NANOPHOTONIC DESIGN AND NANOMATERIAL ASSEMBLY FOR NEXT-GENERATION OPTOELECTRONICS

by

Botong Qiu

A dissertation submitted to The Johns Hopkins University

in conformity with the requirements for the degree of

Doctor of Philosophy

Baltimore, Maryland

May, 2019

Abstract

Nanomaterials are widely deployed in many optoelectronic technologies, with applications in solar energy harvesting, light emission, bio-sensing, computing and communications. The unique advantages of colloidal nanomaterials include size-tunable optical properties and room-temperature solution-processability, which translates to low-cost materials growth and fabrication processes associated with nanomaterials-based technology. Moreover, their lightweight and thin-film nature enables optoelectronic devices made from nanomaterials to be flexibly coated on almost any surface, which is ideal for applications such as wearable electronics and building-integrated photovoltaics. This thesis focuses on combining optical modeling, nanomaterials synthesis, nanofabrication, and advanced optical and electrical characterization techniques to develop nanomaterial-based next-generation optoelectronic devices.

The first section of this thesis focuses on applying nanophotonics design principles to optically engineer solar cell and photodetector device structures for specific applications. One of our studies demonstrated a high-performing visible-blind ultraviolet (UV) thin film photodetector by introducing nanoheterojunctions for enhanced absorption and carrier injection. In

another study, we used optical simulations and an effective medium model to investigate and predict light-trapping enhancements by embedding plasmonic nano-inclusions in the absorbing layer of solution-processed solar cells. We also combined thin-film interference engineering and multi-objective optimization algorithms to control the color and transparency of colloidal quantum dot (CQD) solar cells for applications in building-integrated photovoltaics and multi-junction photovoltaics. In the final study of this section, we proposed and investigated engineering photonic bands in strongly absorbing materials to tune the spectral selectivity of optoelectronic films.

We then focus on developing lead sulfide CQD-based light emitting diodes (QLEDs) and solar cells with novel functionality. We developed a room-temperature-processed silver-nanowire-based transparent electrode for flexible optoelectronics. With carefully-tuned nanomaterials synthesis conditions, we fabricated PbS QLEDs with near-infrared emission that can be easily detected by inexpensive silicon-based photodetectors, paving the way for our proposed flexible transparent light emitting membrane technology, which has many target applications including in next-generation virtual reality googles and motion-capture suits for the film industry. We also built a semi-automated spray-casting system to demonstrate an all-solution-processed CQD solar cell, as a scalable and portable method for manufacturing CQD solar cells, expanding the application areas of this technology.

Thesis Committee

Primary Readers

Susanna M. Thon (Primary Advisor)
Assistant Professor
Department of Electrical and Computer Engineering
Johns Hopkins Whiting School of Engineering

Amy C. Foster
Associate Professor
Department of Electrical and Computer Engineering
Johns Hopkins Whiting School of Engineering

Jacob B. Khurgin
Professor
Department of Electrical and Computer Engineering
Johns Hopkins Whiting School of Engineering

Acknowledgments

Firstly, I would like to give my sincere gratitude to my advisor and supervisor, Dr. Susanna M. Thon. She had her great trust in me and because of that I have this great opportunity to be here. She has been such a great mentor that help me grow fast in all aspects, not only in research but also she has helped me develop all the soft skills. I am also grateful to her that she is very flexible about my schedules, open to any ideas and discussions. I often felt very homesick and those trips back home really help to get me back into the mood. She has also been a great friend to me, to the whole group, supportive and we had great fun at group dinners and all kinds of sports.

I would also like to thank my past and present lab mates, who are all wonderful people, for all their hard work and support throughout this time. I am really grateful to know Ebuka Arinze, who took me into the lab and helped get a quick start. Ebuka and I not only accomplished a number of projects together, we were also close friends and teammates in sports. I would like to thank Nathan Palmquist and Gabrielle Nyirjesy, the earliest members of the lab who not only helped with research but also as undergraduate students helped me learn so much about the life in the college and in the US. I am grateful to Yan Cheng, who came in the same time as me, for how patient she was about

the all the lab responsibility and help in coordinating the work. Finally, I would like to thank Yida Lin for being my roommate as well as labmate. Yida contributed significantly in a number of projects and outside work we had so much great memory together as well. I would like to thank this group of people including Arlene Chiu, Lulin Li, Chengchangfeng Lu, Andrew Rauch, Gary Qian, Garrett Ung, Eric Tsai, Nicole Kim, and Charles Thorton, who made the time an enjoyable journey and I look forward to meeting them often in the future. I would like to acknowledge all the funding sources that gave me the great opportunity to explore the world of science and engineering. Specifically, I would like to thank the National Science Foundation, JHU Discovery Fund, JHU Catalyst Fund and the Cohen Engineering Translational Fund for all the support over the years.

I would like also to thank my greatest basketball friends here at Johns Hopkins. Every place I went I started making new friends on basketball court and JHU is no exception. I can't name all of them all here but I will always remember all of the games we made great efforts together. Some of them have already left Baltimore but I will always miss them and hope to play with them again somewhere in the future. I would like to thank all the JHU CSSA Basketball team members, families and fans. I had my better and worse games but they always had their greatest trust in me, for which I have been really grateful. I would like to give my greatest gratitude among this group to Zengwen Fan, who has been a role model to me on the basketball court since I came here and has been a truly good friend to me in everyday life. I will always remember all the games we played in the 5 years and the happy hours

we had together as a team.

I would like to thank my friends in this department, Hongcheng Sun, Kangmei Li, Tengfei Li, Jaewook Shin, Jasper Stroud, Milad Alemohammad and Kayode Sanni. We supported each other through this journey and we had so much fun playing sports, hiking, BBQ and enjoying the happy hours together. I would like to thank my college friends, Shida Shen, Hao Wu, Wenyang Li, Siqi Wang and Baochen Wu. Even though we can only meet at conference or during short vacation time, but they gave me great support to help me through the hard time and we supported each other. I would like to thank my high school friends, Feifan Zhang and Jindong Chen, who game me great help and comfort when I was feeling low.

I would like to thank my special friend Jiahua Fan, who gave the greatest help when I was at my lowest during this time. Jiahua and I had so much in common that even though we were only roommate for 5 months I feel I have known him for years. He is such a sincere friend to me that we share all our thoughts about life in all aspects and we supported each other through our hard time.

Of course I would like to express my sincerest gratitude to my family, namely my mother (Ximei Xu) and father (Huonan Qiu). They game me the warmest family to grow up and taught me to be a kind person full of love. They give me the most unselfish love in the world and always let me know I always have a safe landing spot even if I fall. I was born in a small town in China and it was them who taught me to have a brave heart to chase my dream by living their own life as an example. I would also like to thank the

rest of my big family, my grandparents, uncles, aunts and cousins for all their love and support for me, which help me keep pursuing my dreams.

Table of Contents

List of Tables

List of Figures

Chapter 1

Introduction and Motivation

Optoelectronics is the bridge between optics and electronics, including the study, design and application of semiconductor-based devices that detect, emit, modulate or transmit light. Optoelectronics technologies include but are not limited to solar cells, light emitting diodes (LEDs), lasers and photodetectors. Every invention of these technologies led to great innovations and made significant impacts on everyday life. Today, optoelectronic technology has reached almost every corner of our daily life, covering power generation [1, 2], security monitoring [3, 4], defense [5, 6], entertainment [7, 8], healthcare [9, 10], etc. The rapidly growing population and urgent demand for innovations for higher quality of life have presented many challenges for existing optoelectronic technology.

One of the greatest challenges in the 21st century is energy sustainability. The global population is projected to reach 9.8 billion in 2050 [11], and the world energy demand is projected to increase 28% between 2015 and 2040 [12]. Regardless of sustainability, rising global temperature with more frequent extreme weather events and air pollution will not allow us to rely on fossil

fuels as energy sources. Many countries have made their own renewable portfolio standard (RPS), and in the USA related goals vary by state. Figure 1.1a shows that in the USA, renewable generation currently has only an 18% share in the total electricity generation and is projected to hit 31% by 2050 [13]. Among all states of the USA, California has the most ambitious goal of reaching 60% generation from renewable sources by 2030 [14]. Figure 1.1b shows that wind and solar photovoltaic (PV) generation has been growing rapidly during the past decades, and these sources are projected to be the mainstream resources to be employed to meet the renewable generation need [13].

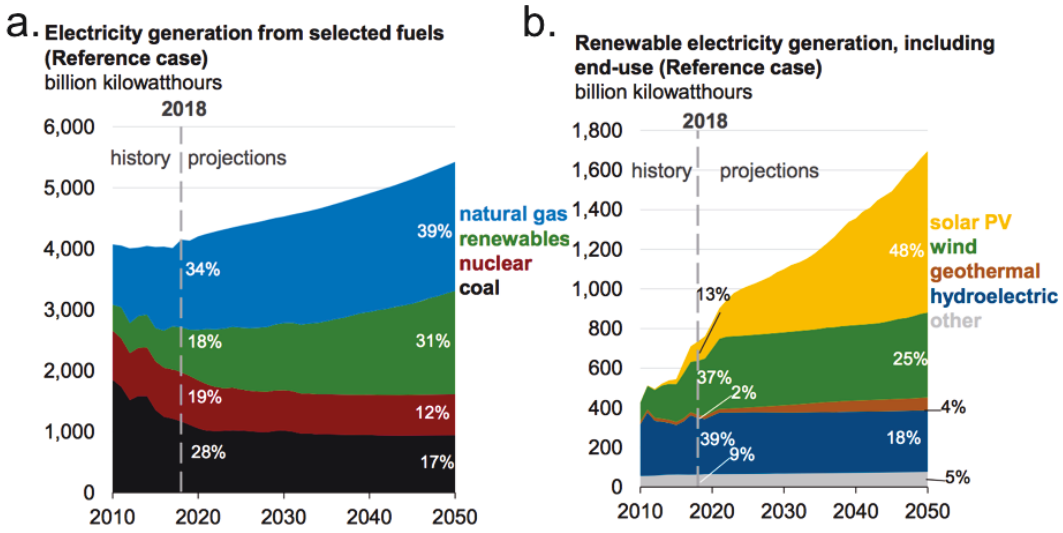

Figure 1.1: USA Electricity Generation Projections : (a) USA Electricity generation from selected fuels with projections to 2050. (b) USA renewable electricity generation, including end use with projections to 2050. [13]

Solar energy has unique advantages in its huge potential and wide accessibility when compared to other renewable sources such as wind and hydropower. Actually, the solar energy hitting the surface of the earth in a one

hour window is enough to fulfill global electricity consumption for the whole year; however, solar PV generation only accounts for less than 3% of current total electricity generation in the USA, and other solar energy harvesting technologies have even less share [13]. That is largely due to the high cost per watt for solar PV generation when compared to other energy resources. However, as shown in Figure 1.2, the cost for solar PV has been decreasing dramatically, and is projected to be lower than that for most fossil fuels by 2020 [15]. Solar PV is the leading technology in solar energy harvesting with the advantage of being both dispatchable and scalable when compared to alternative solar energy harvesting technologies, such as solar thermal generation, that suffer from system complexity and large land use. With its abundance, scalability and rapid cost reduction, solar PV is projected to account for almost half of the renewable electricity generation by 2050 [13].

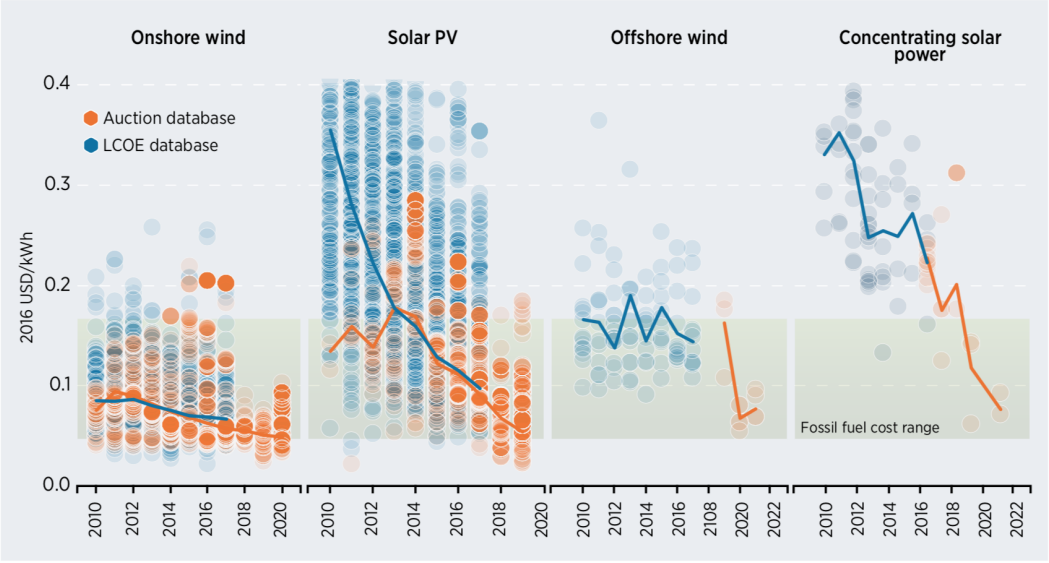

Figure 1.2: Renewable electricity generation cost : The levelized cost of electricity for projects and global weighted average values for concentrating solar power (CSP), solar PV, and onshore and offshore wind, 2010-2022. [15]

Ever since their invention, solar cells have been getting cheaper. As the industry has developed and matured, silicon-based modules came to dominate the market [16], with a few other materials such as cadmium telluride (CdTe) and copper indium gallium diselenide (CIGS) sharing a small portion [17]. These modules have been very successful installed on rooftops and in designated solar farms. However, all of these modules are based crystalline semiconductor materials and suffer from bulkiness, rigidity, expensive manufacturing processes, and poor band gap tunability, limiting the number of areas and infrastructures on which they can be installed. Solar energy lies in a broad spectral range while semiconductor materials can only harvest photons with energies larger than their specific band gap energy, which means a significant portion of the available solar energy is wasted. Ideally, we would want solar cell technology that is flexible, with tunable band gaps, low costs, and the ability to be easily integrated into any scale and on any surface to efficiently harvest solar energy.

Optoelectronics technology itself doesn't make up a single industry; instead, it shares a semiconductor platform and infrastructure over a number of industries, serving as an essential foundational technology that drives innovations in areas such as computing, communications, imaging, information storage, display and sensing. Over the years, the scope of optoelectronics technology also broadened to incorporate other technologies such as photonics [18, 19, 20] and electro-optics [21, 22], making a broader impact.

To meet the growing demands of technology innovation, firstly, performance improvements in optoelectronic technology are of great interest. For

instance, high-brightness with superior color quality is required for display technology to create more vivid views and higher responsivity, together with higher sensitivities, that are critical in detecting weak signals more accurately, helping to develop advanced sensing and automation systems. Secondly, novel functionality such as tailored working spectral ranges, lightweight platforms, and flexibility are of great interest. These novel functionalities could allow huge leaps in industries such as wearable electronics and medical instruments, reducing the complexity as well as weight and size of these systems. Last but not least, cost reduction is needed. Even though many of the cutting-edge optoelectronic technologies have been demonstrated in research labs or have been recently introduced to the market, their high cost and price still hinder their accessibility to consumers. For example, as shown in Figure 1.3, Samsung and Huawei have both recently introduced foldable phones based on flexible AMOLED (active matrix organic LED) screens but the $2,000 starting price [23, 24] , which is 3-4 times of the price of high-end smartphones such as the $749 iPhone XR [25], is surely not affordable for most potential buyers. To address these issues in the research and development of optoelectronic applications, new device architectures and novel materials platforms are urgent needs.

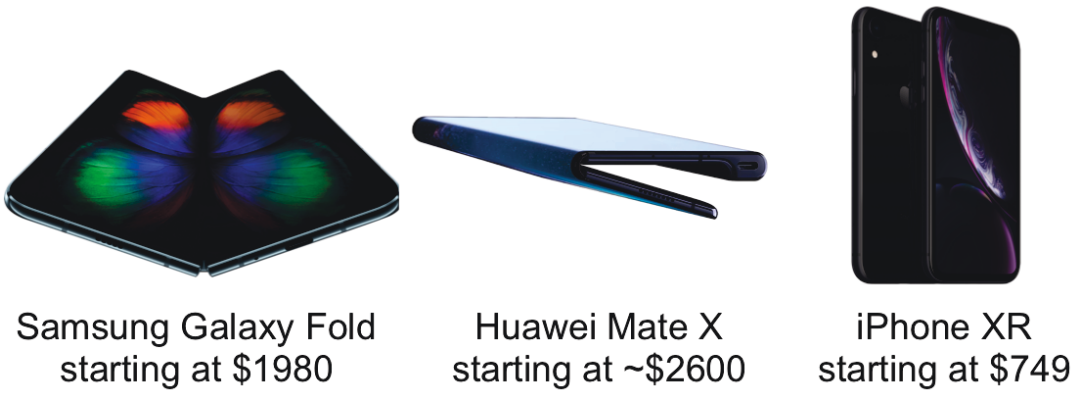

Figure 1.3: High-end commercial electronics with cutting-edge optoelectronics : Left to right: foldable phones from Samsung (left) and Huawei (middle), and a traditional smart phone from Apple (right). [23, 24, 25]

In the past decades, innovations in nanophotonics and nanomaterials have been applied to many areas [26, 27, 28, 29], with optoelectronic applications being a notable success story [8, 30, 31, 32]. The fundamental idea is that once the size of the structure is comparable to or smaller than the wavelength of the light, complex optical phenomena such as interference and scattering will occur, which could be a tuning knob to improve device performance or creating novel functionality. In addition, the properties of nanomaterials can be dramatically different from bulk materials, and nanomaterials can be solution-processed, which allows for the application of various scalable fabrication methods to assemble flexible devices that break the limits of traditional crystalline-semiconductor-based devices. This thesis will focus on using nanophotonic design and nanomaterial fabrication to find solutions for performance improvements, enable novel functionality, allow for manufacturing scalability, and result in cost reductions in the development of future

optoelectronic technologies, allowing us to solve the energy crisis and support innovations in a wide range of industries.

References

[1] Martin A Green, Yoshihiro Hishikawa, Ewan D Dunlop, Dean H Levi, Jochen Hohl-Ebinger, and Anita WY Ho-Baillie. "Solar cell efficiency tables (version 52)". In: *Progress in Photovoltaics: Research and Applications* 26.7 (2018), pp. 427–436.

[2] Martin A Green. "Commercial progress and challenges for photovoltaics". In: *Nat. Energy* 1.1 (2016), p. 15015.

[3] Ulrike Willer, Mohammad Saraji, Alireza Khorsandi, Peter Geiser, and Wolfgang Schade. "Near-and mid-infrared laser monitoring of industrial processes, environment and security applications". In: *Optics and lasers in engineering* 44.7 (2006), pp. 699–710.

[4] Akram M Zeki, Elbara Eldaw Elnour, Adamu A Ibrahim, Chiroma Haruna, and Sameem Abdulkareem. "Automatic interactive security monitoring system". In: *2013 International Conference on Research and Innovation in Information Systems (ICRIIS)*. IEEE. 2013, pp. 215–220.

[5] Philip E Cassady, Ronald N Murata, Sean McKenna, M John Yoder, William E Keicher, Philip M Blumenau, Daniel H Leslie, and Douglas G Youmans. "Laser radar technology for airborne theater missile defense". In: *Applied Laser Radar Technology II*. Vol. 2472. International Society for Optics and Photonics. 1995, pp. 50–62.

[6] Douglas G Youmans and Rodney Robertson. *Modelocked-laser laser radar performance in the detection of TMD and NMD targets*. Tech. rep. SCHAFER (WJ) ASSOCIATES INC CHELMSFORD MA, 1997.

[7] Takuya Komoda, Hisahiro Sasabe, and Junji Kido. "Current Status of OLED Material and Process Technologies for Display and Lighting". In: *2018 25th International Workshop on Active-Matrix Flatpanel Displays and Devices (AM-FPD)*. IEEE. 2018, pp. 1–4.

[8] Takatoshi Tsujimura. *OLED display fundamentals and applications*. John Wiley & Sons, 2017.

[9] Victor S-Y Lin, Kianoush Motesharei, Keiki-Pua S Dancil, Michael J Sailor, and M Reza Ghadiri. "A porous silicon-based optical interferometric biosensor". In: *Science* 278.5339 (1997), pp. 840–843.

[10] Hisataka Kobayashi, Mikako Ogawa, Raphael Alford, Peter L Choyke, and Yasuteru Urano. "New strategies for fluorescent probe design in medical diagnostic imaging". In: *Chemical reviews* 110.5 (2009), pp. 2620–2640.

[11] United Nations, Departement of Economic and Social Affairs, Population Division. *World Population Prospectes: The 2017 Revision, Key Findings and Advance Tables*.

[12] U.S.Energy Information Administration (EIA). *International Energy Outlook 2017*.

[13] U.S.Energy Information Administration (EIA). *Annual Energy Outlook 2019*.

[14] Galen L Barbose. *U.S. Renewables Portfolio Standards: 2018 Annual Status Report*. Lawrence Berkeley National Laboratory.

[15] International Renewable Energy Agency. *Renewable Power Generation Costs in 2017*.

[16] Pierre-Jean Ribeyron. "Crystalline silicon solar cells: Better than ever". In: *Nature Energy* 2.5 (2017), p. 17067.

[17] Taesoo D Lee and Abasifreke U Ebong. "A review of thin film solar cell technologies and challenges". In: *Renewable and Sustainable Energy Reviews* 70 (2017), pp. 1286–1297.

[18] Karl J Ebeling. *Integrated optoelectronics: waveguide optics, photonics, semiconductors*. Springer Science & Business Media, 2012.

[19] Stavros Iezekiel, Maurizio Burla, Jonathan Klamkin, David Marpaung, and Jose Capmany. "RF engineering meets optoelectronics: Progress in integrated microwave photonics". In: *IEEE Microwave Magazine* 16.8 (2015), pp. 28–45.

[20] Francesco Bonaccorso, Z Sun, Ta Hasan, and AC Ferrari. "Graphene photonics and optoelectronics". In: *Nature photonics* 4.9 (2010), p. 611.

[21] Q Wu and X-C Zhang. "Free-space electro-optics sampling of mid-infrared pulses". In: *Applied physics letters* 71.10 (1997), pp. 1285–1286.

[22] Theodor Tamir, Giora Griffel, and Henry L Bertoni. *Guided-wave optoelectronics: device characterization, analysis, and design*. Springer Science & Business Media, 2013.

[23] Samsung. *Samsung Galaxy Fold*.

[24] Huawei. *Huawei Mate X*.

[25] Apple. *Apple XR*.

[26] A Femius Koenderink, Andrea Alu, and Albert Polman. "Nanophotonics: shrinking light-based technology". In: *Science* 348.6234 (2015), pp. 516–521.

[27] Chaoliang Tan, Xiehong Cao, Xue-Jun Wu, Qiyuan He, Jian Yang, Xiao Zhang, Junze Chen, Wei Zhao, Shikui Han, Gwang-Hyeon Nam, et al. "Recent advances in ultrathin two-dimensional nanomaterials". In: *Chemical reviews* 117.9 (2017), pp. 6225–6331.

[28] Wei Xia, Asif Mahmood, Zibin Liang, Ruqiang Zou, and Shaojun Guo. "Earth-Abundant Nanomaterials for Oxygen Reduction". In: *Angewandte Chemie International Edition* 55.8 (2016), pp. 2650–2676.

[29] Peter G Bruce, Bruno Scrosati, and Jean-Marie Tarascon. "Nanomaterials for rechargeable lithium batteries". In: *Angewandte Chemie International Edition* 47.16 (2008), pp. 2930–2946.

[30] Edward H Sargent. "Infrared photovoltaics made by solution processing". In: *Nature Photonics* 3.6 (2009), p. 325.

[31] Kevin A Bush, Axel F Palmstrom, J Yu Zhengshan, Mathieu Boccard, Rongrong Cheacharoen, Jonathan P Mailoa, David P McMeekin, Robert LZ Hoye, Colin D Bailie, Tomas Leijtens, et al. "23.6%-efficient monolithic perovskite/silicon tandem solar cells with improved stability". In: *Nature Energy* 2.4 (2017), p. 17009.

[32] Susumu Noda, Masayuki Fujita, and Takashi Asano. "Spontaneous-emission control by photonic crystals and nanocavities". In: *Nature photonics* 1.8 (2007), p. 449.

Chapter 2

Colloidal Nanomaterials and Device Theory

Colloidal nanomaterials are synthesized and stabilized in the solution phase, which means solution-processed manufacturing methods such as spin coating [1, 2], ink-jet printing [3, 4] and spray coating [5, 6] can be used to assemble to assemble various optoelectronic devices such as LEDs [7, 8], photodetectors [5, 9] and solar cells [1, 10] from these materials. Therefore, the cost of intensive processing associated with traditional materials could be reduced if we can assemble devices using colloidal nanomaterials. What is more, due to the fundamental physics of materials, structuring materials on the nanoscale can enable properties that are dramatically different from those of the bulk forms, making colloidal nanomaterials attractive building blocks for constructing optoelectronic devices with improved performance [7, 11] and novel functionality [2, 8]. In parallel, more development on scalable fabrication methods is also of great interest to further cut processing costs for colloidal nanomaterials. The fundamental physics and unique optical properties of the most important colloidal nanomaterials, along with the theory of the operational principles of

the optoelectronic devices that are developed within the scope of this thesis will be discussed below.

2.1 Colloidal Quantum Dots

Colloidal quantum dots are a type of quantum-confined semiconductor nanocrystal stabilized in solution. When the size of the particles are comparable to or smaller than the Bohr exciton radius of the constituent bulk material (usually 2-50 nm), the quantum confinement effect becomes apparent [12]. Similar to the particle-in-a-box model, the energy levels of the QDs become discrete and the effective band gap is larger than its bulk form.

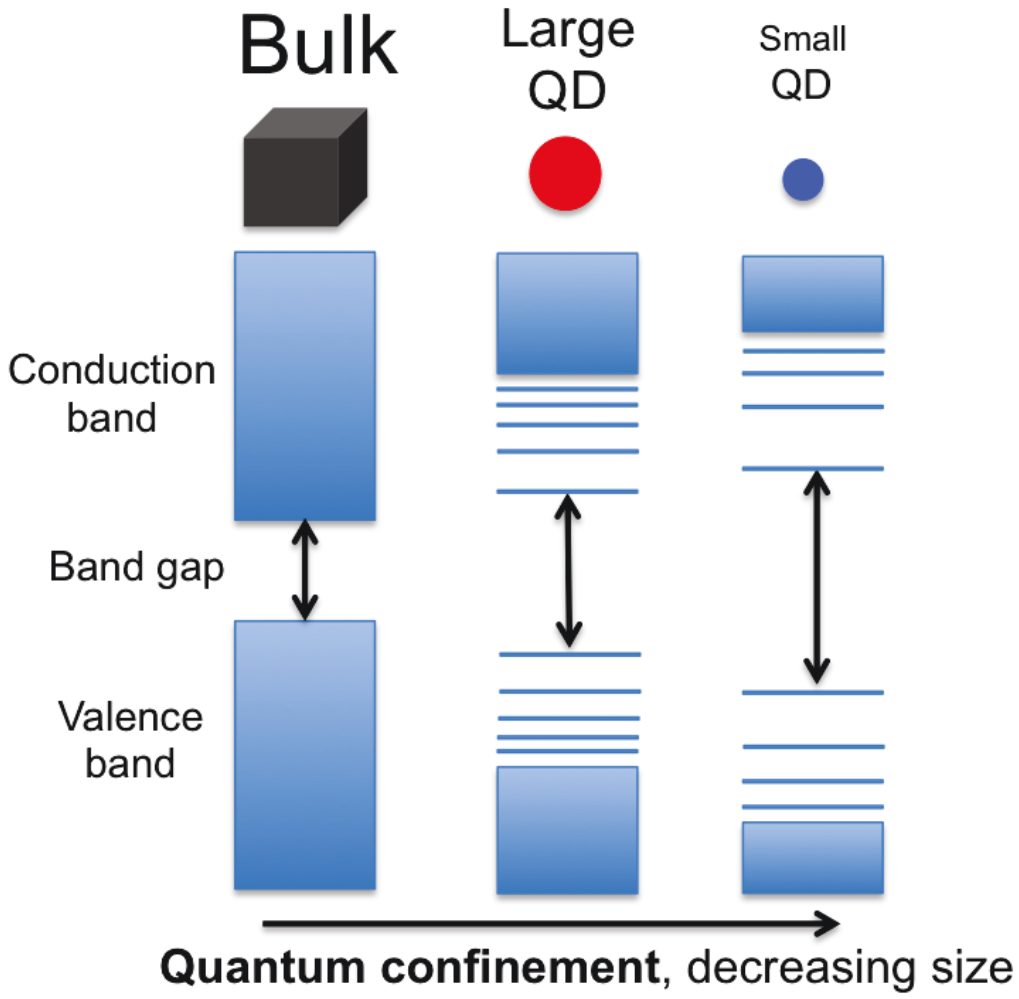

Figure 2.1: Quantum confinement effect illustration : Left to right: energy level diagrams of a bulk semiconductor, a relatively large QD and a relatively small QD. Due to the quantum confinement effect, the band gap of a QD is larger than its bulk form, and the band gap and energy level separations increase with decreasing QD size.

The quantum confinement effect is illustrated schematically in Figure 2.1: the smaller the quantum dot is, the larger the band gap will be. The quantitative description of band gap energy is given by the Brus Equation [13]

equation 3.2:

$$E^* = E_g + \frac{h^2\pi^2}{2R^2}[\frac{1}{m_e} + \frac{1}{m_h}] - \frac{1.8e^2}{\epsilon_o\epsilon_p R} \tag{2.1}$$

In the Brus Equation, E^* is the apparent band gap, E_g is the band gap of its bulk form, m_e and m_h are the effective electron and hole masses respectively, ϵ_p is the dielectric constant of the quantum dot material, and R is the radius of the quantum dot [13]. The second term in this equation comes from the quantum confinement of wavefunctions of electrons and holes while the last term is due to the electron-hole Coulomb interaction. Due to a large surface-to-volume ratio, surface modifications are necessary to mitigate the dangling bonds to bonds on the surface of quantum dots to reduce the trap states densities which contribute to losses in optoelectronic devices [14]. As synthesized, colloidal quantum dots are usually decorated with long-chain organic ligands such as oleic acid to prevent agglomeration and control the growth kinetics.

2.1.1 PbS CQDs Synthesis

Lead sulfide, PbS, has a direct bulk band gap of 0.41 eV [15] and a Bohr exciton radius of 18 nm [16, 17], making it an ideal candidate for CQDs with band gap energies tunable through the near-infrared range [15, 18, 19, 20]. A widely used method and the route we use to synthesize group IV-VI semiconductor nanoparticles, such as PbS and PbSe, CQDs, is the so-called "hot-injection" method [21]. Commonly used precursors used for PbS CQDs synthesis are PbO, oleic acid and bis(trimethylsilyl)sulfide ($(TMS)_2S$) [21]. The oleic acid serves as a surface passivant and enables nanoparticle colloidal

stability through steric effects. The PbO and oleic acid are dissolved in a solvent (octadecene, ODE) at room temperature, and then degassed and heated up to the desired injection temperature. The S precursor at room temperature is injected into the hot Pb precursor solution to initiate the nanoparticle nucleation reaction.

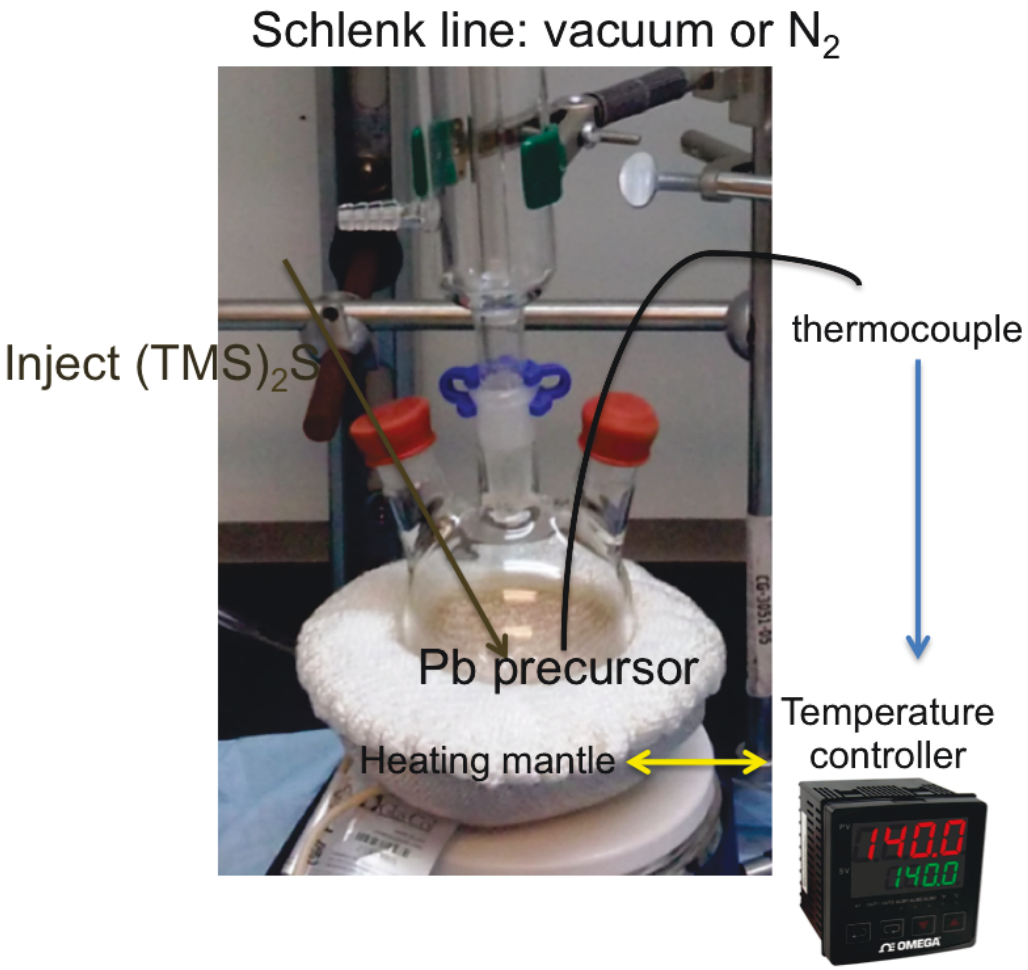

Figure 2.2: Apparatus for PbS CQD synthesis in our lab : the setup consists of a Schlenk line, a three-neck flask, a hotplate and a temperature control system including a heating mantle, a thermocouple and a smart temperature controller.

The synthesis apparatus in our lab is shown in Figure 2.2, where the

Schlenk line is used to provide a vacuum for degassing the precursors or N_2 for inert processing steps. A thermocouple, temperature controller and heating mantle are used to precisely measure and control the temperature of the synthesis mixture. Detailed synthesis procedures for specific particle types are described in the Appendix.

2.1.2 Optical Properties and Band Gap Tuning

The optical properties of CQDs differ as a function of composition, ligand character, particle shape and particle size. Two of the most important optical properties of CQDs are the absorption onset, or first exciton wavelength, and the emission wavelength, which are also referred to as the band gap. Figure 2.3 shows the absorption spectra for different sizes of PbS CQDs synthesized in our lab. They are labeled by the longest absorption peak wavelength (750 nm _ 1600 nm), which is also known as the first exciton (1S) peak wavelength and optical band gap wavelength. The absorbance of PbS CQDs can extend through the near-infrared range, having huge potential in efficient solar energy harvesting, optical communications and imaging.

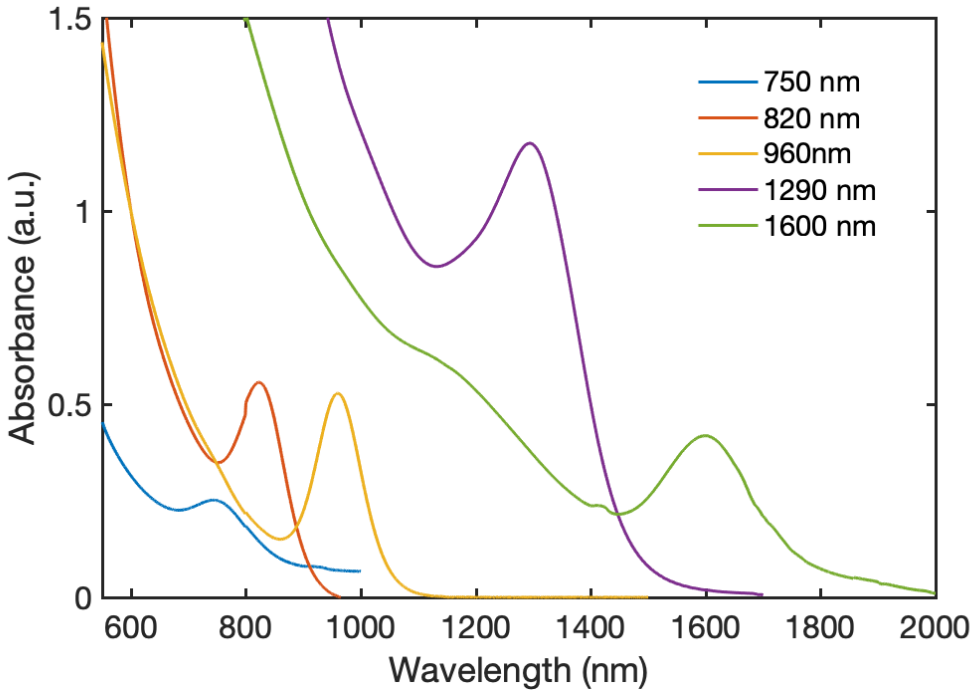

Figure 2.3: Absorbance spectra of different sizes of PbS CQDs : absorbance spectra measured using Cary5000 UV-VIS-NIR spectrophotometerfor for PbS CQDs of approximately 2.4 nm to 6.2 nm in diameter (estimated using equation 3.3), labeled by their first exciton peak wavelengths.

As discussed earlier, the band gap of a CQD is larger than that of its bulk form and increases with nanoparticle decreasing size due to quantum confinement, which can be described using the Brus equation [13]. The simplified model of the size-dependent effective band gap of PbS CQDs has been empirically determined to follow [18]:

$$E^*(eV) = 0.41 + \frac{1}{0.0252d^2(nm) + 0.0283d(nm)} \tag{2.2}$$

where the E^* is the apparent band gap in eV and d is the diameter of the CQD in nm. Therefore, accurately controlling the size of the CQDs and

having monodisperse CQDs is critical to optimizing the optical properties of CQD materials. In the hot-injection method, CQD size is controlled by several factors such as precursor concentration, injection temperature and the dynamics of the cooling process. Generally, higher relative oleic acid concentration, higher injection temperatures and slower cooling will yield larger CQDs with smaller band gap. Systematic studies revealing an empirical relationship between the first exciton peak wavelength and the oleic acid concentration and injection temperature during synthesis have resulted in the following equation [19]:

$$\lambda_{1s} = 935nm + m(T_{inj})g_{OA} \tag{2.3}$$

Where λ_{1s} is the wavelength of first exciton peak, $m(T_{inj}) = 5.9 + 0.0026{T_{inj}}^2$ is the temperature-dependent slope and g_{OA} is the mass of the oleic acid used in the specific protocol, from which the relative oleic acid concentration can be easily calculated as well [19]. As shown in Figure 2.3, in our lab we are able to control the PbS QD size and achieve an average E^* spread of 0.18 eV, measured by the full-width at half maximum (FWHM) of the first exciton peak in the absorbance spectra and peak in photoluminescence spectra, which includes both homogeneous and inhomogeneous broadening.

Ligands on the quantum dot surface also play a role in the optical properties, which, as discussed earlier, include the effective band gap and spectral absorptivity. In the solution phase, the CQDs are capped with long oleic acid ligands, and are therefore widely spaced to the point where the inter-particle coupling is negligible. When the oleic acid ligands are replaced with small

molecules such as 3-Mercaptopropionic acid (MPA), 1,2-Ethanedithiol (EDT) or PbI_2 to assemble quantum dot solids, stronger inter-dot coupling induces a red-shift in the absorption onset because of wavefunction overlap between the excitons associated with neighboring particles. Composition is also important, an example of which is that chemical doping or surface oxidation will impact the optical properties of CQDs. For instance, when stored in air, the un-passiviated <100> surfaces of relatively large (>4 nm in diameter) PbS CQDs tend to oxide easily, and the first exciton wavelength will blue-shift to longer wavelengths because of a decrease in the effective CQD diameter [22].

The emissive properties of colloidal quantum dots, specifically photoluminescence and electroluminescence, play critical roles in many optoelectronic technologies as well, and they are significantly influenced by the surface passivation. Better surface passivation helps eliminate trap-assisted recombination, increasing radiative recombination efficiency and therefore luminescence efficiency. In addition to causing a red-shift in the absorption and emission spectra, the coupling between quantum dots induced by the ligands also impacts the luminescence properties by increasing exciton dissociation rates, which lowers radiative recombination rates. There have been studies showing that photoluminescence quantum yields increase by a factor of 2 when glutathione (GSH) ligands are used rather than tiopronin (TP) ligands due to the presence of an inner thiol group in GSH [23].

Ligands also play important roles in CQD solids in determining charge injection and transport properties, which can affect the quantum dot luminescence properties as well. There has been work showing the importance

of the ligand size in optimizing the inter-CQD spacing for high efficiency PbS quantum dot infrared LEDs [24]. Generally, there exists a red-shift of the luminescence peak wavelength with respect to the first exciton absorption peak, and this shift is known as the Stokes shift. The Stokes shift of CQDs is relatively large, and it increases with decreasing particle size. The origins of the Stokes shift of CQDs are still under discussion but are commonly attributed to surface properties [25]. Candidates for PbS CQD surface ligands usually have a thiol group, a carboxylate group, an amine group, or some combination. Additionally, single halide atoms (Cl, Br, or I) have also become popular ligand choices, especially in CQD solar cell films. Ligands selection and size-tuning during the synthesis phase are the major part determinants of the optical and electronic properties of CQDs for optoelectronic technology.

2.2 Plasmonic Nanoparticles

Surface plasmons refer to the collective oscillations of the free electrons bounded at the interface of a conductor and a dielectric. Surface plasmons can couple strongly to incident electromagnetic fields with proper design. Surface plasmonic structures confine the propagation of waves or localize the fields, which can lead to greatly enhanced local field strengths. Due to confinement that can exceed the free-space diffraction limit, high local field intensity, and high sensitivity to local optical properties, surface plasmons have been used effectively in a broad range of applications such as optical communications [26], computing [27] and sensing [28].

2.2.1 Localized surface plasmon resonances

When the size of a plasmonic nanoparticle is comparable to or smaller than the the relevant light wavelength scales, surface plasmons can be excited and confined within the particle. These excitations are termed localized surface plasmons (LSPs) with their associated absorption or scattering peaks in wavelength or frequency termed localized surface plasmon resonances (LSPRs). Figure 2.4 illustrates the dipole mode and quadrupole mode of a LSP in a spherical plasmonic nanoparticle.

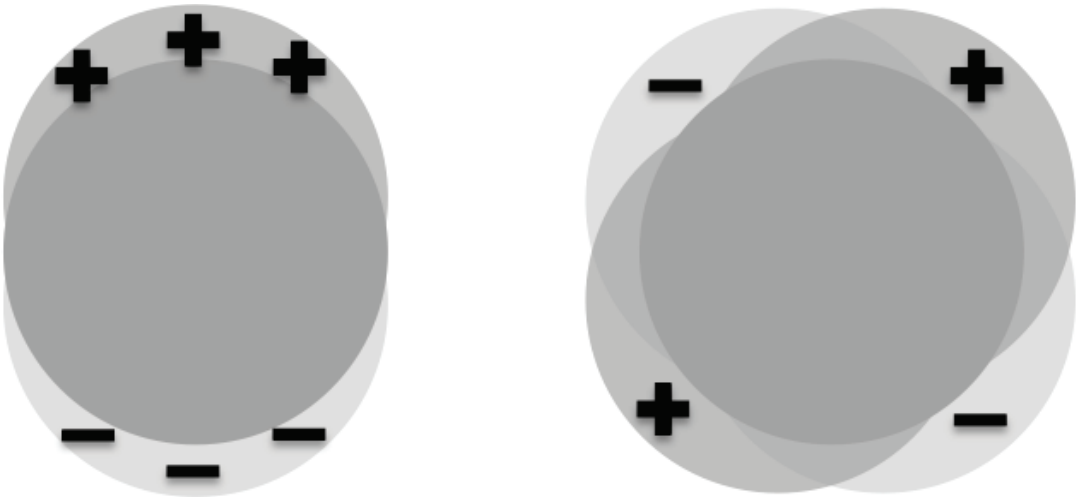

Figure 2.4: Schematic showing LSPR mode charge distributions in a spherical plasmonic nanoparticle : left is the dipole mode and right is the quadrupole mode. The opaque areas represents the nanoparticle while the semitransparent areas represent the collective oscillations of electrons.

There are two key properties of LSPRs that are useful in optoelectronic devices. First, the electric field intensity is greatly enhanced in the vicinity of the nanoparticle and falls off evanescently with increasing distance from the surface. Second, the resonant frequencies or wavelengths are highly sensitive to the local and surrounding refractive index. These features form the basis of

using LSPRs for sensing applications [28]; however, the optical properties of plasmonic nanoparticles can be very useful in absorption enhancement [29, 30] in optoelectronic applications as well.

2.2.2 Optical properties of plasmonic nanoparticles

In the quasi-static approximation, when light is scattered by small sphere particles, the dipole moment can be expressed as:

$$P = 4\pi\epsilon_m r^3 \frac{\epsilon_p - \epsilon_m}{\epsilon_p + 2\epsilon} E_0 \tag{2.4}$$

The scattering cross-section and absorption cross-sections can be obtained from the scattering field radiated by this dipole, which is induced by plane wave [31, 32]:

$$\sigma_{sca} = \sigma_{geom} \frac{8}{3} q^4 \left| \frac{\epsilon_d - 1}{\epsilon_d + 2} \right|^2 \tag{2.5}$$

$$\sigma_{abs} = \sigma_{geom} 4q \, \mathrm{Im}[\frac{\epsilon_d - 1}{\epsilon_d + 2}] \tag{2.6}$$

Where $\sigma_{geom} = \pi a^2$ is the geometrical cross-section, $q = kr$ is the dimensionless size and $\epsilon_d = \epsilon_p / \epsilon_m$ is the relative dielectric function. We note from these formula that resonance of will occur when $\mathrm{Re}(\epsilon_d) = -2\epsilon_m$ and this is known as the Fröhlich condition. This resonance is due to the resonant excitation of the dipole surface plasmon and with the Drude model of dielectric function this resonance frequency is $\omega_{sp} = \omega_p / \sqrt{3}$, if the frequency of electron collisions is small [31, 32].

However, retardation effects in larger particles result in breakdown of the quasi-static approximation. In order to capture size effects on the spectra, including changes of the position of width of plasmon peak, Mie Theory [33] can be employed. When illuminated with an incident plane wave, the total scattering, extinction and absorption cross-sections of a homogeneous conducting spherical particle can be described, according to Mie Theory, as [32]:

$$\sigma_{sca} = \frac{2\pi}{k^2} \sum_{L=1}^{\infty} (2L+1)(|a_L|^2 + |b_L|^2) \tag{2.7}$$

$$\sigma_{ext} = \frac{2\pi}{k^2} \sum_{L=1}^{\infty} (2L+1) Re(a_L^2 + b_L) \tag{2.8}$$

$$\sigma_{abs} = \sigma_{ext} - \sigma_{sca} \tag{2.9}$$

where k is the wave vector of light and L is the integer number that represents the order of the scattering modes. a_L and b_L are parameters that derived from the Riccati-Bessel functions ψ_L and χ_L :

$$a_L = \frac{m\psi_L(mx)\psi'_L - \psi'_L(mx)\psi_L(x)}{m\psi_L(mx)\chi'_L - \psi'_L(mx)\chi_L(x)} \tag{2.10}$$

$$b_L = \frac{\psi_L(mx)\psi'_L - m\psi'_L(mx)\psi_L(x)}{\psi_L(mx)\chi'_L - m\psi'_L(mx)\chi_L(x)} \tag{2.11}$$

Here, $m = \tilde{n}/n_m$, where $\tilde{n} = n_R + in_I$ is the complex refractive index of the nanoparticle and n_m is the real refractive index of the background. For

$x = k_m r$, r is the radius of the particle and $k_m = 2\pi/\lambda_m$ is the wavevector in the background material rather than vacuum.

According to Mie Theory, the optical properties strongly depend on the material and size of the particles. Noble metals such as gold and silver are the most common materials used for plasmonic nanoparticles in the visible and near-infrared spectral range, and their resonances can be easily tuned by controlling their sizes. The shape of the nanoparticles is important as well in determining the resonances [34]; an example of which is the existence of two strong extinction peaks due to transverse and longitudinal modes in gold nanorods [35]. Therefore, the material selection, size and shape tuning are critical in designing plasmonic nanoparticles to facilitate the development of new optoelectronic technology.

2.3 Nanomaterials-Based Optoelectronic Devices

2.3.1 Solar cells

Solar cells are semiconductor-based devices that convert solar radiation into electricity via the photovoltaic effect. The basic structure and operation of a solar cell is illustrated in Figure 2.5a.

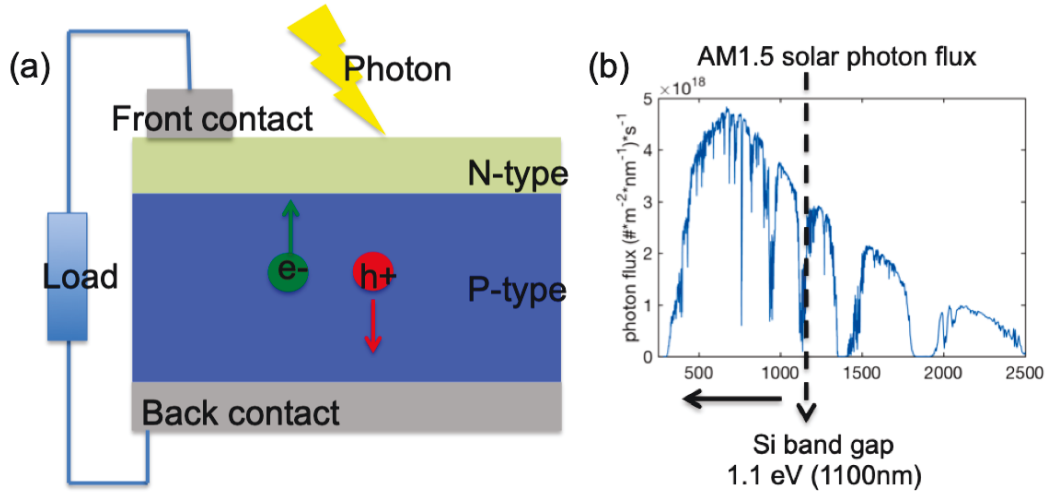

Figure 2.5: Solar Cell schematic and AM1.5 solar spectrum :(a) Schematic showing the basic structure and operational principles of a solar cell. It consists of a front contact, an n-type and a p-type semiconductor forming a P-N junction, and a back contact. Photons are absorbed in the n- and/or p-layers, resulted in the exciton of electron-hole pairs which dissociate and are driven through the device by the junction to be collected as current through their respective electrodes. (b) AM1.5 solar photon flux t with the band gap and absorbing range of silicon labeled. Si will absorb photons with wavelengths smaller than its band gap wavelength (1100 nm).

A solar cell typically consists of a p-n semiconductor junction and two conductive layers that make up the front and back contacts. When photons with energy greater than the band gap energy enter the device, they will be absorbed by the absorbing layer (the p- or n-type semiconductor in the case of Figure 2.5a) and generate electron-hole pairs. If the carriers reach the junction before they recombine, they are separated by the electric field at the junction and travel through the device to be collected by the contacts as current.

Under short circuit conditions (zero voltage applied), there is no build up of charge as light generated carriers exit the device and form the short circuit current. Under illumination, the separation and build up of charge creates an electric field at the junction which is in opposition to the that already

existing at the junction, thereby reducing the net electric field and giving rise to diffusion current. When a new equilibrium is reached between the diffusion current and drift current, a voltage is established by the separation between the quasi-Fermi levels for electrons and holes, known as the photovoltaic effect and an open circuit voltage could be measured from the solar cell. With forward voltage output and current output generated from the solar cell, the device delivers power to the load.

Solar radiation is essentially black-body radiation at a temperature of $\approx 5800K$, whose spectrum is very broadband with a peak in the visible and can be described in detail using Planck's Law [36, 37]. Solar radiation can be absorbed by atmosphere and the path length of sunlight reaching the earth surface varies across time and location. Air mass (AM): $AM = 1/cos(\theta)$ is used define the actual path length light travels through the atmosphere normalized to the shortest possible path length, where θ is the angle from the vertical (zenith angle). Air Mass 1.5 (AM1.5) solar spectrum is widely used as reference for evaluating performance of solar cell and its photon flux plot is plotted in Figure 2.5b.

Due to the current-voltage trade off that exists for solar cells made from a single semiconducting material and other assumptions that go into the detailed balance theory calculations for solar cell efficiency, the optimal band gap range for a single junction solar cell is approximately 1.1-1.4 eV, and the theoretical efficiency limit is 31%-33%, which is called the Shockley-Queisser limit [38]. The theory is based on thermodynamics and semiconductor physics, which will use parameters such as temperature of the sun's surface (T_S),

the ambient temperature, and the electronic band gap of the semiconductor material. The model generating these results is based on a few assumptions namely:

1. Photons with energies smaller than the band gap of the semiconductor will not be absorbed — spectral loss.
2. Complete absorption of photons with energy greater than the band gap of the semiconductor while each absorbed photon only generate one electron-hole pair, whose excessive energy is converted to heat — thermalization loss.
3. Radiative recombination is the only recombination process accounted for.
4. Infinite mobility: carriers can be collected no matter where they are generated.
5. Resistive losses are zero.
6. The solar cell temperature is kept at ambient temperature (300K).
7. "One sun" illumination: the incident sunlight is not concentrated.

The band gap of silicon lies within this range as shown in Figure 2.5b, and the low manufacturing costs due to decades of infrastructure investment makes silicon the dominant solar cell material on the market today.

The most important figure of merit of a solar cell is the power conversion efficiency (PCE); however, there are many other parameters of interest for

solar cell operation as well. The current density - voltage ($J-V$) curve of a solar cell measured under illumination is used to measure these important figures of merit. A typical J-V curve of a solar cell with the relevant parameters labeled is drawn in Figure 2.6.

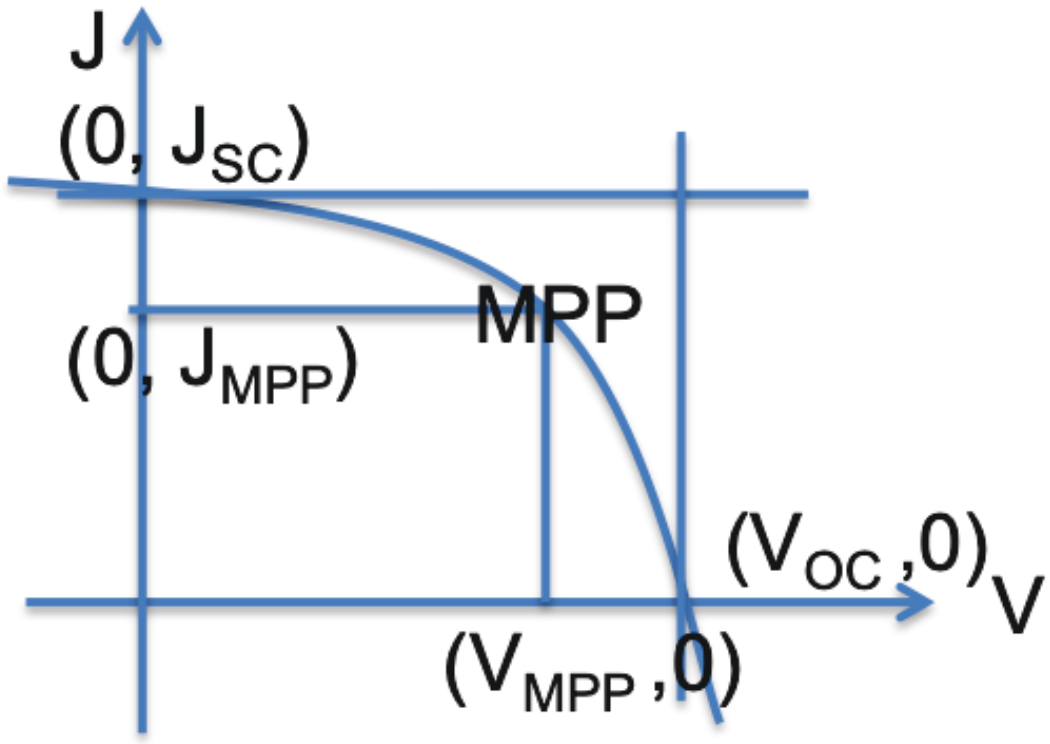

Figure 2.6: Schematic of a typical $J-V$ characteristics of a solar cell : the short circuit current density (J_{SC}), open circuit voltage (V_{OC}), and maximum power point (MPP) with its corresponding current density (J_{MPP}) and voltage (V_{MPP}) are labeled.

The short circuit (SC) current density, J_{SC}, is the current density at zero bias and largely determined by absorption and carrier collection efficiency. The open circuit (OC) voltage, V_{OC} , is the voltage at zero current, which is largely determined by the band gap or absorption onset of the material and the separation between the quasi-Fermi levels for electrons and holes. The

open circuit voltage is therefore related to the doping density on both sides of any charge-separating junctions and is generally limited by recombination processes. The maximum of the product of current density and voltage is termed the maximum power point (MPP), with a current density J_{MPP} and voltage is V_{MPP}. Fill factor (FF) is defined as a measure of the "squareness" of the J-V curve, reflecting the effect of series and shunt resistance existing in the device. It is given by the ratio of the current density and voltage at the maximum power point to the product of the open circuit voltage and short circuit current density:

$$FF = \frac{J_{MPP}V_{MPP}}{J_{SC}V_{OC}}$$

Finally, the power conversion efficiency is calculated by dividing the maximum power density by the input AM1.5 solar power density ($\approx 100 mW/cm^2$) we will get the PCE:

$$PCE = \frac{J_{MPP}V_{MPP}}{P_{AM1.5}} \approx \frac{J_{MPP}V_{MPP}}{100 mW/cm^2} = \frac{J_{SC}V_{OC}FF}{100 mW/cm^2}$$

Nanomaterials-based solar cells such as organic, perovskite and CQD solar cells are of significant interest due to their low cost and flexibility potential. In addition to the solution-processibility, CQD solar cells also have unique advantages in band gap tunability for building multi-junction solar cells and high efficiency potential due to enhanced multiple exciton generation rates over bulk materials. The solar cell spectrum has almost half its photons in the infrared region that is not absorbed by traditional single junction solar cell

materials. By absorbing different portions of the solar spectrum in different materials one can push the efficiency limit up to 41% in two-junction solar cells and even higher in multi-junction solar cells [39]. PbS CQD solar cells can harvest infrared photons very efficiently and have gone through rapid development during the past decade [40]. The highly efficient PbS solar cells today all employ a planar heterojunction structure with record PCEs exceeding 12% [41]. A typical planar heterojunction PbS CQD solar cell structure is shown in Figure 2.7.

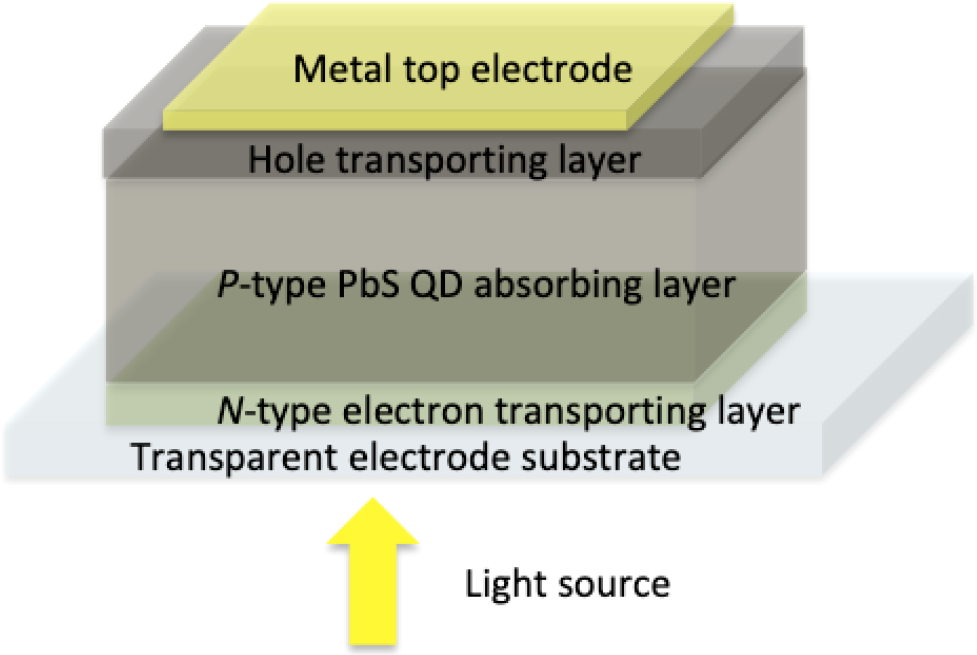

Figure 2.7: Schematic of a planar heterojunction PbS CQD solar cell

This is a multilayer structure that consists of a front transparent electrode, n-type electron transport layer, p-type PbS QD absorbing layer, a hole transport layer and a metal top electrode. All of the layers have thicknesses on the order of hundreds of nanometers, making the devices ultra-lightweight and

possibly flexible, depending on the substrate.

2.3.2 Photodetectors

Photodetectors are devices that detect photons, usually by converting light to electrical signals. There are various types of photodetectors that are classified based on their physical structures or modes of operation, including photoelectric [42], photothermal [43], photochemical [44], photoconductor [45, 46], phototransistor [47, 48] and photodiode [49, 50] type detectors.

Among these types of photodetectors, solid-state semiconductor-based photodetectors are widely used and of great interest due to their mature material processing, device integration and packaging technology and ease of use. The three main classes of solid-state photodetectors are photoconductors, phototransistors and photodiodes. Their respective device structures are illustrated schematically in Figure 2.8.

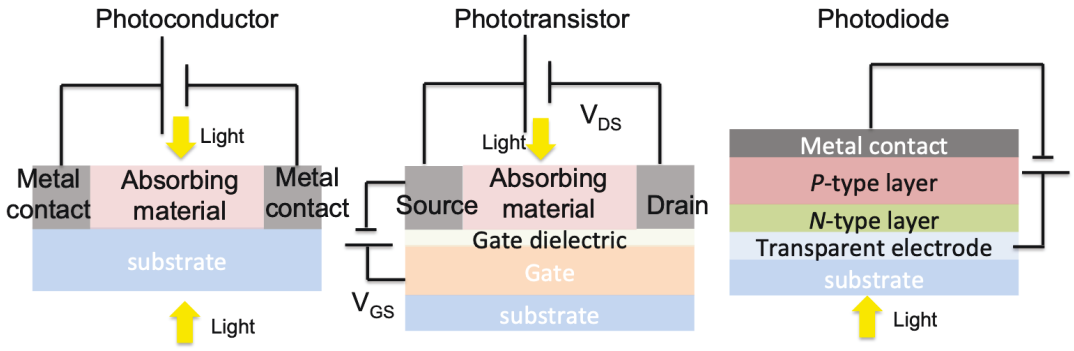

Figure 2.8: Schematic of solid-state photodetector structures:left to right: a representative of photoconductor, phototransistor and photodiode.

In photoconductive photodetectors, absorption of photons generates electron-hole pairs in the absorbing semiconductor and increases its conductivity. Carriers are circulated through the external circuits before recombining with the opposite charge carriers; therefore the differing lifetimes of the two carrier types allows for photoconductive gain, resulting in a larger number of circulating carriers than the number of absorbed photons. In phototransistor-type photodetectors, in addition to the electron-hole pairs generated in the semiconducting channel by photon absorption, the gate and drain voltages also provide a way to tune carrier distribution and collection in the channel, modulating the electrical signal. Photodiode-type photodetectors rely on the built-in potential provided by a p-n junction or a Schottky junction to direct photogenerated carriers; therefore the quantum efficiency in these devices cannot exceed unity.

Important figures of merit for photodetectors include quantum efficiency (QE), responsivity (R), noise equivalent power (NEP) and specific detectivity (D^*). QE is defined as the ratio between the number of electrons produced as current and the number of incident photons:

$$QE = \frac{n_e}{n_{ph}}$$

where n_e is the electron flow rate in the current and n_{ph} is the incident photon rate. The responsivity is given by:

$$R = QE\frac{e}{h\nu} = \frac{I}{P}$$

where QE is the quantum efficiency, e is the electron charge, h is Plank's constant, ν is the photon frequency, I is the measured current and P is the incident power. The noise equivalent power is given by:

$$NEP = QE\frac{I_n}{R}$$

where I_n is the noise current and R is the responsivity. The specific detectivity is given by:

$$D^* = \frac{\sqrt{A_d B}}{NEP} = \frac{\sqrt{A_d B}R}{I_n}$$

where A_d is the aperture of the detector, B is the electrical bandwidth in frequency, R is the responsivity, I_n is the noise current and NEP is the noise equivalent power.

Nanomaterials and nanostructures have been successfully incorporated into the design of photodetectors. Traditional crystalline semiconductor-based photodetectors have limited bandwidth, spectral selectivity, strict lattice-matching requirements for the materials, and cooling requirements while in operation. Nanomaterial-based absorbers such as organic polymers, perovskites and CQDs have the potential to solve some of these problems by offering spectral tunability and relatively low cost and facile processing methods and have therefore made significant progress in photon detection technologies [9, 51, 52]. Nanostructures and nanophotonics designs have additional advantages for photodetectors such large surface-to-volume ratios [53], light trapping [54], ease of miniaturization and integration with readout integrated

circuitry (ROIC) [55] as well as new photon detection mechanisms [56, 57].

2.3.3 Light-emitting diodes

Light-emitting diodes (LEDs) are devices that emit light in response to an input current, a process termed "electroluminescence (EL)". Photons are the product of radiative recombination of injected carriers within the active semiconductor layer of the LED. A band diagram schematic of a typical LED device illustrating its operating mechanism is shown in Figure 2.9. The electrons and holes are injected from different layers and trapped within the emission (active) layers by energy barriers formed between the transport/blocking layers and the emission layer, resulting in the emission of photons through radiative recombination.

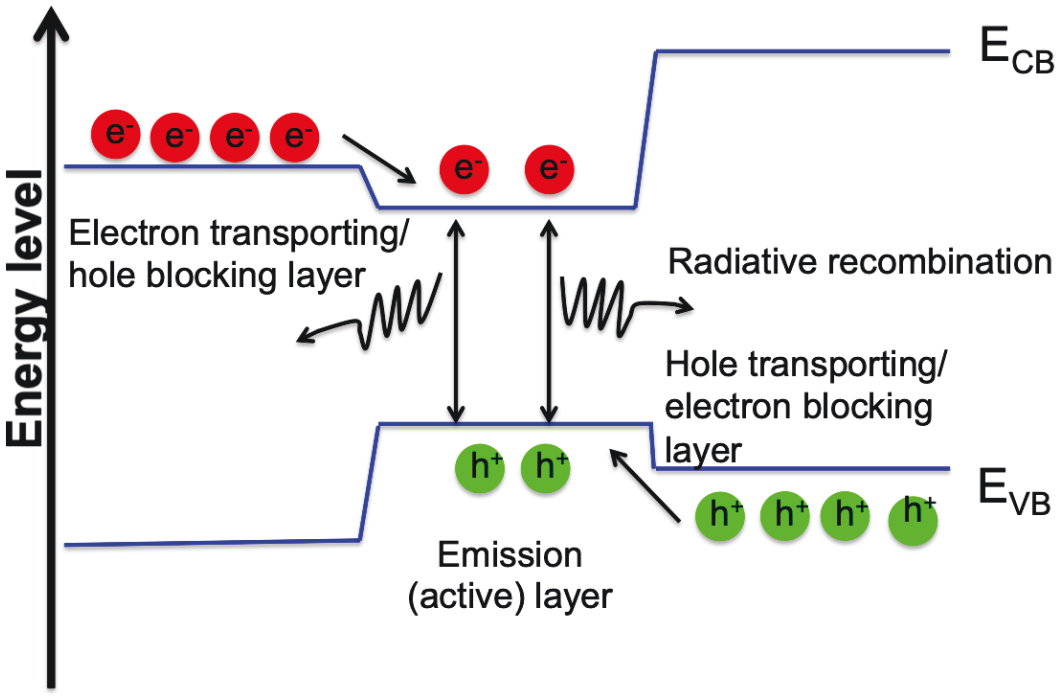

Figure 2.9: Band diagram schematic of within a LED device:the band diagram schematic of the semiconductor layers within a LED device device illustrating the operating mechanism.

As shown in Figure 2.9, the emission wavelength is determined by the band gap of the active layer semiconductor. The emission wavelength of the LED is the most critical property for targeting specific applications. The visible energy emission range is of great interest for display technology, and the inventor of the blue LED was awarded the Nobel Prize in Physics [58]. Nanomaterials including organic polymers, perovskites and CQDs can have high brightness [59, 60, 61] and narrow bandwidth of emission for superior color quality [11, 62, 63]. Organic LEDs (OLEDs) already dominate the high-end commercial electronics display market [11]. Nanomaterials-based LEDs also have their unique advantages including tunable emission wavelengths [62], ease of

fabrication, low costs, and flexible device structures, and significant progress has been made in engineering their performance [8].

In addition to the emission bandwidth (usually characterized by the full width at half maximum (FHWM) of the EL peak), another critical LED figure of merit is the EL external quantum efficiency (EQE), in the nanomaterials-based LEDs which is given by:

$$\eta_{EL} = \gamma \eta_{PL} \chi \sigma_{out}$$

where the γ is the ratio of excitons to injected carriers in the active layer, η_{PL} is the photoluminescence quantum efficiency, also known as PL quantum yield (PLQY), χ is the spin multiplicity of the radiatively recombining excitons, and σ_{out} is the light out-coupling efficiency from the device to free space [64].

To achieve maximum brightness, LED materials should facilitate strong carrier transport which is required to efficiently inject carriers. Additionally, a balance between the injection of both carrier types (electrons and holes) is necessary. To maximize the overall EL EQE, there are a number of factors that must be taken into account. The γ and PLQY strongly depend on the lifetime of the carriers within the active layer. Therefore, carrier blocking layers are typically introduced in solution-processed LEDs to trap the carriers and prevent leakage into the electrodes. In addition, to maximize the PLQY, complete surface passivation is required to eliminate trap states associated with nanomaterial surfaces and suppress non-radiative recombination. To maximize σ_{out}, the active layer is usually very thin to avoid photon re-absorption, and careful design of the optical structure of the LED together with packaging

optics is necessary.

References

[1] Mengxia Liu, Oleksandr Voznyy, Randy Sabatini, F Pelayo García de Arquer, Rahim Munir, Ahmed Hesham Balawi, Xinzheng Lan, Fengjia Fan, Grant Walters, Ahmad R Kirmani, et al. "Hybrid organic–inorganic inks flatten the energy landscape in colloidal quantum dot solids". In: *Nature materials* 16.2 (2017), p. 258.

[2] Ebuka S Arinze, Botong Qiu, Nathan Palmquist, Yan Cheng, Yida Lin, Gabrielle Nyirjesy, Gary Qian, and Susanna M Thon. "Color-tuned and transparent colloidal quantum dot solar cells via optimized multilayer interference". In: *Optics Express* 25.4 (2017), A101–A112.

[3] Shun-Chi Chang, Jie Liu, Jayesh Bharathan, Yang Yang, Jun Onohara, and Junji Kido. "Multicolor organic light-emitting diodes processed by hybrid inkjet printing". In: *Advanced Materials* 11.9 (1999), pp. 734–737.

[4] Vanessa Wood, Matthew J Panzer, Jianglong Chen, Michael S Bradley, Jonathan E Halpert, Moungi G Bawendi, and Vladimir Bulović. "Inkjet-printed quantum dot–polymer composites for full-color ac-driven displays". In: *Advanced Materials* 21.21 (2009), pp. 2151–2155.

[5] Mengyu Chen, Hui Yu, Stephen V Kershaw, Haihua Xu, Shuchi Gupta, Frederik Hetsch, Andrey L Rogach, and Ni Zhao. "Fast, air-stable infrared photodetectors based on spray-deposited aqueous HgTe quantum dots". In: *Advanced Functional Materials* 24.1 (2014), pp. 53–59.

[6] Illan J Kramer, James C Minor, Gabriel Moreno-Bautista, Lisa Rollny, Pongsakorn Kanjanaboos, Damir Kopilovic, Susanna M Thon, Graham H Carey, Kang Wei Chou, David Zhitomirsky, et al. "Efficient spray-coated colloidal quantum dot solar cells". In: *Advanced materials* 27.1 (2015), pp. 116–121.

[7] Hanjie Chen, Zhengyuan Xu, Qian Gao, and Shangbin Li. “A 51.6 Mb/s experimental VLC system using a monochromic organic LED”. In: *IEEE Photonics Journal* 10.2 (2018), pp. 1–12.

[8] Dong-Un Jin, Jae-Sup Lee, Tae-Woong Kim, Sung-Guk An, Denis Straykhilev, Young-Shin Pyo, Hyung-Sik Kim, Dong-Bum Lee, Yeon-Gon Mo, Hye-Dong Kim, et al. “65.2: Distinguished Paper: World-Largest (6.5") Flexible Full Color Top Emission AMOLED Display on Plastic Film and Its Bending Properties”. In: *SID Symposium Digest of Technical Papers*. Vol. 40. 1. Wiley Online Library. 2009, pp. 983–985.

[9] Jason P Clifford, Gerasimos Konstantatos, Keith W Johnston, Sjoerd Hoogland, Larissa Levina, and Edward H Sargent. “Fast, sensitive and spectrally tuneable colloidal-quantum-dot photodetectors”. In: *Nature nanotechnology* 4.1 (2009), p. 40.

[10] Jianhui Hou, Olle Inganäs, Richard H Friend, and Feng Gao. “Organic solar cells based on non-fullerene acceptors”. In: *Nature materials* 17.2 (2018), p. 119.

[11] Takuya Komoda, Hisahiro Sasabe, and Junji Kido. “Current Status of OLED Material and Process Technologies for Display and Lighting”. In: *2018 25th International Workshop on Active-Matrix Flatpanel Displays and Devices (AM-FPD)*. IEEE. 2018, pp. 1–4.

[12] AD Yoffe. “Low-dimensional systems: quantum size effects and electronic properties of semiconductor microcrystallites (zero-dimensional systems) and some quasi-two-dimensional systems”. In: *Advances in Physics* 51.2 (2002), pp. 799–890.

[13] Louis Brus. “Electronic wave functions in semiconductor clusters: experiment and theory”. In: *The Journal of Physical Chemistry* 90.12 (1986), pp. 2555–2560.

[14] Alexander H Ip, Susanna M Thon, Sjoerd Hoogland, Oleksandr Voznyy, David Zhitomirsky, Ratan Debnath, Larissa Levina, Lisa R Rollny, Graham H Carey, Armin Fischer, et al. “Hybrid passivated colloidal quantum dot solids”. In: *Nature nanotechnology* 7.9 (2012), p. 577.

[15] Steven A McDonald, Gerasimos Konstantatos, Shiguo Zhang, Paul W Cyr, Ethan JD Klem, Larissa Levina, and Edward H Sargent. “Solution-processed PbS quantum dot infrared photodetectors and photovoltaics”. In: *Nature materials* 4.2 (2005), p. 138.

[16] Iwan Moreels, Guy Allan, Bram De Geyter, Ludger Wirtz, Christophe Delerue, and Zeger Hens. "Dielectric function of colloidal lead chalcogenide quantum dots obtained by a Kramers-Krönig analysis of the absorbance spectrum". In: *Physical Review B* 81.23 (2010), p. 235319.

[17] Xiaoqi Fu, Yi Pan, Xin Wang, and John R Lombardi. "Quantum confinement effects on charge-transfer between PbS quantum dots and 4-mercaptopyridine". In: *The Journal of chemical physics* 134.2 (2011), p. 024707.

[18] Iwan Moreels, Karel Lambert, Dries Smeets, David De Muynck, Tom Nollet, José C Martins, Frank Vanhaecke, Andre Vantomme, Christophe Delerue, Guy Allan, et al. "Size-dependent optical properties of colloidal PbS quantum dots". In: *ACS nano* 3.10 (2009), pp. 3023–3030.

[19] Jianbing Zhang, Ryan W Crisp, Jianbo Gao, Daniel M Kroupa, Matthew C Beard, and Joseph M Luther. "Synthetic conditions for high-accuracy size control of PbS quantum dots". In: *The journal of physical chemistry letters* 6.10 (2015), pp. 1830–1833.

[20] Margaret A Hines and Gregory D Scholes. "Colloidal PbS nanocrystals with size-tunable near-infrared emission: observation of post-synthesis self-narrowing of the particle size distribution". In: *Advanced Materials* 15.21 (2003), pp. 1844–1849.

[21] CBea Murray, David J Norris, and Moungi G Bawendi. "Synthesis and characterization of nearly monodisperse CdE (E= sulfur, selenium, tellurium) semiconductor nanocrystallites". In: *Journal of the American Chemical Society* 115.19 (1993), pp. 8706–8715.

[22] Hyekyoung Choi, Jae-Hyeon Ko, Yong-Hyun Kim, and Sohee Jeong. "Steric-hindrance-driven shape transition in PbS quantum dots: understanding size-dependent stability". In: *Journal of the American Chemical Society* 135.14 (2013), pp. 5278–5281.

[23] Ying-Fan Liu and Jun-Sheng Yu. "Selective synthesis of CdTe and high luminescence CdTe/CdS quantum dots: the effect of ligands". In: *Journal of Colloid and Interface Science* 333.2 (2009), pp. 690–698.

[24] Liangfeng Sun, Joshua J Choi, David Stachnik, Adam C Bartnik, Byung-Ryool Hyun, George G Malliaras, Tobias Hanrath, and Frank W Wise. "Bright infrared quantum-dot light-emitting diodes through inter-dot spacing control". In: *Nature nanotechnology* 7.6 (2012), p. 369.

[25] Oleksandr Voznyy, Larissa Levina, Fengjia Fan, Grant Walters, James Z Fan, Amirreza Kiani, Alexander H Ip, Susanna M Thon, Andrew H Proppe, Mengxia Liu, et al. "Origins of stokes shift in PbS nanocrystals". In: *Nano letters* 17.12 (2017), pp. 7191–7195.

[26] Rupert F Oulton, Volker J Sorger, DA Genov, DFP Pile, and X Zhang. "A hybrid plasmonic waveguide for subwavelength confinement and long-range propagation". In: *Nature Photonics* 2.8 (2008), p. 496.

[27] Yulan Fu, Xiaoyong Hu, Cuicui Lu, Song Yue, Hong Yang, and Qihuang Gong. "All-optical logic gates based on nanoscale plasmonic slot waveguides". In: *Nano letters* 12.11 (2012), pp. 5784–5790.

[28] Kathryn M Mayer and Jason H Hafner. "Localized surface plasmon resonance sensors". In: *Chemical reviews* 111.6 (2011), pp. 3828–3857.

[29] Xuanhua Li, Wallace Chik Ho Choy, Haifei Lu, Wei EI Sha, and Aaron Ho Pui Ho. "Efficiency enhancement of organic solar cells by using shape-dependent broadband plasmonic absorption in metallic nanoparticles". In: *Advanced Functional Materials* 23.21 (2013), pp. 2728–2735.

[30] Xi Chen, Baohua Jia, Jhantu K Saha, Boyuan Cai, Nicholas Stokes, Qi Qiao, Yongqian Wang, Zhengrong Shi, and Min Gu. "Broadband enhancement in thin-film amorphous silicon solar cells enabled by nucleated silver nanoparticles". In: *Nano letters* 12.5 (2012), pp. 2187–2192.

[31] Xiaofeng Fan, Weitao Zheng, and David J Singh. "Light scattering and surface plasmons on small spherical particles". In: *Light: Science & Applications* 3.6 (2014), e179.

[32] Craig F Bohren and Donald R Huffman. *Absorption and scattering of light by small particles*. John Wiley & Sons, 2008.

[33] Gustav Mie. "Beiträge zur Optik trüber Medien, speziell kolloidaler Metallösungen". In: *Annalen der physik* 330.3 (1908), pp. 377–445.

[34] Colleen L Nehl, Hongwei Liao, and Jason H Hafner. "Optical properties of star-shaped gold nanoparticles". In: *Nano letters* 6.4 (2006), pp. 683–688.

[35] Huanjun Chen, Lei Shao, Qian Li, and Jianfang Wang. "Gold nanorods and their plasmonic properties". In: *Chemical Society Reviews* 42.7 (2013), pp. 2679–2724.

[36] Max Planck. *The theory of heat radiation*. Courier Corporation, 2013.

[37] George B Rybicki and Alan P Lightman. *Radiative processes in astrophysics*. John Wiley & Sons, 2008.

[38] William Shockley and Hans J Queisser. "Detailed balance limit of efficiency of p-n junction solar cells". In: *Journal of applied physics* 32.3 (1961), pp. 510–519.

[39] Alexis De Vos. "Detailed balance limit of the efficiency of tandem solar cells". In: *Journal of Physics D: Applied Physics* 13.5 (1980), p. 839.

[40] Graham H Carey, Ahmed L Abdelhady, Zhijun Ning, Susanna M Thon, Osman M Bakr, and Edward H Sargent. "Colloidal quantum dot solar cells". In: *Chemical reviews* 115.23 (2015), pp. 12732–12763.

[41] Junghwan Kim, Olivier Ouellette, Oleksandr Voznyy, Mingyang Wei, Jongmin Choi, Min-Jae Choi, Jea Woong Jo, Se-Woong Baek, James Fan, Makhsud I Saidaminov, et al. "Butylamine-Catalyzed Synthesis of Nanocrystal Inks Enables Efficient Infrared CQD Solar Cells". In: *Advanced Materials* 30.45 (2018), p. 1803830.

[42] J Engelfried, I Filimonov, J Kilmer, A Kozhevnikov, V Kubarovsky, V Molchanov, A Nemitkin, E Ramberg, V Rud, and L Stutte. "The SELEX phototube RICH detector". In: *Nuclear Instruments and Methods in Physics Research Section A: Accelerators, Spectrometers, Detectors and Associated Equipment* 431.1-2 (1999), pp. 53–69.

[43] Changhong Chen, Xinjian Yi, Xingrong Zhao, and Bifeng Xiong. "Characterizations of VO2-based uncooled microbolometer linear array". In: *Sensors and Actuators A: Physical* 90.3 (2001), pp. 212–214.

[44] Geoffrey Boothroyd. "Photographic technique for the determination of metal cutting temperatures". In: *British Journal of Applied Physics* 12.5 (1961), p. 238.

[45] Andre Dreyhaupt, Stephan Winnerl, Thomas Dekorsy, and Manfred Helm. "High-intensity terahertz radiation from a microstructured large-area photoconductor". In: *Applied Physics Letters* 86.12 (2005), p. 121114.

[46] E Munoz, E Monroy, JA Garrido, I Izpura, FJ Sánchez, MA Sánchez-Garcıa, E Calleja, B Beaumont, and P Gibart. "Photoconductor gain mechanisms in GaN ultraviolet detectors". In: *Applied physics letters* 71.7 (1997), pp. 870–872.

[47] Anders Elfving, Göran V Hansson, and W-X Ni. "SiGe (Ge-dot) heterojunction phototransistors for efficient light detection at 1.3–1.55 μm". In: *Physica E: Low-dimensional Systems and Nanostructures* 16.3-4 (2003), pp. 528–532.

[48] Robert W Sandage and J Alvin Connelly. "A fingerprint opto-detector using lateral bipolar phototransistors in a standard CMOS process". In: *Proceedings of International Electron Devices Meeting*. IEEE. 1995, pp. 171–174.

[49] RJ Fonck, R Ashley, R Durst, SF Paul, and G Renda. "Low-noise photodiode detector for optical fluctuation diagnostics". In: *Review of scientific instruments* 63.10 (1992), pp. 4924–4926.

[50] John Bowers and Charlesa Burrus. "Ultrawide-band long-wavelength pin photodetectors". In: *Journal of Lightwave Technology* 5.10 (1987), pp. 1339–1350.

[51] P Peumans, V Bulović, and SR Forrest. "Efficient, high-bandwidth organic multilayer photodetectors". In: *Applied Physics Letters* 76.26 (2000), pp. 3855–3857.

[52] Letian Dou, Yang Micheal Yang, Jingbi You, Ziruo Hong, Wei-Hsuan Chang, Gang Li, and Yang Yang. "Solution-processed hybrid perovskite photodetectors with high detectivity". In: *Nature communications* 5 (2014), p. 5404.

[53] Linfeng Hu, Jian Yan, Meiyong Liao, Limin Wu, and Xiaosheng Fang. "Ultrahigh external quantum efficiency from thin SnO2 nanowire ultraviolet photodetectors". In: *small* 7.8 (2011), pp. 1012–1017.

[54] Wei Zhang, Jin Xu, Wei Ye, Yang Li, Zhiqiang Qi, Jiangnan Dai, Zhihao Wu, Changqing Chen, Jun Yin, Jing Li, et al. "High-performance AlGaN metal–semiconductor–metal solar-blind ultraviolet photodetectors by localized surface plasmon enhancement". In: *Applied Physics Letters* 106.2 (2015), p. 021112.

[55] Ethan JD Klem, Chris Gregory, Dorota Temple, and Jay Lewis. "PbS colloidal quantum dot photodiodes for low-cost SWIR sensing". In: *Infrared Technology and Applications XLI*. Vol. 9451. International Society for Optics and Photonics. 2015, p. 945104.

[56] S Kalchmair, H Detz, GD Cole, AM Andrews, P Klang, M Nobile, R Gansch, C Ostermaier, W Schrenk, and G Strasser. “Photonic crystal slab quantum well infrared photodetector”. In: *Applied Physics Letters* 98.1 (2011), p. 011105.

[57] Jessie Rosenberg, Rajeev V Shenoi, Sanjay Krishna, and Oskar Painter. “Design of plasmonic photonic crystal resonant cavities for polarization sensitive infrared photodetectors”. In: *Optics express* 18.4 (2010), pp. 3672–3686.

[58] Isamu Akasaki, Hiroshi Amano, Shuji Nakamura, and S Nakamura. “The Nobel Prize in Physics 2014”. In: *Nobelprize. org. Nobel Media AB* (2014).

[59] CH Chuen and YT Tao. “Highly-bright white organic light-emitting diodes based on a single emission layer”. In: *Applied physics letters* 81.24 (2002), pp. 4499–4501.

[60] Zhi-Kuang Tan, Reza Saberi Moghaddam, May Ling Lai, Pablo Docampo, Ruben Higler, Felix Deschler, Michael Price, Aditya Sadhanala, Luis M Pazos, Dan Credgington, et al. “Bright light-emitting diodes based on organometal halide perovskite”. In: *Nature nanotechnology* 9.9 (2014), p. 687.

[61] Sang Hyun Park, Ara Hong, Jong-Hoon Kim, Heesun Yang, Kwangyeol Lee, and Ho Seong Jang. “Highly bright yellow-green-emitting CuInS2 colloidal quantum dots with core/shell/shell architecture for white light-emitting diodes”. In: *ACS applied materials & interfaces* 7.12 (2015), pp. 6764–6771.

[62] Polina O Anikeeva, Jonathan E Halpert, Moungi G Bawendi, and Vladimir Bulovic. “Quantum dot light-emitting devices with electroluminescence tunable over the entire visible spectrum”. In: *Nano letters* 9.7 (2009), pp. 2532–2536.

[63] Aditya Sadhanala, Shahab Ahmad, Baodan Zhao, Nadja Giesbrecht, Phoebe M Pearce, Felix Deschler, Robert LZ Hoye, Karl C GoÌĹdel, Thomas Bein, Pablo Docampo, et al. “Blue-green color tunable solution processable organolead chloride–bromide mixed halide perovskites for optoelectronic applications”. In: *Nano letters* 15.9 (2015), pp. 6095–6101.

[64] Stefano Toffanin Michele Muccini. “Photonic Properties of OLETs”. In: *Organic Light-Emitting Transistors: Towards the Next Generation Display Technology*. John Wiley & Sons, Ltd, 2016, pp. 201–241. ISBN: 978-1-119-18997-8.

Chapter 3

Nanophotonic design for optoelectronics

3.1 Improved performance of visible-blind UV photodetectors by nanoheterojunction incorporation

This section is adapted from Ref. [1]. Reprinted with permission from Applied Physics Letters 107, no. 24, 241108, "High-performing visible-blind photodetectors based on SnO_2/CuO nanoheterojunctions," by Xie, Ting, Md Rezaul Hasan, Botong Qiu, Ebuka S. Arinze, Nhan V. Nguyen, Abhishek Motayed, Susanna M. Thon, and Ratan Debnath, copyright © 2015. In this project I was in charge of the optical simulations and enhancement mechanism with help form Ebuka Arinze.

3.1.1 Introduction and Background

Transparent oxide semiconductors (TOSs) have attracted considerable attention in recent years, due to their versatile applications in transparent thin-film

transistors,[2, 3] transparent electrodes,[4] and optoelectronics.[5, 6, 7] Visible-blind ultraviolet (UV) photodetectors (PDs) are of particular interest, owing to their broad application in digital imaging, missile plume detection, optical communications, and biomedical sensing.[8, 9, 10] Due to its wide bandgap and consequent transparency in the visible spectral region, SnO_2 has been demonstrated as a useful material for visible-blind UV photon detection.[11, 12, 13]

Typical n-SnO_2 PDs work as photoconductors with electrons as the majority carriers. In a photoconductor, absorption of photons with energy larger than the bandgap energy generates free carriers, leading to an increase in conductivity for a period known as the persistence time. The device conducts a single carrier type, and the persistence time can be lengthened by trapping of the non-conducting carrier type, leading to photoconductive gain and quantum efficiency of greater than 100%. At a specific operation bias, the photocurrent is measured as the response of the PD, which can be used to calculate the EQE (external quantum efficiency) and responsivity of the device.

Current SnO_2 thin-film PD technology is limited by low responsivity, especially at longer UV wavelengths.[14] Efforts to improve device performance have focused on achieving better crystal quality and building one-dimensional SnO_2 nanostructures.[10, 15, 16, 17] The reported ultrahigh responsivity[15] of SnO_2 based PDs indicates that SnO_2 is a promising material for high-performing PDs. Here, we build thin-film SnO_2 PDs using a novel, facile, and scalable approach to fabricate nanoscale p-n heterojunctions with enhanced

light absorption in the active material to improve the performance of UV PDs.

Nanorod-based heterojunctions consisting of p-CuO and n-SnO_2 have been previously developed for applications such as gas sensors.[18, 19] Our simplified PD device fabrication method consists of using rf-sputtering to deposit SnO_2 thin films and Cu nanoparticle (NP) clusters. The top layer of Cu NPs oxidizes in ambient to form CuO NP clusters, and the primary role of these clusters is to enhance absorption at the longer wavelength edge of the UV response in the PDs. We used finite-difference time-domain (FDTD) simulations to model the light absorption in devices with and without the CuO NPs and achieved good agreement with the experimental absorption spectra. Our electrical measurements indicated that the inclusion of the CuO NPs improved the responsivity of the PDs more than 5 fold compared to SnO_2-only devices.

3.1.2 Experimental Results and Discussion

The SnO_2 thin films were rf-sputtered using a SnO_2 target on sapphire substrates in a Denton Vacuum Discovery 550 sputtering system. The base pressure was kept at or below 6.7 x 10^{-4} Pa (5 x 10^{-6} Torr), and the substrate temperature was maintained at 325 $^{\circ}$ C to yield uniform films. The thickness of the deposited SnO_2 was measured using a J. A. Woollam M2000 ellipsometer and estimated to be (95 $\pm$ 2) nm.

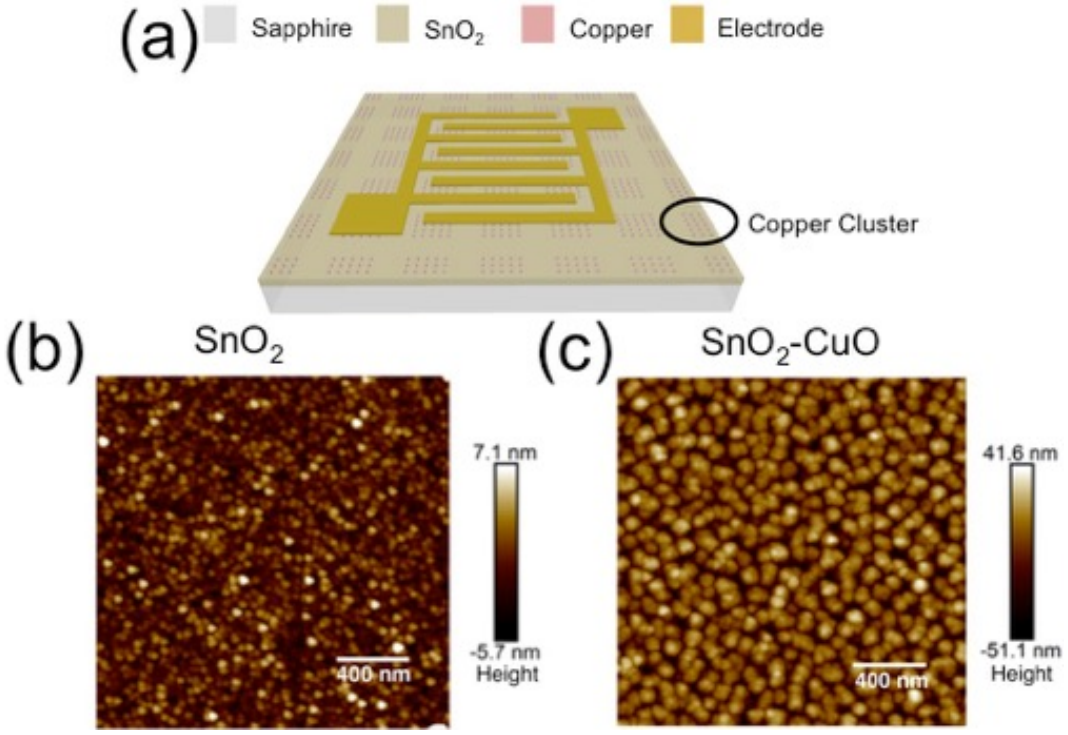

Figure 3.1: (a) Schematic of a SnO_2-CuO nanocluster PD device including the top interdigitated electrodes. Dimensions are not to scale. (b) High-resolution AFM image of an as-deposited SnO_2 film. (c) High-resolution AFM image of a SnO_2 film with a top layer of CuO nanoclusters.[1]

The Cu NP clusters were deposited on the SnO_2 films by rf-sputtering at room temperature. The deposition time was 185 seconds, and a shadow mask was used to form square-shaped clusters composed of self-assembled nanoparticles with a nominal height of 40-50 nm rather than continuous cluster films. The total areal size of the Cu clusters was 200 μm x 200 μm, and they were spaced by 200 μm, as shown in Figure 3.1a. Oxidation of the Cu nanoparticles occurred spontaneously during and immediately following the deposition, resulting in the formation of CuO NPs. X-ray photoelectron spectroscopy (XPS) measurements indicated that the final NP clusters are

primarily (> 95 %) composed of CuO, as shown in Figure 3.2b. Electron beam evaporation was used to deposit Ti/Al/Ti/Au interdigitated electrodes (IDEs) as the final step in the PD fabrication process. Figure 3.1a shows a device schematic of the entire structure.

The surface morphology of the SnO_2 and SnO_2-CuO films was measured using a Bruker Dimension FastScan atomic force microscope (AFM). Figures 3.1b and c show high-resolution AFM images of the bare SnO_2 film and the SnO_2 with a top layer of self-assembled CuO NPs. The measured root mean square (rms) surface roughness of the bare SnO_2 film was 1.8 nm, and the rms value increased to 13.8 nm after the addition of the CuO NPs. The grain sizes of the SnO_2 film and the CuO nanoclusters were estimated as (32.9 $\pm$ 13) nm and (74.6 $\pm$ 25) nm, respectively. A rough statistical analysis performed on the image in Figure 3.1c resulted in an average CuO NP surface density of 65 μm^{-2} and an average particle height of 45 nm. These estimated parameters were used in the FDTD simulations described below.

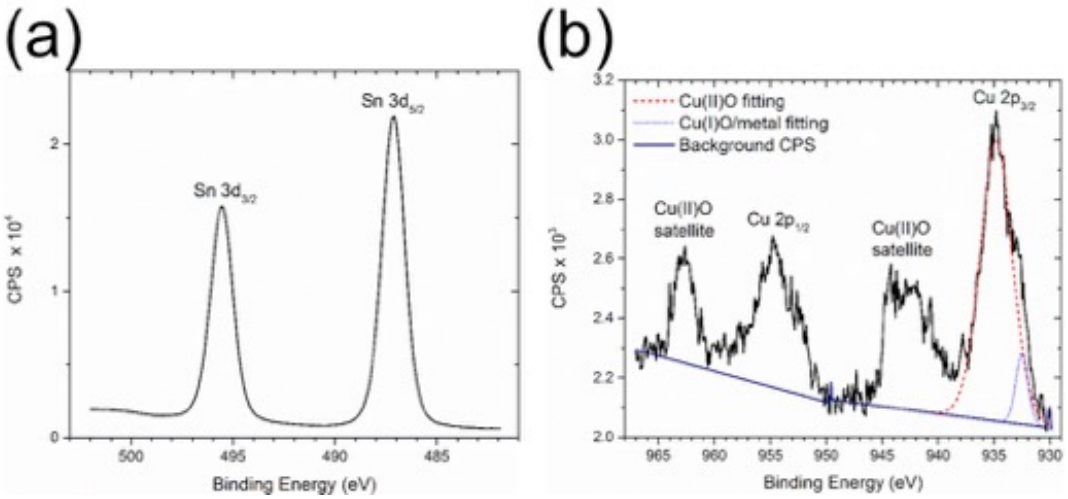

Figure 3.2: High-resolution XPS spectra of (a) the Sn 3d and (b) the Cu 2p regions of a SnO_2-CuO film. CPS is counts per second.[1]

We used XPS measurements to confirm the chemical identity of the SnO_2-CuO films. XPS curve-fitting and analysis was performed using CasaXPS software. The binding energies of the spectra were calibrated to the hydrocarbon peak at 284.8 eV. High-resolution XPS spectra of the Sn 3d and Cu 2p regions of the SnO_2-CuO film are shown in Figures 3.2a and b, respectively. As seen in Figure 3.2a, the Sn 3d 5/2 peak appears at a binding energy of (487.1 $\pm$ 0.1) eV with a satellite peak characteristic of Sn 3d 3/2 at (495.5 $\pm$ 0.1) eV, which is consistent with previously reported XPS data for SnO_2.[20] The Cu 2p region of the spectrum shows a combination of Cu-related states that can be identified by referring to published reports.[21, 22, 23] Curve-fitting of the Cu 2p region peaks (Figure 3.2b) was used to estimate that 95 at.% of the Cu content of the sample is in the form of Cu(II)O and the other 5 at.% is in the form of Cu(I)O or Cu metal. From these measurements, we concluded that the deposited Cu NPs are substantially oxidized to form CuO during and

after the deposition process.

The absorption spectra and absorption coefficients (α) of the SnO_2 and SnO_2-CuO films were measured using an Ocean Optics QE65000 spectrometer and a J. A. Woollam M2000 ellipsometer, respectively. Optical absorbance spectra of the SnO_2 and SnO_2-CuO films are shown in Figure 3.3b. A significant enhancement in the light absorption over the wavelength range of 250 nm to 475 nm is observed in the film decorated with CuO NPs compared to the bare SnO_2 film.

To verify the enhancement mechanism associated with the addition of the CuO NP clusters, we used FDTD simulations to calculate the optical properties of a 100 nm thick SnO_2 film with and without CuO nanoclusters on top. The simulated structure is shown in Figure 3.3a. The CuO NPs were modeled as randomly distributed elliptic paraboloids. The particle shape, dimensions and average surface densities were derived from the analysis of the AFM images (Figure 3.1c). Refractive indices for the SnO_2 film were obtained from ellipsometry measurements, and reported values were used for the refractive indices for the CuO[24] and sapphire[25] substrate. A broadband (200 nm - 1000 nm) plane wave incident from the nanocluster side of the device was used as the excitation source for the simulations.

Figures 3.3b and c show the experimental and simulated absorption spectra for the SnO_2 films with and without CuO NP clusters. The simulated and measured spectra show qualitative agreement in the effect of the CuO NPs on the increase in absorbance across all wavelengths in the plotted range, the apparent red shift of the absorption onset, and the change in shape of the

absorbance curve. Differences in quantitative agreement can be attributed to inhomogeneity in the NP size and density distributions, and uncertainty in the SnO_2 film thickness in the real devices.

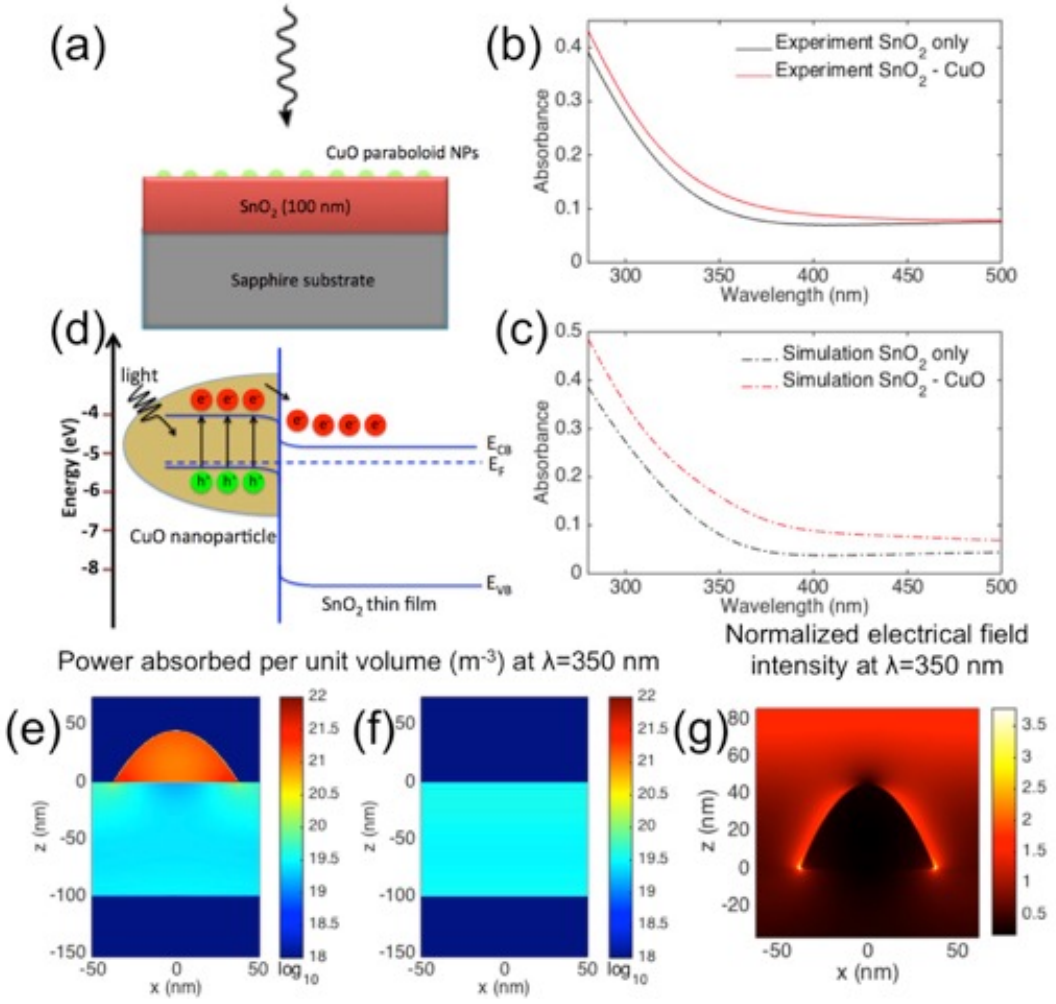

Figure 3.3: (a) Diagram of the setup for the FDTD simulations. A SnO_2 film thickness of 100 nm was used for the simulations with and without CuO NPs. The CuO NP clusters were modeled as elliptic paraboloids with heights of 45 nm and diameters of 75 nm. The CuO NPs were randomly distributed on the SnO_2 film with an average surface density of 65 μm^{-2}. The size and average density values of the NPs were based on AFM measurements of the real devices. (b) Measured and (c) FDTD simulated absorption spectra of the SnO_2 and SnO_2-CuO films. (d) Schematic band diagram illustrating the hypothesized electron transfer process in the CuO-SnO_2 nanoheterojunctions under irradiation. (e) Spatial cross-section of simulated power absorbed per unit volume at λ = 350 nm in a single CuO NP on a SnO_2 film and (f) in a bare SnO_2 film. (g) Spatial cross-section of simulated normalized electrical field intensity at λ = 350 nm for a single CuO NP on a SnO_2 film.[1]

The simulated spatial absorption profiles for a single CuO NP on a SnO_2

film and a bare SnO_2 film at a wavelength of 350 nm are plotted in Figure 3.3e and Figure 3.3f. The normalized electrical field intensity at a wavelength 350 nm is plotted in Figure 3.3g. There is an enhancement of the local electrical field intensity around the NP and strong associated absorption within the NP. We attribute the enhanced absorption in the composite devices to this effect. Our aim was to use this increase in absorption without relying on an increase in SnO_2 film thickness to improve the responsivity of the SnO_2-based photodetectors.

A schematic band diagram for the SnO_2/CuO pn-nanoheterojunctions is depicted in Figure 3(d) using energy levels reported for p-CuO[26] and n-SnO_2[27]. The nanoheterojunction structure takes advantage of the intense absorption in the CuO NPs to transfer a high density of photogenerated electrons from the p CuO NPs to the n-SnO_2 film, while the transfer of holes is hindered by the energy barrier at the junction. The smaller bandgap of CuO (1.35 eV[26]) results in increased absorption at the red edge of the UV spectrum, and the pn-heterojunction nature of the CuO/SnO_2 interface facilitates charge transfer upon illumination to increase the responsivity of the photodetector. Electrons injected into the conduction band of SnO_2 from the CuO increase the free majority carrier density in the photoconductive material, which could lead to a significant increase in photocurrent in the PD. Although the bandgap of CuO is small, the nanoscale structure of the CuO particles are predicted to allow the films to remain "visible-blind" due to poor in-coupling and low absorption in structures that are much smaller than the visible and infrared material photon absorption lengths.

Typical I-V characteristics of the SnO_2-only and CuO-SnO_2 devices measured in the dark and under UV-illumination are shown in Figure 4(a). The photocurrent generated in the PD with CuO NPs was almost double that of the SnO_2-only device under 290 nm wavelength illumination for all tested biases. The measured dark current for the CuO-SnO_2 PD was also larger than that of the SnO_2-only device, indicating that the conductivity of the CuO-SnO_2 composite film was larger than that of the SnO_2-only film.

To quantify the performance of the PDs, we used the photocurrent-to-dark current ratio, defined as:

$$Photocurrent - to - darkcurrentratio = \frac{I_{UV} - I_{dark}}{I_{dark}} \tag{3.1}$$

where I_{UV} is the current under UV illumination, and I_{dark} is the dark current at the same voltage. The CuO-SnO_2 PDs exhibited a PF of $\sim$ 592 at 1.2 V under 290 nm illumination.

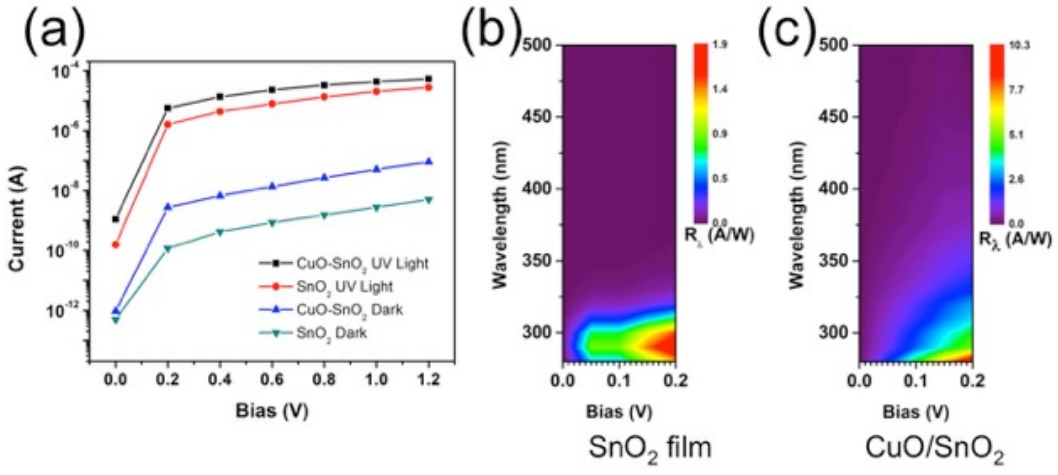

Figure 3.4: (a) ON/OFF I-V curves for SnO_2-only and CuO/SnO_2 PDs under UV illumination at a wavelength of 290 nm. (b) Responsivity as a function of bias and wavelength for SnO_2 and (c) SnO_2-CuO thin film photodetectors.[1]

Responsivities of the SnO_2 and SnO_2-CuO PDs were measured at various bias voltages under a spectrally filtered light source. The measurements, calibrated using a standard NIST silicon photodiode, were associated with a total uncertainty of $\pm$ 5 % (fractional). In order to obtain stable and reliable data, the photocurrent at each wavelength was measured with a delay of 180 seconds with respect to the illumination. The need for stable photocurrent operation precluded higher resolution measurements of the PD response time.

The UV photocurrent response of the PDs was recorded over a voltage range of 0 V to 1.2 V at an illumination wavelength of 290 nm, as shown in Figure 3.4a. In addition to light current enhancements, the dark current also increases after the SnO_2 surface is covered with the CuO NPs, despite the assumed formation of a depletion layer. This increase can be attributed to several potential mechanisms. The small amount of Cu(I)O or Cu metal visible in the XPS spectrum could lead to an increase in the dark current which could be ameliorated in future iterations by including a controlled oxidation step in the fabrication process. Additionally, the presence of defects close to the nanojunction interface could reduce carrier lifetimes, potentially act as dopants, and facilitate leakage paths, contributing to an increase in device dark current.

Figures 3.4b and c illustrate the spectral responsivity of the SnO_2 devices with and without CuO NPs in the low bias regime. The SnO_2-only PDs reached a maximum responsivity of 1.9 A/W at 0.2 V bias under 290 nm illumination, while the devices with CuO NP clusters exhibited a responsivity of 10.3 A/W at 0.2 V bias under 280 nm illumination. The incorporation of the

CuO NPs resulted in a greater than 5 fold improvement of the responsivity. Additionally, the SnO_2-only PD response had a sharp cutoff at around 320 nm in wavelength, whereas the SnO_2-CuO PDs displayed some response out to 340 nm in wavelength at low bias. The broadening of the spectral detection range can be attributed to the drastic enhancement of light absorption and charge transfer facilitated by the SnO_2-CuO nanoheterojunctions in the UVA spectral region. Although the responsivity of these devices is lower than that of PDs based on one-dimensional structures9,14, it is competitive with thin-film based UV PDs made from other traditional semiconductor materials.27 Additionally, this method produces robust structures without complex fabrication processes that operate at low bias, making it suitable for practical applications.

3.1.3 Conclusion

In summary, we have demonstrated high responsivity visible-blind UV PDs based on sputtered SnO_2-CuO nanoheterojunction films. We investigated the properties of the films using AFM and XPS measurements, confirming that the sputtered Cu forms self-assembled nanoparticle clusters that are composed primarily of Cu(II)O after air exposure. The peak responsivity reached a value of 10.3 A/W at a low bias of 0.2 V in the CuO-SnO_2 devices, representing a five-fold increase over the highest responsivity achieved in devices without CuO NPs. The performance enhancement is attributed to the intense local absorption of the CuO NPs and the charge transfer facilitated by the CuO-SnO_2 pn nanoheterojunction structures. Our approach of utilizing

CuO-based pn nanoheterojunctions to enhance the efficiency of visible-blind SnO_2 photodiodes represents a viable path for building UV optoelectronic devices based on cost-effective materials.

3.2 Limits of light trapping via plasmonic enhancement in absorbing media

This section is adapted from Ref. [28]. Reprinted with permission from ACS Photonics 3, no. 2, 158-173, "Plasmonic Nanoparticle Enhancement of Solution-Processed Solar Cells: Practical Limits and Opportunities," by Arinze, Ebuka S., Botong Qiu, Gabrielle Nyirjesy, and Susanna M. Thon, copyright © 2016.

The search for sustainable and cost-competitive alternatives to fossil fuel-based energy sources has driven developments in solution-processed solar cells. These technologies seek to reduce manufacturing and processing costs as well as improve device efficiencies over traditional and thin-film bulk semiconductor platforms. The low temperature roll-to-roll production methods, solution-based fabrication techniques and high efficiency potential make materials such as polymers, hybrid perovskites, and colloidal quantum dots attractive technologies. However, the electronic transport lengths in most solution-processed materials are smaller than the photon absorption lengths, especially at near infrared wavelengths, due to their nanostructured nature and associated interface-related defects and impurities. This is referred to as the "absorption-extraction compromise" whereby the material thickness required for complete absorption results in incomplete extraction of the photogenerated charge carriers.

Attempts to improve the efficiencies of solution-processed devices have included engineering of the absorbing material,[29, 30, 31, 32] design of new device architectures,[33, 34, 35, 36, 37] and incorporation of light trapping techniques to decrease the effective film absorption lengths.[38, 39, 40, 41, 42, 43] Introducing plasmonic elements, which enhance the interaction of light with matter in metallic structures on the nanoscale, has been of particular interest to the field due to their minimum perturbation of the device structure and successful deployment for related optoelectronic device applications.[44, 45, 46, 46, 47, 48, 49]

Various efforts to introduce plasmonic enhancers into solution-processed photovoltaic cells have been tested, some of which will be reviewed in the following section. However, absolute photocurrent and power conversion efficiency improvements have been relatively limited thus far, partially due to the difficulty in systematic evaluation of the optimum plasmonic nanoparticle design for integration with specific photovoltaic materials. Here, we provide an overview of the field of embedded plasmonic-enhanced solution processed solar cells. We then develop an analytical model to systematically evaluate the practical potential of plasmonic enhancements in thin film materials. We compare the photocurrent enhancements predicted by our model to simulation and experimental results for three different systems. Finally, we use our model to make specific suggestions for the field moving forward, focusing on the optimum plasmonic nanoparticle material type, material shape, and concentration for realizing maximum potential enhancements for different systems.

3.2.1 Solution Processed Solar Cells

Compared to traditional bulk semiconductors, solution-processed solar cell materials typically have shorter charge transport lengths, stronger exciton binding energies, and larger electronic trap state densities due to the heterogeneity of their structures arising from the low-energy fabrication and processing procedures. Additionally, flexibility in doping of the materials is generally lacking. Therefore, solution-processed solar cell architectures have been designed to engineer around these issues. Taking inspiration from electrochemical cells, most solution-processed photovoltaic devices employ heterointerfaces, which can be structured to enhance charge separation and collection while minimizing the thickness of the active material.

Initial OPV architectures involving a bilayer donor-acceptor planar heterojunction[50] suffered from the "exciton-diffusion" bottleneck that resulted from the small diffusion lengths.[51, 52, 53, 54, 55] This led to the development of the bulk heterojunction architecture, in which the acceptor and donor phases are blended to form a high interfacial area mixture.[56, 57] This architecture is limited by the ability to optimally distribute charge separation interfaces and facilitate appropriate conduction channels.[58, 59, 60]

The highest-performing CQD photovoltaic devices use a heterojunction architecture in which the CQD medium forms a junction with an n-type wide band gap semiconductor such as TiO_2 or ZnO.[61] Control over the CQD film doping,[62] band alignment,[63] and structuring of the electrodes[29] have led to the development of advanced architectures that utilize multiple CQD film types, although high electronic trap state densities still limit performance.[64]

In the case of perovskite solar cells, sensitizing-type architectures produced most of the initial results in the field. The perovskite material is infiltrated into an electron-extracting[37, 65, 66, 67, 68] or insulating[32, 69, 70] mesoporous layer (usually TiO_2 and Al_2O_3 respectively) and topped with a hole transporting material. With advances in the growth of long-diffusion-length large-domain single crystal perovskites,[71, 72] the field is trending towards more conventional planar cell designs in which the perovskite film is sandwiched between electron- and hole-extracting electrodes.

The limited carrier transport lengths necessitate careful engineering of solution processed solar cell device architectures in order to maximize absorption and achieve the highest possible efficiencies. This problem is magnified at longer photon wavelengths near the band gap energy where absorption lengths can exceed carrier transport lengths by more than an order of magnitude in OPV and CQD materials, making light trapping a vital component of successful device designs.

3.2.2 Light Trapping for Photovoltaics

As a technique for absorption enhancement, the idea of light trapping in thick and thin optical films has been studied for decades.[73, 74, 75, 76] Conventionally, light trapping employs total internal reflection as the primary confinement mechanism and is achieved through structural manipulation of the device layers. The maximum absorption enhancement factor (Yablonovitch Limit or Lambertian Limit [73, 74, 75]) for conventional thin-film light-trapping strategies is $4n^2/sin^2\theta$, where n is the refractive index of the absorbing medium, and

θ is the angle of the emission cone in the medium surrounding the cell (also known as the acceptance angle). For normal incidence radiation ($\theta = \pi/2$), this upper limit can be further simplified to $4n^2$.

Recent theoretical work on light trapping has focused on the ultra sub-wavelength regime for optical film thicknesses. On the nanoscale, where light-matter interactions beyond the classical ray optics limit take place, it is theoretically possible to surpass the traditional Lambertian limit over specific wavelength ranges.[68] Using a rigorous electromagnetic approach, Yu et al. developed a statistical temporal coupled-mode theory of light trapping,[77] demonstrating that the enhancement factor can in theory be increased to 12x4n^2 over a virtually unlimited spectral bandwidth when optical modes exhibit deep-subwavelength-scale field confinement. Callahan et al. proposed that an elevated local density of optical states (LDOS) for the absorber is the key design element, and they demonstrated several nanostructured solar cell architectures that exceeded the Yablonovitch limit in simulation.[78]

Beyond evaluating the absorption enhancement factor, Schuster et al. proposed a figure of merit called light trapping efficiency (LTE), which is the ratio of the total current gain achieved in a device to the theoretical maximum current gain achievable in an ideal Lambertian scattering system.[79] Using LTE as a metric, they demonstrated that multiple theoretical and experimental photonic structures could be used to approach the enhancement limit.[79] Plasmonic enhancement strategies ideally fall under the category of approaches that can be used exceed the Lambertian limit.

3.2.3 Embedded Plasmonic Enhancers

The collective oscillations of the free electrons at the surface of a conductor are known as surface plasmons. These excitations couple strongly to incident electromagnetic radiation and are able to propagate along a metal-dielectric interface as surface plasmon polaritons. Plasmons can be excited at optical frequencies in materials such as gold and silver. In nanoscale structures, localized surface plasmon resonances (LSPRs) result in strong local field enhancement. This nanophotonic effect can be used to circumvent the traditional diffraction limits, and can result in the scattering of incoming light into guided modes in a thin film material with embedded plasmonic nanoparticles. Plasmonic elements have been applied in diverse applications such as nanoscale sensing,[80, 81, 82] light emitting diodes,[83, 84, 85] lasers,[86, 87, 88] photon detection,[89] information processing,[90] and photovoltaics.[42, 91, 92, 93, 94, 95]

Embedded plasmonic structures are of particular interest for solution-processed photovoltaic devices, such as those based on organic, hybrid inorganic-organic perovskite, and colloidal quantum dot thin film materials. Several reports study the integration of plasmonic structures into such devices with demonstrated increases in optical absorption.[91, 92, 94, 96] Embedded plasmonic structures within the absorbing medium are of particular interest for solution-processed technologies since the materials growth techniques are uniquely compatible with hybrid inclusions, whereas bulk semiconductor systems must rely on surface-based plasmonic in-couplers or scatterers.[97, 98, 99, 100, 101, 102]

Plasmonic nanostructures can be spatially placed at the top of, within, or

at the base of solution-processed devices. Placing the plasmonic nanoparticles within the active layer rather than in or on top of contact or buffer layers has several advantages. Mixing the plasmonic materials into the active layer of the cell can help to reduce reflection losses that occur before the light reaches the active layer and increase wave-guiding within the absorbing medium.[103, 104, 105] Finally, the near-field effects associated with LSPRs can be used to enhance absorption within the active layer if there is a strong spatial-field overlap with the absorbing medium. Embedded plasmonic schemes make use of this strong local field enhancement without significantly disrupting the device structure as in conventional light trapping designs. While this perspective focuses on embedded nanoparticle plasmonic enhancement strategies, non-embedded plasmonic strategies have been explored in-depth in the field, due to the ease of design and fabrication associated with integrating top- and bottom-device structures without disrupting the active layers. These schemes include placing metallic nanoparticles and nanostructured gratings outside the active layers for light in-coupling and trapping.[106, 107, 108, 109, 110, 111, 112, 113, 114, 115] Symmetric metallic nanostructured gratings, either 1D or 2D nanostructures, can be designed for effective light coupling to surface plasmon polariton (SPP) modes that strongly confine light at the interface, resulting in light concentration or preferential scattering into the active layer.

Examples of these methods include the design and integration of 2D SPP gratings for incident light coupling at the exciton peak wavelength in a CQD optoelectronic device.[115] A peak absorption enhancement factor of 3 was observed at the target wavelength. Additionally, the short-circuit current

in the light trapping spectral range (640 nm to 1100 nm) was observed to increase by 41%. In another study for OPVs,[112] a 14.8% improvement in efficiency was observed due to the integration of Ag nanoparticle films at the front electrode for preferential forward scattering into the active layer. In this plasmonic scheme, the Ag nanoparticle film was self-assembled via thermal evaporation and subsequent annealing.

In general, the propensity of plasmonic nanoparticles embedded within the active layer itself to serve as recombination sites for exciton quenching[116] has led to extensive exploration of plasmonic enhancement schemes that take advantage of scattering and light coupling from the electrode layers. However, the potential for high near-field enhancements from plasmonic particles embedded within the active layer provides motivation for further exploring embedded nanoparticle schemes.

The field of embedded plasmonic enhancement schemes for solution processed solar cells has advanced rapidly in recent years. Plasmonic particles of different shapes and sizes have been studied in organic photovoltaic (OPV), colloidal quantum dot (CQD), and perovskite solar cells. Large photocurrents have been demonstrated, although relative power conversion efficiency (PCE) enhancements have remained under 16% for films with PCE values of over 5%.

Table 3.1 summarizes the progress so far in embedded plasmonic enhancement schemes for solution-processed solar cells. Gold and silver are the most commonly used plasmonic materials, and they have also been combined with

oxide cores or shells.[43, 117, 118] The nanoparticles in the summarized studies ranged in size from 5 - 150 nm and were embedded at concentrations of 1 - 15 wt.%. The maximum PCE of 16.3% was achieved in a perovskite solar cell.[118] Maximum PCEs of 7.1% and 6.9% were achieved through plasmonic enhancement in OPVs and CQD solar cells, respectively.[104, 117] Although many potential nanoplasmonic enhancement schemes have been explored,[44, 94, 95, 97, 118, 119, 120, 121, 122, 123, 124, 125] experimental realizations of integrated plasmonic designs have yet to lead to record device efficiencies, mainly due to loss of the parasitic absorption by the plasmonic nanoparticles.[126, 77, 127, 128, 129]

3.2.3.1 Organic Photovoltaics

Plasmonic particles have been embedded within or between the active layers and selective contacts in OPV devices.[103, 104, 105, 121, 130, 131, 132, 133, 134] Typical OPVs have an active layer that consists of electron-donor and electron-acceptor materials.

One study[104] incorporated chemically-synthesized 40 nm silver nanoclusters into the active layer of a poly[N-9"-hepta-decanyl-2,7-carbazole-alt-5,5-(4′,7′-di-2-thienyl-2′,1′,3′-benzothiadiazole) (PCDTBT): [6,6]-phenyl-C70-butyric acid methyl ester ($PC_{70}BM$) bulk heterojunction (BHJ) solar cell to improve the efficiency. The nanoclusters exhibited a maximum absorbance peak near 420 nm. A 12.7% improvement in PCE was obtained by optimizing the weight percentage of the nanoclusters in the active layer. This enhancement was mainly due to a 7.6% increase in the short-circuit current density

Plasmonic Material (Shape)	Plasmonic Nanoparticle Size (nm)	Plasmonic Nanoparticle Concentration	Max. J_{SC} (mA/cm_2)	J_{SC} Enhancement	Max. PCE (%)	PCE Enhancement
Au (Octahedron)[130]	45	$2x10^{11}cm^{-3}$	10.22	11.6%	4.24	18.8%
Au (Sphere)[121]	30-40	20% by vol.	10.18	13.7%	4.19	20.4%
Au (Truncated Octahedron)[103]	70	5 wt.%	11.16	8.3%	6.45	11.8%
Ag (Nanocluster)[104]	40	1 wt.%	11.61	7.6%	7.1	12.7%
Au (Sphere)[105]	18	0.5 wt.%	4.8	15.7%	2.17	32.3%
Ag (Sphere)[131]	5-15	1:16 wt. ratio (Ag:P3HT)	8.9	1.1%	3.3	-2.9%
Ag (Truncated Octahedron)[132]	80	15 wt.%	8.7	19.2%	3.2	88.2%
Au (Sphere and Prism)[133]	20 and 60x10	2 wt.%	10.61	18%	4.3	19.4%
Au (Sphere)[134]	30	1 wt.%	15.3	-0.1%	7.02	6.7%
Au-Ag (Popcorn Alloy)[135]	150±50	0.7 wt.% TiO_2	16.46	6.1%	10.3	15.7%
Au-SiO_2 (Sphere)[136]	80/8 (core/shell)	0.9 wt.%	15.3	13.5%	9.5	13%
Au-TiO_2 (Sphere)[118]	40/2 (core/shell)	2.2 wt.%	22	8.9%	16.3	12.4%
Au (Sphere)[137]	5	0.3% by vol.	29.45	42.2%	4.5	12.5%
Ag (Hemisphere)[138]	40	33% surface coverage	8.5	19.4%	0.68	58.1%
SiO_2-Au (Sphere)[117]	15/60 (core/shell)	10 μm^{-2}	24.5	13%	6.9	11%

Table 3.1: Summary of selected plasmonic enhancement demonstrations in OPV, Perovskite, and CQD solar cells.[28]

(J_{SC}) and an associated reduction in the cell series resistance.

The addition of 70 nm truncated gold octahedral nanoparticles at optimized concentrations (5 wt.%) to the BHJ active layer in another study[103] resulted in consistent PCE improvements in fabricated devices. Other shapes, including Ag nanoparticles and nanoprisms mixed into the buffer layer of an OPV cell, [133] have also been used to realize wide-band absorption enhancements. Generally, relative PCE improvements on the order of 10% have been demonstrated in plasmonically enhanced OPV devices, mainly due to increases in J_{SC}. Associated compromises in the open-circuit voltage (V_{OC}) and fill factor (FF) are the prime reasons why these systems have been unable to rival the record efficiencies in the field.

3.2.3.2 Perovskite Solar Cells

Embedded plasmonic schemes have been explored only recently in perovskite solar cells, due to the relative novelty of this technology.[43, 118, 135] One demonstration enhanced the PCE of a perovskite solar cell by 12.4% by incorporating 40 nm silver-core nanoparticles with 2 nm TiO_2 shells through a low-temperature processing route.[118] The nanoparticles were added to the mesoporous Al_2O_3 scaffold layer, which was infiltrated with methylammonium lead iodide perovskite material.

Another study in the perovskite material system achieved a relative PCE enhancement of 15.7%.[135] A broadband absorption enhancement was demonstrated through the addition of Au-Ag alloy popcorn-shaped nanoparticles to the device. These nanoparticles were synthesized through a co-reduction

of $HAuCl_4$ and $AgNO_3$ and had an average size of 150 $\pm$ 50 nm. The nanoparticles were embedded in the mesoporous TiO_2 at a concentration of 0.7 wt.%.[135]

Higher efficiencies have been achieved in perovskite solar cells compared to OPV devices, and therefore these devices have less to gain from plasmonic enhancement schemes. The high efficiency is due to both substantial absorptivity near the band gap energy and superior charge transport. However, plasmonic enhancements could potentially enable materials savings even in high efficiency systems.

3.2.3.3 Colloidal Quantum Dot Solar Cells

Several different device architectures have been employed to make high-performing CQD solar cells.[139, 117, 140, 141, 142, 136, 143, 144, 137, 138, 145] All consist of close-packed CQD films sandwiched between selective transparent and reflective contacts.[143] Like OPV devices, CQD cells must overcome an absorption-extraction compromise to reach high performance, and several plasmonic enhancement strategies have been deployed to address this compromise.

To enhance the absorption specifically in the infrared regime, a study[117] added 120 nm diameter core-15 nm shell SiO2-Au core-shell nanoparticles to the active layer of a depleted heterojunction cell. In the lead sulfide (PbS) matrix, the nanoshells exhibit an LSPR peak at 820 nm. An enhancement in infrared photocurrent led to an 11% PCE improvement over a control device. [117]

Absorption enhancements in the active layer of a CQD solar cell have also been achieved by using the near field enhancement associated with small (5 nm-diameter) Au nanoparticles instead of focusing on far-field scattering gains.[137] The study demonstrated evidence of hot-electron transfer directly from the excited metal particles to the PbS semiconductor nanocrystals. The best performing cell had a 12.5% PCE improvement over a non-plasmonic device. [137]

Plasmonic particles can play electronic as well as optical roles in CQD solar cells. One study built an Ag nanoparticle - PbS CQD nano-Schottky junction device by depositing self-assembled 40 nm diameter Ag hemispheres that covered 33% of the ITO contact.[138] The PCE was enhanced by 58.1% compared to the fabricated control devices, which used a planar silver architecture. The improved performance was attributed to the modified absorption profile due to the enhanced optical field around the nanoparticles. This ensured that carriers were generated close to the metal-semiconductor interface within the depletion region.

Generally, plasmonically enhanced CQD devices have benefited from absorption improvements near the weakly-absorbing quantum dot band gap edge. The overall PCE enhancements have generally been weakened by mild loss in V_{OC} and FF.

3.2.3.4 Summary

The largest relative improvements in all three materials systems were achieved in cells with low starting efficiencies and device absorption.[132, 138] Incorporating plasmonic particles generally increased film absorption, although none of the plasmonically enhanced devices achieved record efficiencies in their respective classes, nor approached the theoretical photocurrent limits based on the photovoltaic material band gaps. Addressing the question of whether the full parameter space has yet to be explored in these systems or if plasmonic enhancement schemes are fundamentally limited in practical devices remains an important research challenge.

3.2.4 Practical Limits of Plasmonic Enhancement

There are several practical obstacles to using plasmonic structures as photocurrent enhancers, which need to be taken into account for plasmonic solar cell design. The biggest barrier is the presence of parasitic absorption in the nanoparticles.[93, 146, 147, 148, 149] Parasitic absorption refers to the loss of photocarriers excited in the metal particles themselves that decay via non-radiative channels to produce heat. This process competes with useful absorption in the photovoltaic material. The relative amount of parasitic absorption vs. useful near- and far-field scattering in the metal can be manipulated to some extent by controlling the size, morphology, material, and placement of the metallic nanoparticles.

Another practical limitation is that embedded plasmonic nanostructures can act as carrier recombination centers in the absorbing medium,[131, 150,

151] often leading to a reduction in device open-circuit voltage as well as current.[152] Including a small insulating barrier in the form of a ligand or dielectric shell around the plasmonic nanostructure can suppress this effect but can also reduce the evanescent spatial field overlap with the photovoltaic absorber, thereby limiting the potential for absorption enhancement.

Other practical issues that arise in plasmonic solar cell design include chemical and physical compatibility of the solvents associated with the plasmonic and photovoltaic materials, and materials costs of the precious metals employed as nanoparticles (primarily gold and silver). Finally, there is the issue of resulting spectral trade-offs. Plasmonic structures have the ability to enhance a spectral regime where there is incomplete absorption in the photovoltaic material. However, in regimes where absorption is substantially complete, introducing plasmonic structures has the potential to degrade the system. Therefore, it is important to be tactical both in understanding the associated spectra[153, 154] and in choosing the type, size, shape and placement within the device of the plasmonic nanostructures.[155, 156, 157]

3.2.5 Absorption Enhancement Model

Taking into account the practical enhancement limitations described above, it is clear that questions remain about the potential for using plasmonic nanoparticles as enhancers in real photovoltaic systems. Specifically, given a set of photovoltaic and plasmonic nanomaterials of interest, it would be useful to be able to quantitatively evaluate the potential photocurrent enhancement using an intuitive model that takes into account the experimental degrees of freedom

present in the system. These parameters include the metal nanoparticle material, size and shape; the thickness and identity of the photovoltaic active layer; and the relative concentration or number density of the embedded plasmonic particles. Adjusting and optimizing these factors experimentally is time- and materials-intensive, given the large parameter space.

We have developed an analytical model that can be used to evaluate the potential absorption enhancement in embedded plasmonic nanoparticle systems over a large parameter space. The results can be translated into potential photocurrent (J_{SC}) enhancement with the assumption of perfect carrier collection. The model determines the effective absorption coefficient and thickness of a photovoltaic film embedded with plasmonic nanoparticles based on the physical and optical properties of the constituent materials. These calculated effective parameters are in turn, translated to an effective absorption, taking inspiration from effective medium approaches for estimating the optical properties of mixed media.

Effective Medium Approximations (EMAs), such as the Bruggeman Model [158] and the Maxwell-Garnett Theory (MGT)[159], treat a heterogeneous medium as one that is homogeneous by effectively averaging the properties of the individual constituent materials. In the MGT, the model medium is composed of spherical particles embedded in a host material. This theory assumes that the composite material is electrodynamically isotropic and possesses a linear response to incident light. Other assumptions include that the mixture parameters are static (non-parametric), the nanoparticle inclusions are separated by distances that surpass their individual sizes, and the sizes

of the inclusions are small in comparison to the wavelength of light in the integrated medium. The Bruggeman model is an extension of the MGT that facilitates the inclusion of polydisperse particles.

Our proposed model is an intuitive extension and approximation of an effective medium theory for a specific system: plasmonically enhanced thin-film photovoltaics. The model makes similar assumptions as the MGT, including the isotropic nature of the materials and the monodispersity of the nanoparticle inclusions, but accounts for the plasmonic response by using simulated nanoparticle scattering and absorption cross-sections.

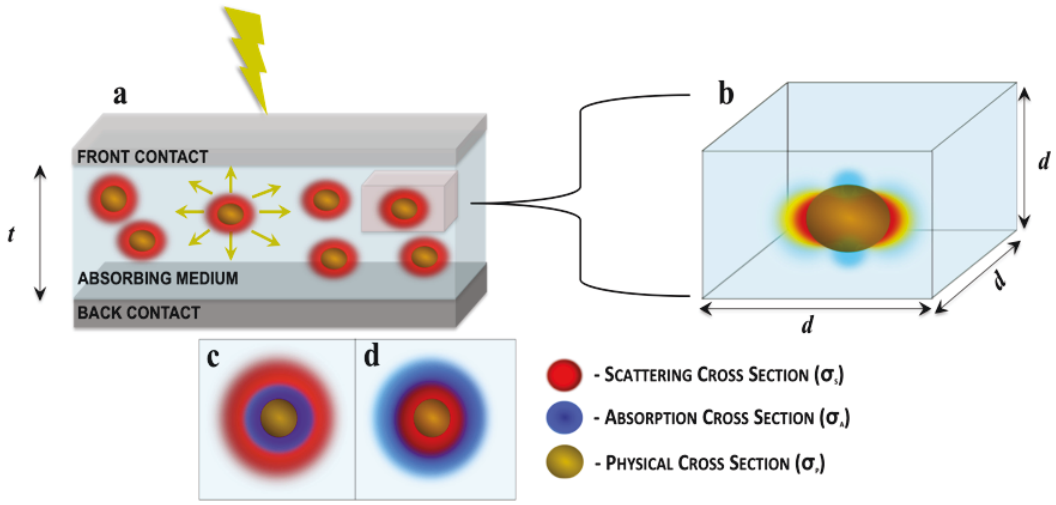

Figure 3.5: (a) Photovoltaic absorbing medium sandwiched between top and bottom contacts with randomly distributed embedded plasmonic nanoparticles. (b) Unit cube with side length d based on the average particle spacing used to evaluate the effect of a single plasmonic nanoparticle on the film. (c) Cross-section of the unit cell illustrating the case where the nanoparticle scattering cross-section exceeds the absorption cross-section. (d) Cross-section of the unit cell illustrating the case where the nanoparticle absorption cross-section exceeds the scattering cross-section.[28]

The model takes as inputs the absorption coefficient, α [m^{-1}], of the photovoltaic material; the photovoltaic film thickness, t [m], along the illumination direction; the physical cross-section, σ_p [m^2]; the scattering cross-section, σ_s [m^2]; and the absorption cross-section, σ_a [m^2] of the embedded plasmonic nanoparticles. The physical cross-section is usually defined as the 2D projection of the physical volume occupied by the nanoparticle. The absorption cross-section quantifies the rate at which energy is removed through absorption from an incident field, and the scattering cross-section quantifies the net power reflected from the nanoparticle. The scattering and absorption cross-sections can be calculated using Mie Theory[160, 161] or numerically via finite-difference time-domain (FDTD) simulations[162, 163] or finite element methods[164, 165] with the absorbing medium used as the background. Scattering and absorption efficiencies, Q_s and Q_a, are defined as the ratios of the scattering and absorption cross-sections, respectively, to the physical cross-section of the plasmonic nanoparticles ($Q_s = \sigma_s / \sigma_p$; $Q_a = \sigma_a / \sigma_p$). The absorption cross-section, scattering cross-section, absorption efficiency, scattering efficiency and absorption coefficient are all wavelength-dependent in general.

Our model assumes that the nanoparticles are randomly and uniformly distributed within the photovoltaic film with an average number density. We use the concept of a unit cell to represent the concentration (number density), ρ [m^3], of the nanoparticles within the absorbing medium. The unit cell is a cube with one nanoparticle at the center, such that the side length, d [m], is

related to the concentration as:

$$\rho = \frac{1}{d^3} \tag{3.2}$$

In addition, we define a unitless variable C to represent the relative separation between the nanoparticles:

$$C = \frac{d}{D} \tag{3.3}$$

where D is the diameter [m] (or length for non-spherical particles) of the nanoparticles. Neglecting reflection at the photovoltaic absorber surface, we use the Beer-Lambert Law[166] to calculate the absorption, A_1, in the unmodified photovoltaic film and the absorption, A_2, in the film with the embedded plasmonic particles:

$$A_1 = 1 - e^{-\alpha t} \tag{3.4}$$

$$A_2 = 1 - e^{-\alpha_{plasmonic} t_{plasmonic}} \tag{3.5}$$

$$\alpha_{plasmonic} = \alpha[1 + \frac{\sigma_p}{d^2}(Q_s - Q_a)] \tag{3.6}$$

$$t_{plasmonic} = t\sqrt{1 - \frac{\sigma_p}{d^2}} \tag{3.7}$$

Equations 3.6 and 3.7 relate the new effective absorption coefficient ($\alpha_{plasmonic}$)

and the new effective film thickness ($t_{plasmonic}$), respectively, to the materials system parameters. In Equation 3.6, $\alpha_{plasmonic}$ represents the effect that a single plasmonic nanoparticle has on the surrounding medium. The MGT uses a cubic lattice of nanoparticles in a medium to approximate the effective dielectric constant by accounting for the volume fraction taken up by the inclusions as well as the relative permittivities of the medium and inclusions. In a similar fashion, we use the plasmonic properties of a single nanoparticle and the optical properties of the medium to approximate the effective absorption coefficient. $\alpha_{plasmonic}$ can be larger or smaller than the absorption coefficient of the bare medium, depending on the relative values of the scattering, absorption and physical cross-sections of the plasmonic nanoparticle inclusions, as well as the number density of the nanoparticles, represented by their average 2D spacing, d^2. The scattering cross-section effectively adds to the absorptivity of the medium while the absorption cross-section effectively subtracts from the absorptivity of the medium. Also, the physical loss of absorbing medium caused by replacing a fraction of the material with nanoparticles is accounted for in Equation 3.7, which subtracts the projection of the physical area occupied by the nanoparticles from the cross-section of the unit cell.

This model accounts for the parasitic absorption that takes place within the metal nanoparticles, which is a source of photocarrier loss, by subtracting a term proportional to Q_a in the expression for $\alpha_{plasmonic}$. It requires input from numerical electrodynamic simulations in the form of single particle absorption and scattering cross-sections. The total-field scattered-field (TFSF) source

method[167] in the FDTD simulations yields an effective scattering cross-section that can account for both the near- and far-field scattering associated with the nanoparticle. Thus both conventional far-field scattering and "local field" effects are incorporated in the model.

Using Equations 3.4-3.7, we can define a quantitative figure of merit, M, which is a measure of the absorption enhancement in the photovoltaic system due to adding the embedded plasmonic nanostructures:

$$M = \frac{A_2}{A_1} - 1 \tag{3.8}$$

By integrating M over all wavelengths, the net absorption enhancement ($M_{total} > 0$) or loss ($M_{total} < 0$) factor can be calculated. Assuming perfect carrier collection (100% internal quantum efficiency, IQE), we can use this model to calculate the expected photocurrent enhancement in a photovoltaic device by integrating the product of the enhanced (A_2) or control absorptions (A_1), solar photon flux, and the elementary electric charge over all wavelengths.

This model requires only the calculation of the single-particle plasmonic optical properties as a prerequisite for estimating the properties of the bulk mixed media systems over a large range of parameters. This method is computationally fast compared to full numerical modeling of entire film structures with randomly embedded nanoparticles. In the following section, we will use the above model to make realistic predictions for achievable photocurrents in plasmonically enhanced photovoltaic devices and compare the results to previous experimental studies.

3.2.6 Model Evaluation

3.2.6.1 Comparison to Experimental Studies

Previous demonstrations of embedded plasmonic nanoparticle enhancements in organic, hybrid organic-inorganic perovskite and colloidal quantum dot solar cells provide test systems for evaluating our model. We will examine one specific example from each of these three systems to analyze in detail: (1) Silver nanoclusters embedded in a poly [N-9"-hepta-decanyl-2,7-carbazole-alt-5,5-(4',7'-di-2-thienyl-2',1',3'-benzothiadiazole) (PCDTBT): [6,6]-phenyl C-71-butyric acid methyl ester ($PC_{70}BM$) mixture,[104] (2) Au/Ag alloy popcorn shaped nanoparticles embedded in mesoporous TiO_2 and infiltrated with methylammonium lead iodide ($CH_3NH_3PbI_3$) perovkite,[135] and (3) SiO_2-Au core-shell nanospheres embedded in a PbS CQD thin film.[117] Absorption coefficients for the three photovoltaic materials were extracted from reported values in the literature.[117, 168, 169]

We employed FDTD simulations to calculate Q_s and Q_a for single plasmonic nanoparticles in the three examples using the total-field/scattered-field source method.[167, 170, 171, 172, 173] We used the average value of the real part of the refractive index of the three materials over a wavelength range of 300-800 nm for the PCDTBT: $PC_{70}BM$ mixture and $CH_3NH_3PbI_3$ perovskite material and 300-1200 nm for the PbS CQDs as the background in the simulations. The silver nanoclusters were represented by closely-packed 40 nm diameter nanospheres with spacing extrapolated from Figure 3.7 of Reference [77] and total diameter of 600 nm. The popcorn-shaped Au/Ag nanoparticles were modeled as nanospheres with diameters equal to the reported size of the

alloyed particles (150 nm) and refractive indices given by the molar average of the refractive indices of Au and Ag based on the reported weight ratio.[135] The average real part of the refractive index of a PbS CQD film with the first exciton peak at 959 nm was used as the background for the 120 nm SiO_2 core/15 nm Au shell particles.[117]

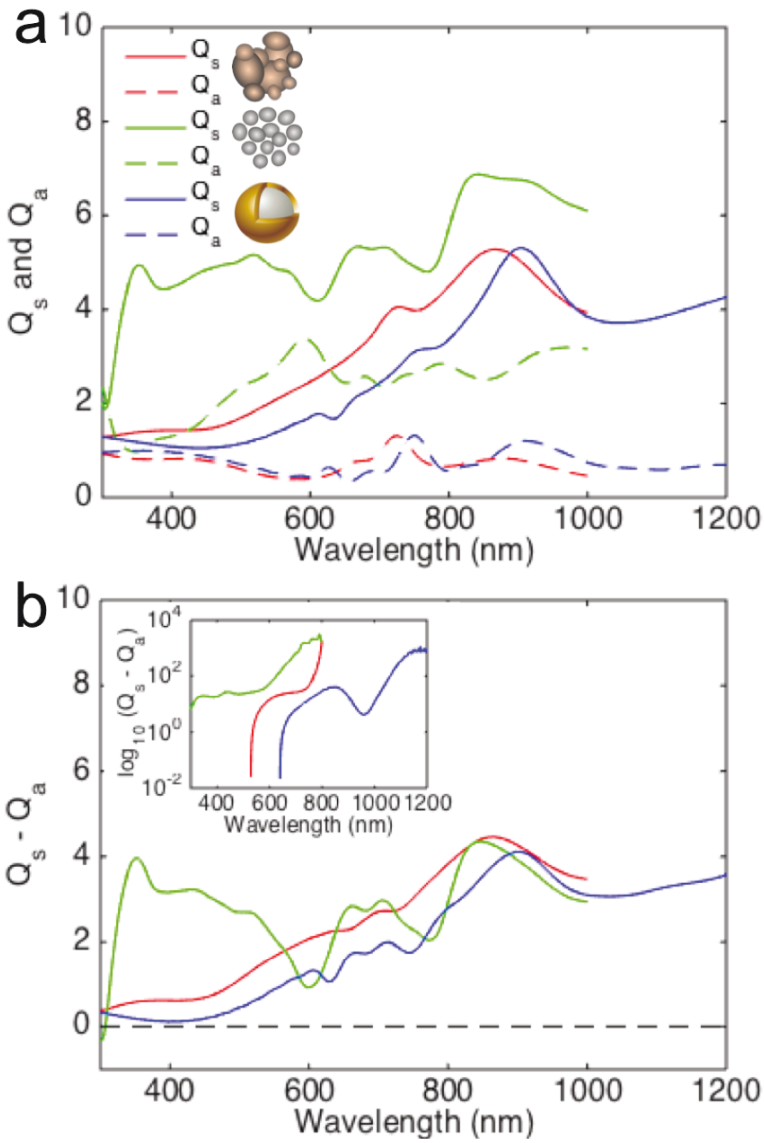

Figure 3.6: (a) Scattering efficiency (Q_s) and absorption efficiency (Q_a) vs. wavelength for the three different plasmonic nanoparticle types calculated using single-particle FDTD simulations. Solid lines: scattering efficiency. Dashed lines: absorption efficiency. Red: 150 nm Au/Ag alloy popcorn nanoparticles embedded in a perovskite-infiltrated-TiO_2 background. Green: 40 nm silver nanoclusters embedded in a PCDTBT:PC_{70}BM mixture. Blue: nanoshells with 120 nm SiO_2 core and 15 nm Au shell thickness embedded in PbS CQD film background. (b) Relative scattering efficiency (Q_s - Q_a) vs. wavelength for the systems plotted in (a). Inset: relative scattering efficiency (Q_s - Q_a) required to achieve 90% absorption as a function of wavelength the three systems at a relative nanoparticle separation C = 3.[28]

Figure 3.6 shows that the relative scattering efficiency (Q_s-Q_a) for all three types of plasmonic nanoparticles is positive over most of the relevant wavelength ranges (the absorption of the organic and perovskite materials cuts off near 800 nm). Therefore, these three types of plasmonic nanoparticles are all predicted to be enhancers in their respective absorbing media. The inset in Figure 3.6b shows the relative scattering efficiencies required to achieve 90% absorption in the three systems at relative nanoparticle separations of C = 3. The fact that Q_s and Q_a are small compared to C in each study indicates that using single-particle simulations as the basis for calculating the optical properties of the system is a reasonable approximation. This validity condition can be written as:

$$Max(\sqrt{Q_s},\sqrt{Q_a}) < C \tag{3.9}$$

Equation 3.9 requires that there is no spatial overlap of the optical influences of adjacent nanoparticles. The number density of the embedded plasmonic particles is an important experimental free parameter. There is an inherent trade-off in an embedded nanoparticle system: increasing the nanoparticle concentration can yield more scattering enhancement of the absorption in the photovoltaic material; however, the nanoparticles occupy physical volume that subtracts from the ability of the photovoltaic material to absorb light. Our model can be used to calculate the optimum nanoparticle density for each of the three test systems given the photovoltaic film thicknesses used in each case (80 nm for the PCDTBT:PC_{70}BM film; 200 nm as an

approximation of the average optical thickness of the perovskite-infiltrated-TiO_2 film; and 400 nm for the PbS CQD film).

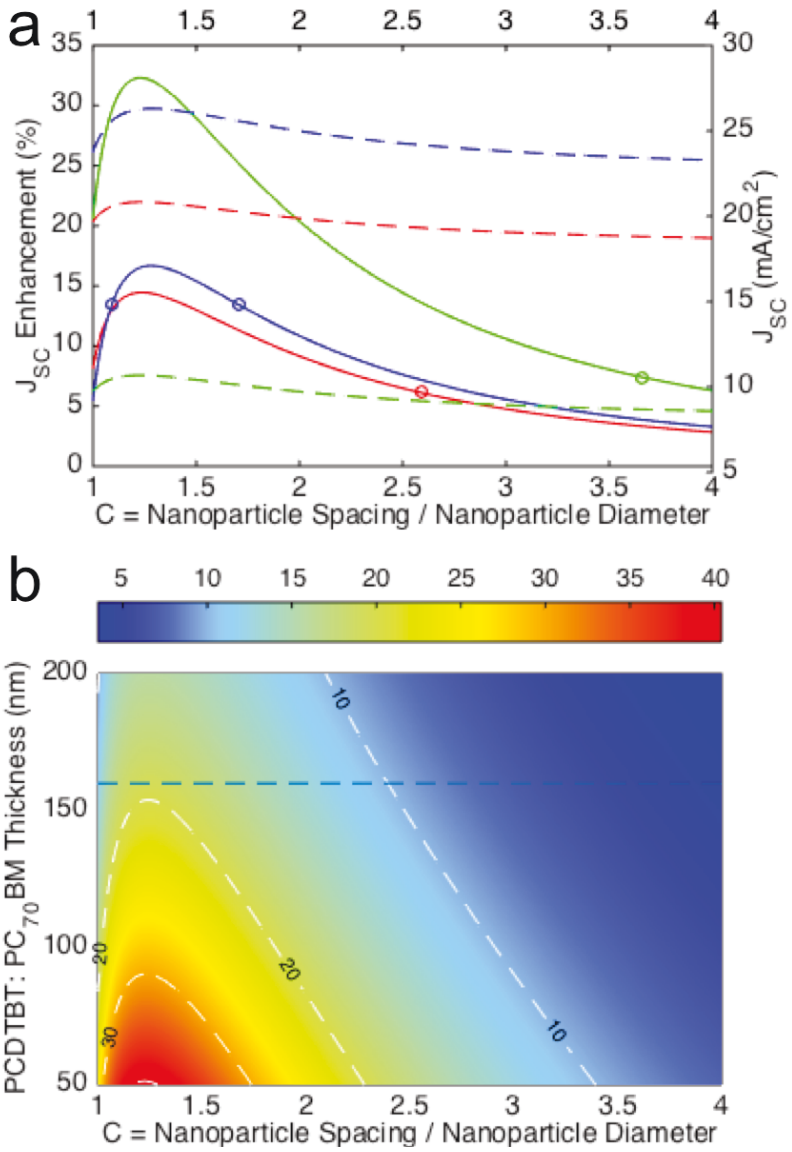

Figure 3.7: (a) Solid lines: predicted J_{SC} enhancement (%) vs. relative nanoparticle separation. The circles are experimental J_{SC} enhancement for the best-performing cells in each study. Dashed lines: predicted J_{SC} values (mA/cm^2) vs. relative nanoparticle separation. Red: 150 nm Au/Ag alloy popcorn embedded in perovskite-infiltrated-TiO2. Green: 40 nm silver nanoclusters embedded in PCDTBT:PC_{70}BM. Blue: 120 nm SiO_2 core/15 nm Au shell nanospheres in PbS CQD film. (b) Percent J_{SC} enhancement (color scale) as a function of film thickness and nanoparticle separation. The white dashed lines are contours at 10%, 20%, 30% and 40% J_{SC} enhancement to guide the eye. The blue line indicates a thickness of 160 nm, twice the reported thickness in Reference [77].[28]

Figure 3.5a is a plot of the predicted photocurrent and photocurrent enhancement as a function of relative nanoparticle separation. There is an optimum separation, or number density, of embedded plasmonic nanoparticles in each case, and the predicted J_{SC} enhancement has a long tail extending to the limit of large nanoparticle separation. The circles correspond to the J_{SC} enhancement for the best-performing cells in each study and estimated experimental values of C for the three systems were approximately 2-5, which lie in the large separation/low density range.[104, 117, 135] Generally, due to the difficulty in achieving precise control of the synthetic and deposition processes, there are multiple sources of error in the estimations of nanoparticle size and density; however, all experimentally observed enhancements fell within the range predicted by our model.

The largest relative photocurrent enhancements are predicted for the system composed of Ag nanoclusters embedded in PCDTBT:$PC_{70}BM$. This is primarily due to the small thickness (80 nm) of the absorbing film; intuitively, larger relative enhancements should be possible for thinner active layers in which initial absorption is less complete. We examined the effect of the thickness of the PCDTBT:$PC_{70}BM$ layer by varying it simultaneously with the effective nanoparticle separation to determine the potential J_{SC} enhancement as shown in Figure 3.5b. The maximum J_{SC} enhancement requires a thickness-independent high density of embedded plasmonic nanoparticles. The blue dashed line indicates a thickness of 160 nm, which is double the reported thickness in Reference [77]. If the organic layer thickness could be doubled, the predicted J_{SC} enhancement in the organic system is very close to that

predicted in the other two systems. This reinforces the idea that plasmonic enhancements are potentially more useful in extremely thin films, even independent of photovoltaic material type, and that OPV cells in particular may have more to gain from embedded plasmonic enhancement schemes.

3.2.6.2 Effect of Nanoparticle Shape

Since our model uses calculated plasmonic absorption and scattering cross-sections as inputs, it can incorporate non-spherical nanoparticles, many of which have been used in embedded photovoltaic enhancement schemes.[103, 133] Shape plays an important role in plasmonic nanoparticle properties.[155, 174, 175, 176, 177, 178, 179, 180, 181] Sharp edges can drastically increase local field intensity while simultaneously introducing strong parasitic absorption.[175, 176, 178, 179, 181] We applied our model to systems composed of octahedral and truncated octahedral Au nanoparticles (70 nm in length) embedded in PCDTBT:$PC_{70}BM$ [103], and compared them to a system with similarly-sized Au nanospheres as the plasmonic material in the same matrix. The simulation results are shown in Figure 3.8.

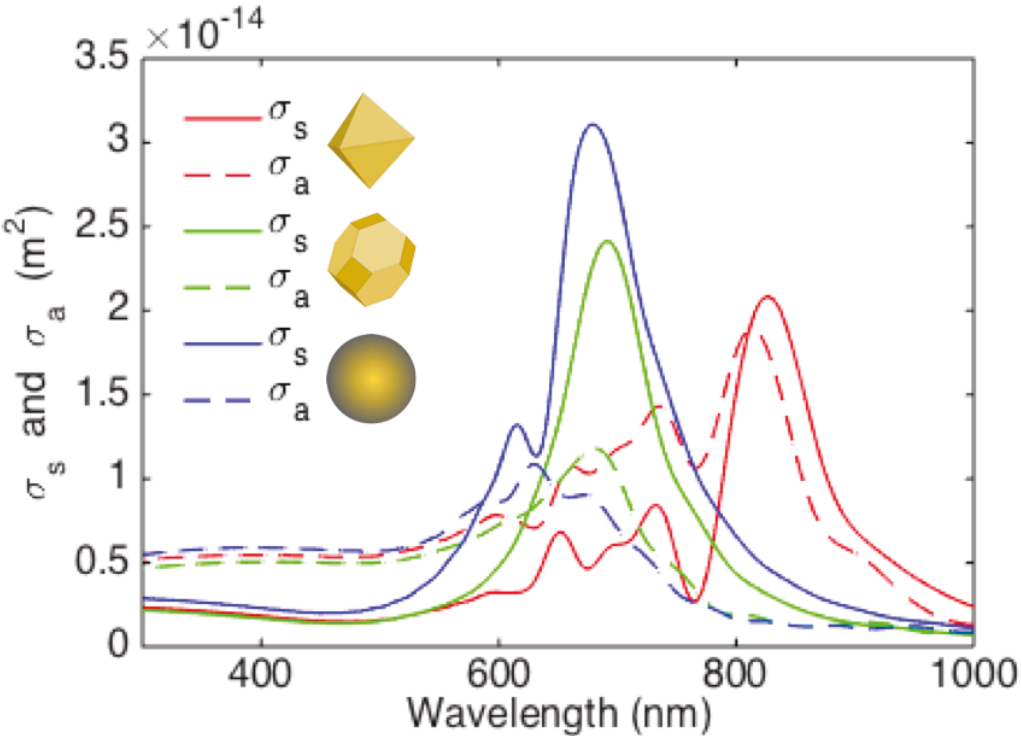

Figure 3.8: Scattering (solid lines) and absorption (dashed lines) cross-section vs. wavelength for different shaped plasmonic nanoparticles of similar size embedded in a PCDTBT:$PC_{70}BM$ background. Red: 70 nm octahedral Au nanoparticles. Green: 70 nm truncated octahedral Au nanoparticles. Blue: 70 nm Au nanospheres.[28]

The octahedral particles contain sharp points, while the truncated octahedra are much closer to spherical in shape. FDTD simulations indicate that gold nanospheres and truncated octahedra of similar size have similar optical properties. The truncated octahedra exhibit a slight red shift and a decrease of the scattering cross-section peak amplitude compared to the nanospheres. The regular octahedral nanoparticles exhibit smaller scattering amplitudes and an increase in absorption with a large red shift compared to the other particles. The absorption cross-section exceeds the scattering cross-section in the 300-800 nm spectral range, indicating that this particle type will not

enhance absorption in a PCDTBT:$PC_{70}BM$ film.

Both the truncated octahedra and the nanospheres have scattering cross-sections larger than their absorption cross-sections near 700 nm in wavelength, indicating that both nanoparticle types have the potential to enhance photovoltaic absorption in this spectral range. However, at wavelengths shorter than 600 nm, the absorption cross-sections are generally larger than the scattering cross-sections, meaning that parasitic absorption will exceed any useful scattering enhancement in this range. This test case illustrates the need to engineer nanoparticle shape for a specific application, and, generally, that shapes with sharp corners often introduce more parasitic absorption than useful scattering enhancements.

3.2.6.3 Effect of Nanoparticle Size and Material

The size-dependence of the scattering and absorption properties of plasmonic nanoparticles is another useful tuning knob for optoelectronic applications.[179, 182, 183, 184] We studied the size-dependent behavior of systems composed of Au and Ag nanospheres embedded in PCDTBT:$PC_{70}BM$. The results are shown in Figure 3.9. We used a fixed nanoparticle separation of C = 2 and a photovoltaic layer thickness of t = 80 nm for these calculations.

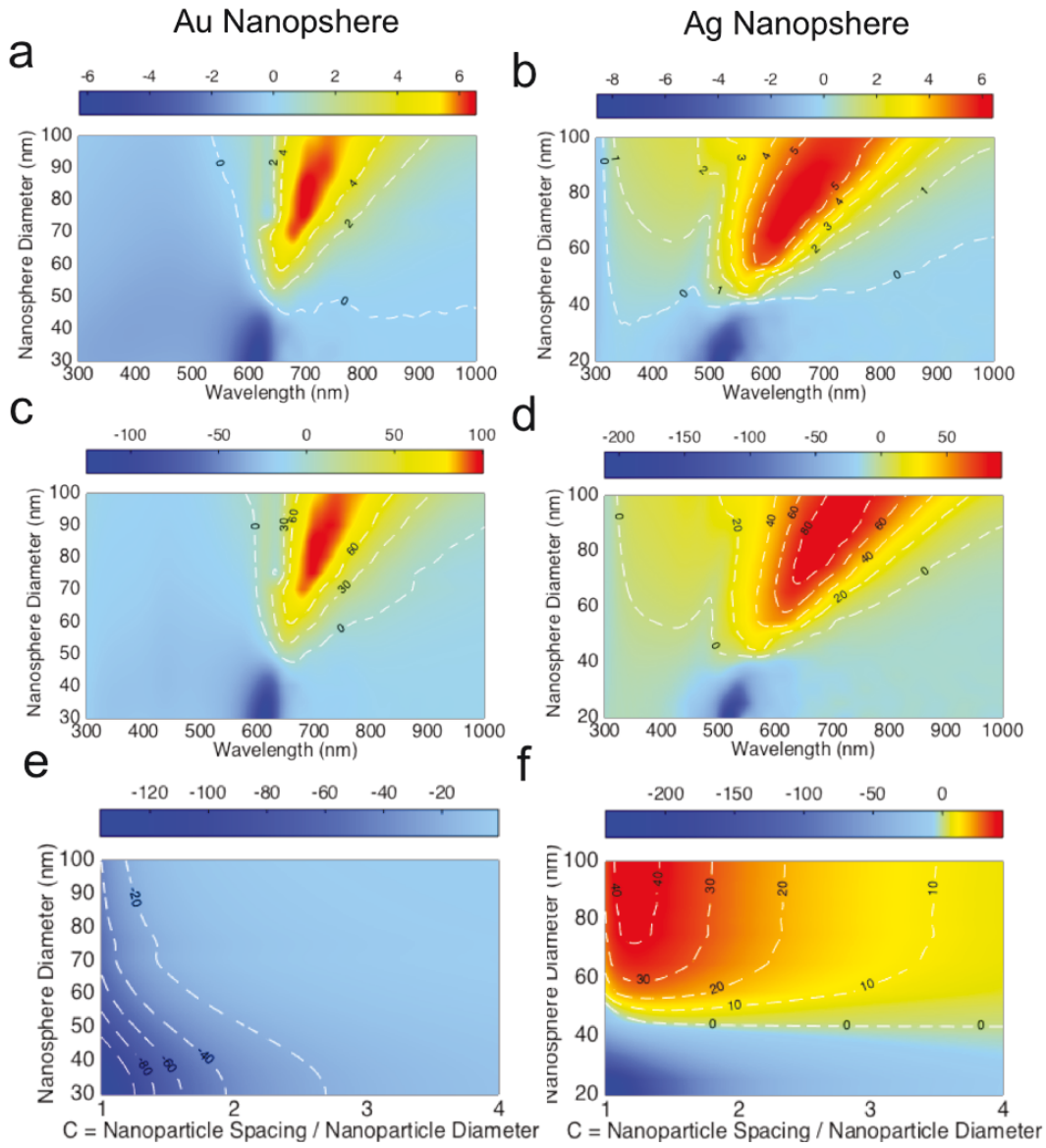

Figure 3.9: (a), (b) Relative scattering efficiency (Q_s - Q_a) vs. wavelength and particle size for Au (a) and Ag (b) nanospheres embedded in an organic film. The dashed contour lines represent Q_s - Q_a as labeled. (c), (d) Percent absorption enhancement or loss vs. wavelength and particle size for Au (c) and Ag (d) nanospheres embedded in an organic film. The dashed contour lines represent relative percentage changes as labeled. (e), (f) Percent J_{SC} loss or enhancement vs. relative particle separation and particle size for Au (e) and Ag (f) nanospheres embedded in an organic film. The dashed contour lines represent relative percentage changes as labeled.[28]

The relative scattering efficiency and the absorption enhancement red-shift as a function of nanoparticle size, as can be seen in Figure 3.9. The Au system exhibits significant parasitic absorption in the shorter wavelength regime. Figure 3.9c demonstrates that embedding these types of particles in the OPV film is predicted to result in no net J_SC enhancement. This is because parasitic absorption is predicted to dominate within the AM1.5G peak power range and relevant absorption window for PCDTBT:PC_{70}BM of 300-800 nm.

One potential method for avoiding nanoparticle parasitic absorption in the strongly absorbing spectral ranges of the photovoltaic material is to embed nanoparticles at selective locations along the illumination direction of a device. Au nanoparticles such as those modeled in Figure 5 could be embedded at the back of a PCDTBT:PC_{70}BM layer (farther from the illumination plane) so that shorter wavelength photons can be substantially absorbed before reaching the nanoparticle locations within the film. Only photons with wavelengths in the more weakly-absorbing spectral region of PCDTBT:PC_{70}BM and the more strongly-scattering spectral region of the nanoparticles (600-800 nm) would have a high probability of interacting with the plasmonic elements, thereby enhancing total absorption in the device.

The system composed of Ag nanospheres embedded in PCDTBT:PC_{70}BM behaves both qualitatively and quantitatively differently from the Au nanosphere system. As can be seen in Figure 5d, Ag nanospheres with diameters larger than 35 nm can be strong enhancers in PCDTBT:PC_{70}BM at wavelengths near 650 nm. The spectral range of enhancement displays a red shift with increasing nanoparticle size. The main spectral peak corresponds to the dipole

LSPR mode of the Ag nanospheres, and the overall enhancement is a result of competition between the scattering and parasitic absorption. The calculated electric field profile of the LSPR mode at 680 nm and scattering and absorption cross-sections vs. wavelength for an 80 nm diameter Ag nanosphere embedded in a PCDTBT:$PC_{70}BM$ film can be seen in Figure 3.10.

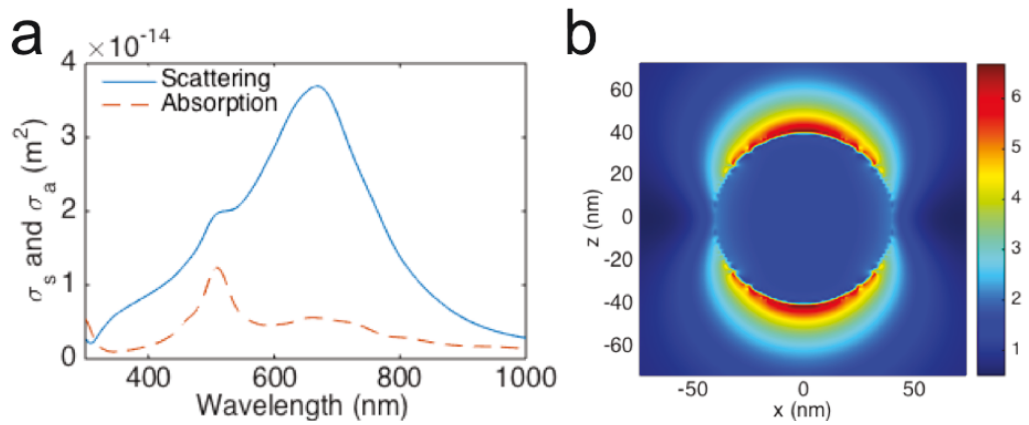

Figure 3.10: (a) Scattering and absorption cross-section vs. wavelength for an 80 nm diameter Ag nanosphere embedded in a PCDTBT:$PC_{70}BM$ background. (b) Calculated normalized electric field intensity (λ = 680 nm) for a single Ag nanosphere at the plane normal to the incident illumination.[28]

Figure 3.9e shows the wavelength-dependent absorption enhancement for different sized Ag nanospheres. Due to the high absorptivity of PCDTBT:$PC_{70}BM$ below 500 nm, most of the light in this range is absorbed in 80 nm of material without the integration of plasmonic nanoparticles. Since the absorptivity of PCDTBT:$PC_{70}BM$ between 600 nm and 800 nm is low, exploiting nanoparticles with strong scattering in this spectral range results in an absorption enhancement, with the peak enhancement exhibiting a red-shift as a function of nanoparticle size.

Using the AM1.5G spectrum as our input, we calculated the predicted J_{SC}

enhancement as a function of Ag nanosphere size and number density. The results are shown in Figure 3.9f; significant J_{SC} enhancements can be achieved for Ag nanospheres with diameters larger than 45 nm. Larger Ag nanospheres and higher number densities result in larger predicted J_{SC} enhancements. For all sizes of embedded Ag nanospheres, the predicted J_{SC} enhancement has a long and relatively flat tail in the large nanoparticle separation limit and becomes very sensitive to separation changes in the high number density limit.

3.2.6.4 Model Validity

The above model estimates the effective absorption in an absorbing photovoltaic layer using the Beer-Lambert law, which describes bulk absorption in a homogeneous medium. However, in a typical multi-layer solution-processed thin-film solar cell, the layer thicknesses are on the scale of the wavelengths of interest, and, as a result, interference effects can play an influential role in real device absorption. These interference effects could be included in our model by embedding the expression for absorption within a thin film interference calculation framework such as the Transfer Matrix Method (TMM) for a multi-layered structures.[185] Such methods take as inputs the thicknesses and the wavelength-dependent complex indices of refraction of the different optical material layers. Our model predicts the new effective absorption coefficient of the modified absorbing medium in a system containing embedded plasmonic nanoparticles. This absorption coefficient is directly related to the imaginary part of the refractive index function; however, estimating an effective real part is more complicated due to the surface plasmon condition that the real part of

the dielectric function change signs across an interface.

In order to test the effect of thin film interference on the sample device absorption results described above, we input the modified imaginary part of the refractive index from our model into a TMM solver[186] and varied the real part by using small perturbations around the original values for a given set of CQD device layer thicknesses.[117] The main effect on total device absorption was due to the addition of a back reflective contact and was less sensitive to variations in the thickness of the front illuminated side transparent contact layers. Due to interference effects, the predicted photocurrents calculated using the TMM were slightly higher (by less than 10%) than the predictions using the Beer-Lambert-based model above, but the overarching trends associated with relative nanoparticle concentration were preserved. A $\pm$10% perturbation of the real part of the refractive index of the active layer resulted in a $\pm$8% shift in the original predicted photocurrents.

Although calculations that take thin film interference effects into account must be used to make accurate predictions of the photocurrent in a real device structure, our enhancement model can be used to evaluate the total absorption enhancement potential associated with an embedded plasmonic nanoparticle strategy as a function of particle type, size, and concentration. Specific device designs can then be fine-tuned by using thin film interference and other light trapping effects.

As previously mentioned, the model described above is a good approximation for real systems when Equation 3.9 is satisfied, i.e. the average nanoparticle concentration is relatively small. This is borne out by the close match of

the predicted J_{SC} enhancements with the reported experimental results. When Equation 3.9 is not satisfied, the model can still be used, but coupling effects between the nanoparticles must be taken into account via simulation of the optical properties of a larger system.[183, 184] In addition, at higher nanoparticle concentrations, our model becomes less accurate due to strong nanoparticle scattering effects and the break down of the plane-wave condition for the Beer-Lambert law.

The model predicts absorption enhancement and corresponding JSC enhancement by assuming perfect carrier collection (IQE) in the photovoltaic systems. However, it is possible to include carrier loss induced by the nanoparticle inclusions into the model, and models that account for both optical and electrical effects have been developed for other proposed systems. [187, 188, 189, 190] This could be achieved, for example, by calculating the effective nanoparticle electronic trap capture cross-section and subtracting the trapping efficiency from the Q terms in the calculation of αplasmonic (Equation 3.6). Other carrier loss mechanisms in real devices could be included through experimental IQE measurements.

3.2.7 Perspective and Future Directions for Solution Processed Solar Cells

General strategies for designing an effective plasmonic enhancement scheme for a specific photovoltaic system can be based on the following two steps:

1. Choose an appropriate material, shape and size in which the scattering cross-section is larger than the absorption cross-section within the

photovoltaic material of interest for the intended spectral enhancement range.

2. An effective medium approach, such as the model described here, can be used to select the optimum embedded nanoparticle density for maximum plasmonic absorption enhancement of the photovoltaic medium.

As has been demonstrated through successful experiments, this strategy can lead to absorption and consequent photocurrent enhancements in real devices. Careful analysis of the model described above, however, indicates that the absolute magnitude of the potential enhancements may be limited. Specifically, in CQD and perovskite solar cells, the model predicts that the maximum achievable plasmonic photocurrent enhancements can probably only improve upon the current best performing devices by about 15%, corresponding to 1 - 4 mA/cm^2 of additional photocurrent. Given these results and the history of steady transport improvements in these materials, we recommend that the fields concentrate instead on improving fundamental materials properties such as decreasing electronic trap state densities and increasing charge carrier diffusion lengths through improved passivation and growth methods. Plasmonic enhancements are of most interest for applications where external considerations limit the thickness of the active material to less than that already utilized in the best performing devices.

In contrast, the outlook for plasmonic enhancements in organic photovoltaics may be much brighter. Active layer thicknesses are smaller in the best performing OPV classes due to limitations on exciton dissociation and diffusion. Therefore, plasmonic photocurrent enhancements of up to 40% are

predicted by our model, as can be seen in Figure 3.9. Specifically, the field should concentrate on using large (up to 100 nm) silver particles for OPV films due to the LSPR spectral overlap and reduced parasitic absorption at shorter wavelengths, and nanoparticle shapes with pointed vertices should be avoided due to the parasitic absorption induced by the sharp edges. From a practical standpoint, care must be taken in using large nanoparticles for thin film enhancement to avoid the formation of detrimental shunt paths in devices. Critically, further absorption and photocurrent enhancements are predicted to be possible at larger embedded nanoparticle densities than have previously been explored. However, the density must be fine-tuned in order to achieve optimum performance due to the sharply peaked nature of the predicted enhancement curves, as seen in Figure 3.7. In recent years, there have been improvements in achieving thicker absorbing layers for OPVs,[191] and the maturation of these improvements would render plasmonic enhancements less applicable.

In addition to emphasizing work on plasmonically enhanced OPV, we propose two relatively unexplored plasmonic enhancement paths. The first is aggressively pursuing new plasmonic materials strategies. Gold and silver have been the most commonly used plasmonic materials in photovoltaics due to their low-loss behavior in the visible wavelength range resulting from the relatively small values of the imaginary parts of the dielectric function. Alternatives such as aluminum, copper and indium tin oxide also have the potential for low loss in specific spectral ranges. New strategies that take advantage of these materials could include spatially integrating ITO nanoparticles at the

base of a tandem device to enhance infrared absorption, or using aluminum nanoparticles for ultraviolet absorption enhancement in thin absorbing active layers. Additionally, alloying different metals to achieve "averaging" of the spectral properties for broadband enhancement is an attractive potential strategy.

The second path of interest is pursuing electronic coupling to make true hybrid plasmonic-excitonic materials. Instead of considering only the optical properties of plasmonic enhancers in forming an effective medium, full treatment of the electronic effects of these materials could make plasmonic materials of interest for multiple classes of solution processed solar cells. The goal would be to use coherent electronic coupling of plasmonic particles to semiconducting media in order to engineer the excitonic structure. This material hybridization strategy could be used to extend the spectral sensitivity of organic materials to infrared wavelengths, e.g. or could be used modify the band structure CQD films to increase absorption near the exciton wavelengths while aiding in transport.

In conclusion, as the field of plasmonically-enhanced solar cells matures, focusing on strategies with the highest potential for enabling real performance advances is of increasing interest. We believe this entails adjusting nanoparticle concentration as the most crucial tuning knob in embedded plasmonically-enhanced photovoltaic devices, working on the specific silver-based strategy outlined for OPV and pursuing the advanced methods described above that go beyond the traditional gold/silver optical enhancement paradigm.

3.3 Tuning color and transparency in CQD solar cells by optimized multi-layer interference

This section is adapted (in part) from Ref. [192]. Reprinted with permission from Optics Express 24, no. 4, A101-A112, "Color-tuned and transparent colloidal quantum dot solar cells via optimized multilayer interference," by Arinze, Ebuka S., Botong Qiu, Nathan Palmquist, Yan Cheng, Yida Lin, Gabrielle Nyirjesy, Gary Qian, and Susanna M. Thon, copyright © 2017.

3.3.1 Introduction

Multi-colored solar cells, solar cells with controlled, tunable spectral reflection and absorption profiles, are of significant interest due to their potential to be coated on exterior surfaces of urban infrastructures, such as building facades, rooftops and automotive skins, to serve both aesthetic and functional purposes.[193, 194] In tandem cell applications, there is also a need to systematically control absorption and, in turn, achieve the required current-matching in cells that possess different spectral absorption profiles. Additionally, semi-transparent solar cells are attractive for integration into portable electronics [195] and for window coatings to help with building and vehicular heat management.[196, 197] Solar cells based on solution-processed materials are especially promising for these large-area applications because of their thin-film and lightweight nature, ease and flexibility of fabrication, associated low costs, and high efficiency potential.

Past examples of colored solution-processed solar cell technologies include using combinations of dyes,[198] photonic filters,[199] physically- or

chemically-modified absorbing/transport layers,[200, 201, 202, 203, 204, 205] integrated liquid/photonic crystals,[206, 207] embedded optical microcavities and dielectric mirrors,[202, 208, 209] and modified top/bottom electrodes [210, 211, 212] in dye-sensitized, organic, and perovskite solar cells. Although multi-colored and semitransparent solar cells based on perovskites and organic materials have been demonstrated, their narrow spectral absorbing ranges, which lie mainly within the visible portion of the spectrum, represent a significant drawback for achieving high photocurrents. As a result, light management strategies to produce cell colors or achieve transparency come with an unavoidable loss of device efficiency.

Colloidal quantum dots (CQDs), semiconducting nanocrystals stabilized in solution, are a promising candidate material for achieving multicolored and semitransparent solar cells [213, 214] due to their band gap tunability, which is enabled by the quantum size effect.[215] Specifically, lead sulfide and lead selenide (PbS, bulk band gap energy of 0.41 eV,[216] and PbSe, bulk band gap energy of 0.27 eV [217]) CQDs have band gaps that can be tuned from the near-infrared to the visible portion of the spectrum. As a result, visible absorption losses induced by the design of multicolored or semitransparent cells can potentially be compensated for by enhanced absorption in the infrared region.

Standard CQD film-based devices [213, 214, 218](Figure 3.11) employ different electronic layers that have thicknesses on the order of the optical wavelengths of interest. The layer thicknesses and design are typically optimized for their electrical properties, but optical thin-film interference plays a

large role in these devices as well, as demonstrated by efforts to utilize interference effects to achieve semitransparency and absorption enhancement via electrode modification [219, 220] and microcavity structuring.[220, 221] Traditionally, transparency in CQD-based devices is induced by employing thin absorbing layers.[222, 223] In this study, we design, optimize and fabricate multicolored and transparent CQD solar cells based on thin-film interference engineering concepts to customize both optical and electrical device properties.[224] Using physical and mathematical modeling techniques, including Transfer Matrix Method (TMM) calculations [186] and multiobjective optimization algorithms,[225, 226] we have developed an optimization method for the custom-design of multicolored and transparent CQD solar cells that could be generalized to other materials systems. The optimization sequence is depicted in Figure 3.11c. The method maximizes reflection and transmission at specific wavelengths, creating a desired cell color, while simultaneously requiring high photocarrier generation rates in a solar cell device.

Our multi-layer thin film calculations were based on a depleted heterojunction architecture [61] design for CQD photovoltaics, but could be generalized to include any optoelectronic layer structure. Figure 3.11 shows an example of this architecture, which consists of an optically thick glass substrate, followed by indium tin oxide (ITO, the bottom contact), TiO_2 (the n-type layer), PbS CQD film (the p-type layer), MoO_3 (buffer layer), and Ag (the top electrode).

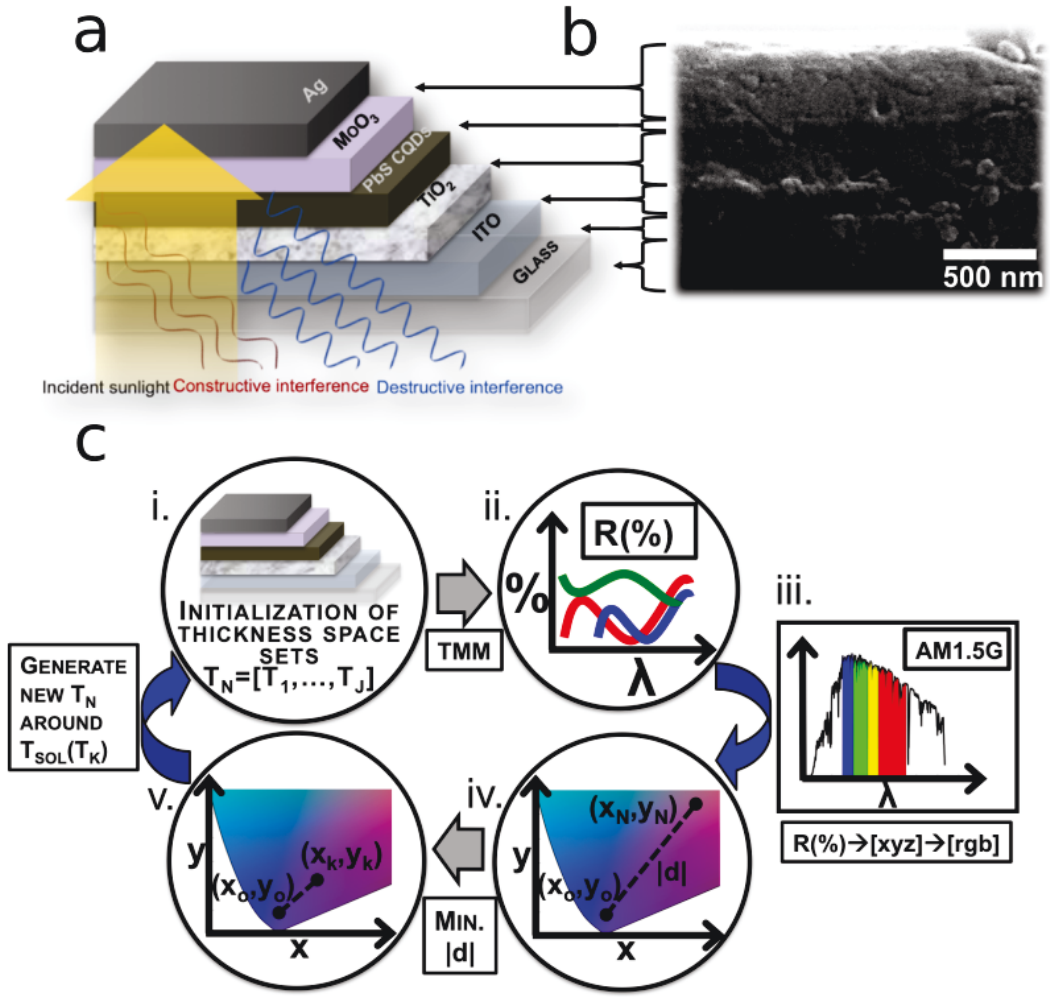

Figure 3.11: (a) Schematic of a CQD-based solar cell illustrating the spectrally-dependent optical interference patterns that can result from tuning the thicknesses of the different cell layers. As incident broadband sunlight passes through the device, constructive or destructive interference occurs at certain wavelengths, resulting in wavelength-dependent reflectivity and transmission, giving the cell its apparent color or semitransparency. (b) Cross-sectional scanning electron microscope (SEM) image of the structure shown in (a) with the layers labeled. (c) Graphic representation of the optimization technique to produce cells with defined color characteristics. Space set of thickness combinations is (i) initialized and each combination is transformed to (ii) a reflection spectrum via TMM. These spectra in combination with incident (iii) AM1.5G and color matching functions are translated to rgb colors on (iv) chromaticity plots where the distance to the intended color is (v) minimized. This optimization cycle repeats until a global minimum is realized.[192]

3.3.2 Optimization of the photocurrent-color tradeoff

We use the TMM, which takes the thicknesses and complex refractive indices of all layers as inputs, and calculates normalized electrical field profiles within the multi-layer structure. In our simulations, the materials models are composed of complex refractive index data from the literature and experimental ellipsometry measurements, and we consider a broadband illumination source with a wavelength range of 300 - 1800 nm. In the case of opaque reflective colored solar cells, Ag is used as the back contact, and ITO is used as the back contact for the semitransparent solar cells. We calculate the reflection spectrum of the device, and predict the expected "color" by combining this spectrum with an appropriate set of color matching functions (1931 CIE [227]) and an illuminating spectrum (AM1.5G). The predicted color can be represented on a 2-dimensional chromaticity plot, as shown in Figure 3.133a Cell "transparency" is calculated by averaging transmittance data over the visible wavelength range (420 nm - 680 nm) output by the TMM calculations.

In order to optimize the color response of our cells, we use particle swarm optimization (PSO),a population-based algorithm,[225] tailored for our specific application, as illustrated in Figure 3.11c. A "swarm size" of solution thickness sets is initialized and fed into the TMM to generate associated reflection spectra, which are then transformed to apparent color. These [rgb] co-ordinates are then optimized for a specific reflected color/wavelength response by minimizing the distance between the target point and solution point on the chromaticity plot, yielding a global solution via multiple iterations. The presence of two different populations (pbest and pcurrent) and

particle movements in PSO allows for both greater degrees of exploration and faster convergence when compared to other optimization methods, such as genetic algorithms. Due to the multilayer architecture of our device and highly multidimensional search space involved, a semi-periodic reflectivity landscape with multiple local minimal emerges. Therefore, employing a PSO with a relatively large "swarm size" provides an efficient route to identifying the global minimum for our highly multidimensional optimization problem.

Despite the infrared responsivity of the PbS CQDs, there still exists a trade-off between the available photocurrent and visible transparency in device designs. This trade-off can be partially mitigated by taking the advantage of multi-layer interference effects to reduce visible field overlap with the CQD layer while maintaining absorption in the infrared. In order to achieve high photocurrent with minimum loss of visible transparency, we used PSO to perform single-objective optimizations on the layer thicknesses, keeping the PbS layer thickness constant. The three optimization targets chosen to explore the entire parameter space involved with the trade-off were high transparency, high photocurrent, and low transparency. The available photocurrent and average transparency of each solution to the three optimization problems are shown in Figure 3.12.

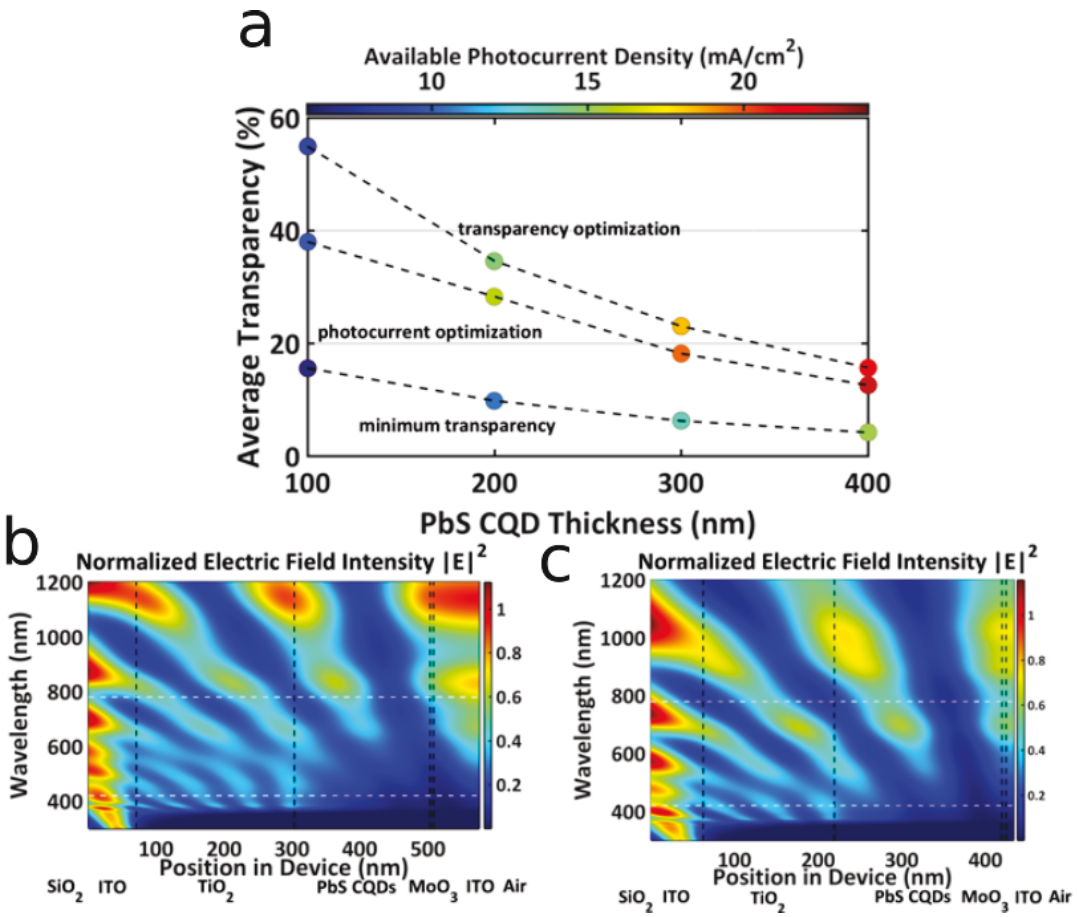

Figure 3.12: (a) Calculated average transparency (%) and corresponding available photocurrent density (mA/cm^2, color bar) versus PbS CQD film thickness (nm). Top curve: optimized for maximum average visible transparency. Middle curve: optimized for maximum available photocurrent density. Bottom curve: calculated for minimum average transparency. Calculated electric field intensity as a function of wavelength and position in the transparent device structure (ITO back contact) with a PbS CQD layer thickness of 200 nm for: (b) transparency-optimized case; (c) photocurrent-optimized case.[192]

In Figure 3.12a, the average transparency is plotted as a function of CQD layer thickness, and the available photocurrent is represented by the color. The top curve is the set of solutions at each given PbS CQD film thickness optimized for the highest transparency. The middle curve is optimized for the

highest photocurrent at each film thickness. Higher photocurrent comes with the expected trade-off of lower transparency. The bottom curve is calculated for the lowest transparency, and it has the lowest available photocurrent of the three sets of solutions. The difference between the bottom curve and the middle curve represents both the photocurrent and degree of transparency that can be gained for a given active layer thickness by doing a rational layer thickness optimization via our method.

The high photocurrent for the middle curve is achieved by maximizing the electric field intensity within the absorbing layer. The high transparency of the top curve is achieved by employing multi-layer interference to minimize the electric field intensity at visible wavelengths within the absorbing layer. The difference between these two cases is visualized in Figures 3.12b and c. In the optimized photocurrent case (Figure 3.12c), there is an intensity peak at a wavelength near 700 nm within the CQD film, allowing more longer wavelength light to be absorbed within this layer. In the optimized transparency case (Figure 3.12b, there is no electric field intensity peak at the edge of the visible spectral range; instead, there is a peak closer to 800 nm at the NIR edge, allowing visible light to be transmitted and maintaining a relatively high photocurrent through NIR photon absorption.

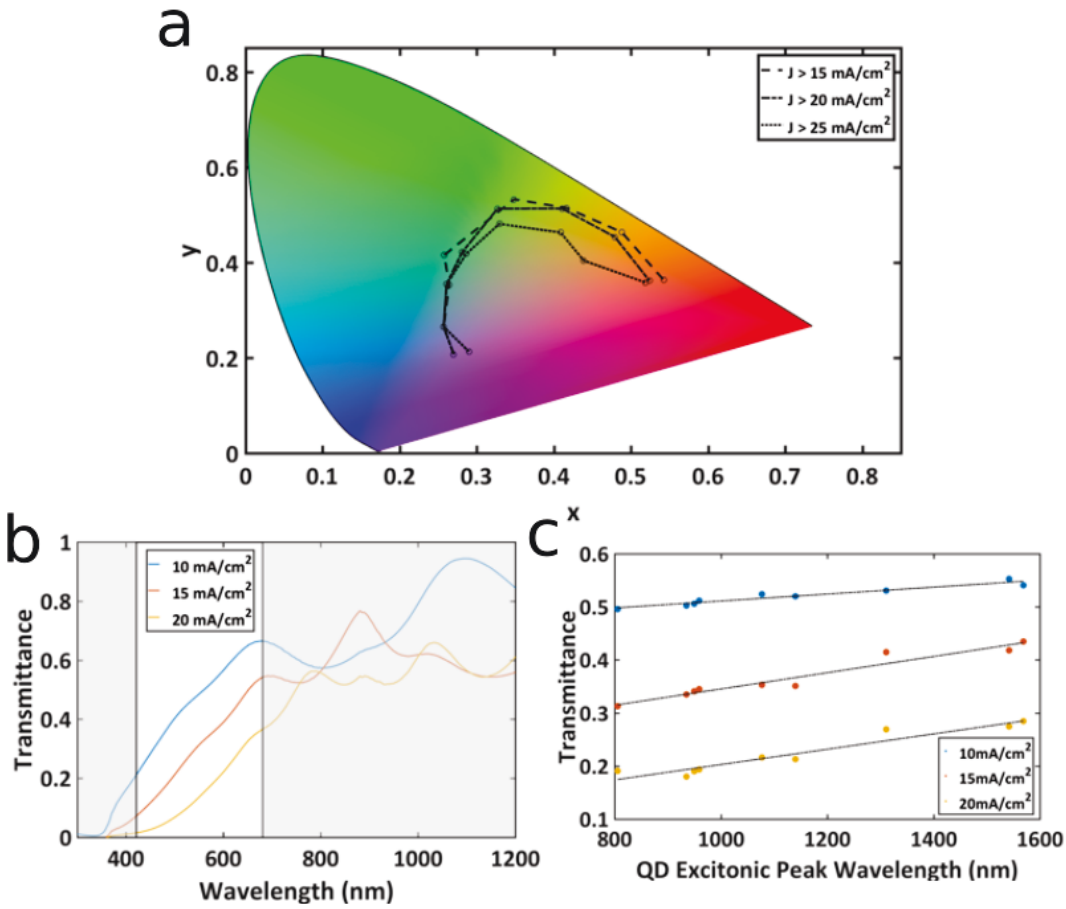

Figure 3.13: (a) Chromaticity plot showing achievable colors given minimum photocurrent requirements (J > 15 mA/cm^2, J > 20 mA/cm^2, and J > 25 mA/cm^2). Calculated Transmittance plots showing: (b) trade-off between transparency and photocurrent (for CQDs with 950 nm exciton peak wavelength), and (c) achievable transparency given minimum photocurrent requirements for different CQD excitonic peak wavelengths.[192]

The tradeoffs between attainable color or transparency and minimum device photocurrent are illustrated in Figure 3.13a. From this plot, it is apparent that photocurrent requirements more strongly affect "redder" colors, whereas the range of "bluer" colors that can be achieved shows little correlation with achievable photocurrent. Figure 3.13b shows transmittance plots for devices

optimized for their transparency based on photocurrent restrictions. As expected, lower required device photocurrents result in higher potential visual transparency levels. Figure 3.13c shows the dependence of the photocurrent/transparency tradeoff on the CQD excitonic peak wavelength.

3.3.3 Effects of non-ideal layers on color saturation

In evaluating the prospects for real devices, it is important to take into account non-ideal effects, such as interface roughness, non-uniformity of the layer physical properties, and the presence of scattering centers formed by impurities and contaminants. We can incorporate these effects into our model by using another parameter, the effective "optical roughness" of each layer. We create a sufficiently large number of samples with random thicknesses by adding the standard deviation of a Gaussian distribution based on the measured or assumed roughness to the mean thickness for each layer. We then calculate the reflectance curve of each sample in the distribution and statistically average the reflectance from all samples to derive the effective reflectance curves.

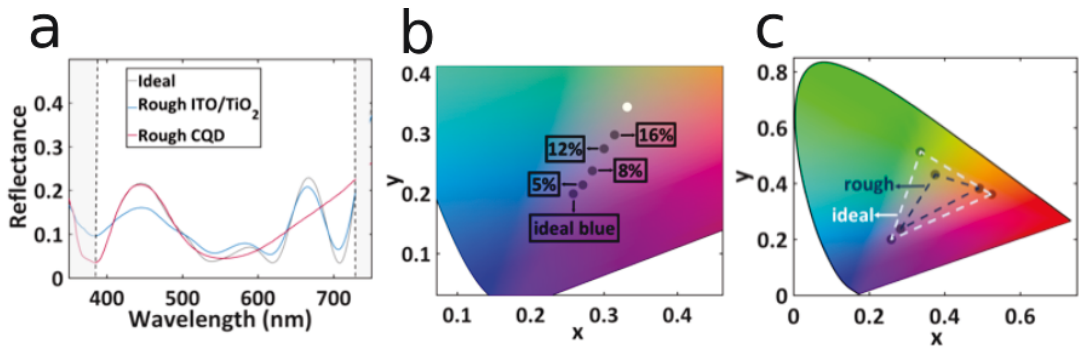

Figure 3.14: (a) Simulated reflectance curves for a specific color objective with and without an effective optical roughness of 10% for the ITO/TiO_2 layers and 10% for the CQD layer. (b) Effects of different levels of roughness on the chromaticity of a "blue" device. Percentages refer to the ratio of the standard deviation to the ideal thickness of the ITO/TiO_2 layer. The white point of the standard illuminant is also plotted as a reference point. (c) Roughness (10%) has the effect of moving the vertices on the largest achievable triangle of color profiles closer to the white point.[192]

Due to the nanostructured nature of the material itself as well as the deposition technique, the CQD layer typically has a geometrical roughness of 3-10 nm.[142] The geometrical roughness of the underlying electrodes and oxide layers deposited by evaporation, which can be determined from surface profilometry, is usually smaller than that of the CQD films. However, the effective optical roughness can be significantly greater than the geometrical roughness. One possible origin of optical inhomogeneity in the ITO and TiO_2 layers is the compositional and structural non-uniformity introduced during the deposition and processing steps, which can be seen as a spatial variation in the refractive index profile of the electrode films.

Figure 3.14 shows the effects of non-ideal interference on the reflectance curves as well as the effective colors of the devices. As can be seen in Figure 3.14a, the reflectance from devices with rough CQD layers is smoothed in the red spectral region, while the shorter-wavelength region is mostly unaffected

by the roughness. For rough TiO_2 and ITO layers, the deviations from the ideal case are greater in the blue region. The changes in the reflectance curves reduce the wavelength selectivity, and make the apparent color less saturated. The chromaticity plot in Figure 3.14b demonstrates this effect for a device that is designed to be blue in color. As the effective optical roughness of the ITO/TiO_2 layer increases, the chromaticity point moves towards the white point, decreasing the saturation, and shifting the color towards brown-grey. In Figure 3.14c, after accounting for the optical roughness, all 3 points corresponding to the maximum achievable saturation of red, blue and green, are closer to the white point. This approach to considering the effects of non-ideal interference is particularly useful for understanding color in real devices.

3.3.4 Application in tandem structures

Our proposed method for color-tuning CQD solar cells is of particular interest for applications in all-CQD and hybrid tandem photovoltaics, where current-matching is critical to series-connected device performance. CQDs are particularly suited to tandem applications because of their band gap tunability, infrared responsivity, and compatibility with a variety of materials systems afforded by their solution-processing. This flexibility effectively eliminates the difficulty of finding a materials combination possessing both appropriate band gaps and suitable lattice matching for optimized multijunction cells.[228] Proof-of-principle studies have demonstrated tandem structures utilizing all-CQD materials systems [229, 230, 231] and CQDs in conjunction with polymer materials.[232, 233]

In these series-connected CQD tandem structures, current matching is essential to obtain high efficiency devices. Generally, this is achieved by empirically adjusting the layer thicknesses until approximately equal photon absorption occurs in the two active layers. Here, we use our optimization algorithm to take into account the effects of interference in a multilayered stack to design optimum absorbing layer thicknesses.

For our optimization simulation, we employed a PbS CQD system comprised of 1.55 eV and 0.95 eV dots which are both within 5% of the optimum band gaps for the maximum efficiency in a two-junction tandem structure.[234] In addition, our simulated tandem structure integrated a graded recombination layer as demonstrated in a previous study.[229] Calculating absorption using only the Beer-Lambert law [166] in the active layers, not taking into account reflection, gave optimum thicknesses of 350 nm and 247 nm for the front and back cells, respectively, predicting a maximum photocurrent of 18.1 mA/cm^2. Using our optimization process, we obtained optimum thicknesses of 350 nm and 196 nm for the front and back cells, respectively, achieving an output-matched photocurrent of 18.6 mA/cm^2. We achieved a $\sim$3% increase in expected photocurrent using our optimized approach, even though it takes into account reflection and the detrimental parasitic absorptions in the electrodes and the other non-active layers in the 9 layer tandem stack, whereas the control case does not. Our optimization method, accounting for both interference and reflection, provides an efficient route for tandem layer designs in both CQD and hybrid systems.

3.3.5 Experimental results and discussion

We fabricated several proof-of-principle CQD solar cell devices based on our optimization method designs for different colors using PbS CQDs with exciton peak wavelengths near 950 nm. To minimize the fabrication uncertainty in the layer thicknesses, we used commercial ITO-coated glass substrates with ITO thicknesses of 28 nm for our "red" and "green" cell designs. For the "blue" cell, we deposited ITO on a glass substrate via e-beam evaporation, followed by an annealing process, to obtain our target optical thickness. The TiO_2 layer was also deposited using e-beam evaporation for precise thickness control, and a $TiCl_4$ solution treatment was applied afterwards.[117] The PbS CQD layer was built up using a layer-by-layer solid state ligand exchange process.[117] Two or three drops of oleic acid capped PbS CQD solution at a concentration of 50 mg/mL per layer were deposited through a 0.22 μm pore filter and spin-cast on the substrate. 0.5% mercaptopropionic acid (MPA) in methanol was used to soak the film for 3 seconds to replace the oleic acid, then the film was spin-cast dry. Lastly, the films were washed with methanol twice to remove the unbound ligands, completing the deposition of one CQD film layer. The total CQD film thickness was controlled through the acceleration, spin speed, spin time and number of layers and verified using profilometry measurements. We were able to control the thickness of the CQD layers to within $\pm$15 nm. The top contact was composed of a thin MoO_3 buffer layer and Ag, which were both deposited via e-beam evaporation.

Photographs of the colored and transparent cells are shown in Figure 3.15a.

We measured the reflectance of each solar cell using an Agilent Cary 5000 UV-Vis-NIR spectrophotometer with an integrating sphere insert, calculated the corresponding xyz color values by integrating over the AM1.5G spectrum, and plotted them in a chromaticity diagram. The reflectance spectra are plotted in Figure 3.15b, and the calculated color of the fabricated devices is shown in Figure 3.15d.

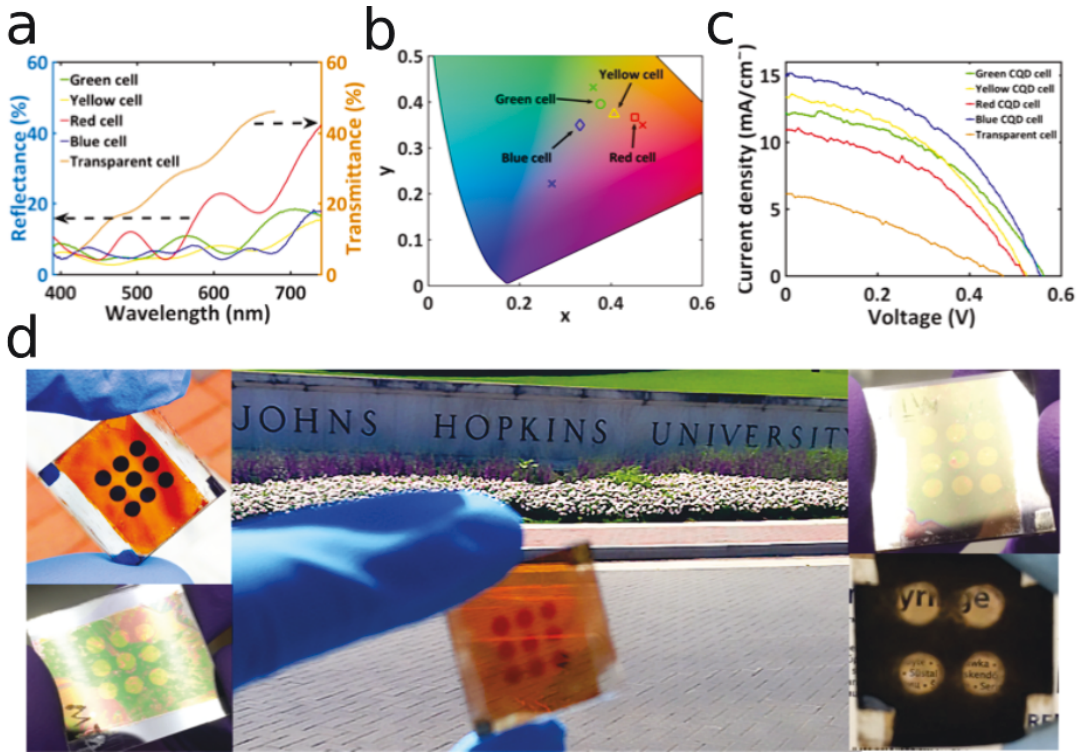

Figure 3.15: (a) Experimental reflectance and transmittance spectra for colored and semi-transparent solar cells, respectively. (b) Chromaticity plot showing the calculated coordinates for different colored devices. Crosses indicate design points while corresponding colored shapes indicate experimental points. (c) J-V characteristics taken under simulated solar illumination for colored and semi-transparent devices. (d) Photographs of blue (upper left), green (lower left), red (center), yellow (upper right), and semi-transparent (lower right) CQD solar cells.[192]

We also fabricated semi-transparent devices based on our optimization

Cell Type	V_{OC} (V)	J_{SC} (mA/cm^2)	FF	PCE(%)	Design Parameters $ITO/TiO_2/PbS/MoO_3/Ag$ (nm)
Blue	0.56±0.01	14.6±0.6	0.44±0.01	3.6±0.1	240/113/400/100/475
Green	0.55±0.02	12.1±0.7	0.42±0.02	2.8±0.1	28/150/297/12/60
Yellow	0.53±0.01	12.6±0.5	0.41±0.01	2.7±0.2	28/150/297/12/60
Red	0.50±0.03	10.3±0.8	0.41±0.03	2.1±0.3	28/166/222/22/274
Transparent	0.46±0.05	5.2±0.7	0.31±0.01	0.8±0.1	28/349/170/17/85(ITO)

Table 3.2: Average performance characteristics of colored and transparent solar cell devices showing open-circuit voltage (V_{OC}), short-circuit current (J_{SC}), fill factor (FF) and power conversion efficiency (PCE). All measurements are for at least 5 devices.[192]

method. The top contact of these devices was a composite electrode consisting of spin-coated Ag nanowires and ITO nanoparticles. Our test devices had measured visible transparencies ranging from 27.3% to 32.2%. The measured transmittance spectrum of the highest efficiency device is plotted in Figure 3.15c.

All current density-voltage measurements were carried out in a nitrogen-purged environment. Current density-voltage curves were measured using a Keithley 2400 source meter with illumination provided by a Sciencetech solar simulator with an irradiance of 1000 W/m^2. The active area of the solar cell was illuminated through a circular aperture with an area of 0.044 $cm^2 \pm 0.003$ cm^2. The power through the aperture, measured using a Thorlabs broadband power meter, was used to calibrate the power density. The measured short circuit current (J_{SC}), open circuit voltage (V_{OC}), fill factor (FF), and power conversion efficiency (PCE) for the different cells are summarized in Table 3.2.

The differences in performance between the devices are related to their

different design parameters, which are determined by the need to optimize reflection and transmission over specific wavelength ranges. Blue is a relatively difficult color to produce using this method, since the reflections are minimized due to the strong absorption of the CQD film in the blue region of the spectrum. The optimal design included a very thick CQD film layer. The lower FF of the semi-transparent device is related to the difficulty in making a strongly conducting top transparent contact without heat-processing due to the presence of the temperature-sensitive underlying CQD film.

Generally, the experimental photocurrents were smaller than those predicted by the simulations by approximately 50-60%, due to experimental deviations from the model assumptions. The simulations make the assumption of perfect carrier collection (IQE = 100%), whereas CQD solar cell IQE is typically on the order of 50-90% above the band gap.[117, 235] Additionally, experimental variations in the device layer thicknesses can contribute to lower average photocurrents. On average, the ITO, TiO_2, and PbS CQD layer thicknesses in our devices were within 15 nm, 10 nm, and 15 nm, respectively, of the design thicknesses.

3.3.6 Conclusion and outlook

We developed a method for producing arbitrary spectral profiles in layered solar cell structures using thin film interference modeling techniques combined with optimization algorithms. At selected wavelengths, our model maximizes reflection and/or transmission to create a target color and transparency level while simultaneously maximizing photocarrier generation rates. Our study

revealed that designs with minimum transparency do not necessarily correspond to the highest attainable device photocurrent, providing a pathway for high efficiency colored devices. Although effective optical roughness in the films decreases the color saturation, CQD solar cell devices with well-defined color profiles can still be produced. Our optimization method produced layer designs for tandem solar cell applications, with increases in expected photocurrent over conventional designs despite taking into account optical losses. Experimentally, we fabricated proof-of-principle blue, green, yellow, red and semi-transparent devices. The measured reflectance and transmittance spectra agreed well with the perceived color and transparency levels.

Future work will focus on broadening the application of our model to hybrid materials systems (single junction and tandem design structures based on non-CQD-based films) and explicitly including additional loss mechanisms. Additionally, the overall device performance could be improved by employing the current best CQD device architecture strategies with graded doped CQD layers involving solution-based halide passivation treatments.[236, 237] Finally, this work, coupled with the development of more efficient room-temperature-processed transparent electrode materials, should extend the range of functionalities of flexible optoelectronic devices.

3.4 Engineering photonic bands in absorbing media for spectral selectivity

This section is adapted (in part) from Ref. [238]. Reprinted with permission from Optics Express 26, no. 21, pp. 26933-26945, "Photonic band engineering

in absorbing media for spectrally selective optoelectronic films," by B. Qiu, Y. Lin, E. S. Arinze, A. Chiu, L. Li and S. M. Thon, copyright © 2018.

3.4.1 Introduction

Spectrally selectivity is critical in many optoelectronic applications, such as optical imaging [239, 240], target recognition [241, 242], chemical detection [241, 243, 244, 245] and solar energy harvesting [246, 234, 247, 248], but is difficult to achieve in traditional semiconductors which typically absorb at all energies above their band gaps. Specific examples of technologies requiring fine-tuned spectral responsivity include finite bandwidth photodetectors and materials with controlled transparency windows for multijunction and transparent photovoltaics [246, 234]. Spectral-selectivity can be employed for heat management in solar cells or other optoelectronic devices by reflecting unwanted wavelengths that would otherwise be parasitically absorbed in the contacts or other device layers. [249, 250, 251, 252] Common solutions to this problem include using external filters for photodetectors [243], which come with the cost of adding complexity to the system, and empirically controlling the thicknesses of each absorbing material in tandem solar cells to realize current matching, which often sacrifices photocurrent output [253, 229, 254]. Here, we propose a solution that achieves controlled spectral selectivity within the absorbing material itself, i.e. the photogenerative material that is responsible for energy conversion or transfer of the absorbed photon energy: using photonic crystals to engineer the photonic band structure in absorbing media to directly control the wavelength-dependent absorption, reflectivity

and transmissivity.

Photonic crystals (PCs) are materials with periodic variations in their dielectric functions, potentially creating a photonic band gap, a range of frequencies in which photons are forbidden to propagate. This compelling mechanism enables PCs to be used to manipulate light flow in many applications including optical communications [255, 256, 257], computing [258, 259, 260, 261], and optoelectronics [262, 263, 264, 265, 266]. In addition to artificial structures, many examples of PCs can be found in the natural world, enabling effects such as the structural colors of butterfly wings and beetles [267, 268, 269].

Most of these examples use PCs with photonic band gaps lying in the naturally non-absorbing range of the materials, i.e. below the electronic band gap where the material behaves like a simple dielectric, although photonic band structures can be straight-forwardly tuned in frequency by adjusting the length scale of the dielectric function periodicity (lattice constant). [270] Positioning the photonic band gap of a PC in the absorbing region of a material presents complications due to absorption being viewed as a loss mechanism for many applications. However, optoelectronic applications such as photovoltaics or photodetectors rely on semiconductor absorption and photogeneration as vital operating mechanisms, and the possibility of using photonic band engineering within the absorbing region represents a potential new spectral tuning mechanism. The concept is illustrated in Figures 3.16a and b. Previous work on engineering photonic band gaps in lossy materials includes forming PCs from metals that have shown diminished reflection peaks with increasing absorption [271]. Initial work on forming PCs within

the photoactive layers for solar cells has been proposed, focusing on utilizing the PC structures for spectrally-selective light trapping [272] and absorption enhancement [272, 273, 274] based on density of states modulation. For wavelength selective-absorption, band-pass absorbers made from dye-glass [275] have been widely implemented for decades, and in recent years, metamaterials based on periodic plasmonic structures have been demonstrated with very high absorbance within the visible range for solar-thermal applications [276]. These implementations typically focus on extending the spectral response in their respective systems by combining structures with engineered responses in different spectral ranges. However, rather than focusing on absorption alone, a comprehensive method for inducing spectral-selectivity that aims to enable wavelength-dependent absorption, reflectivity and transmittivity simultaneously, including not just absorption enhancement but also suppression through the use of controlled transparency windows, has yet to be demonstrated. Here, we describe how embedding PCs in photogenerative materials could offer a handle for controlling spectral features across multiple wavelength bands and dynamic ranges in complicated optoelectronic applications such as multi-junction solar cells.

Spectral-selectivity is particularly applicable for the design of color-tuned materials with controlled transparency windows for multijunction and transparent photovoltaics. Infrared (IR) sensitive materials, such as small-bandgap semiconductors, absorb strongly at all energies above their band gaps. Molecular materials, such as organic semiconductors, [277] typically have finite-bandwidth absorption peaks in the visible and UV, but IR-only responsive

materials are rare. To incorporate IR-sensitive materials into multijunction solar cells, they must be positioned at the back side of a standard solar cell device to permit the absorption of visible radiation by the front cell, and the thicknesses of both cells must be fine-tuned to achieve current-matching. An ideal material for incorporating multijunction functionality into current single junction photovoltaic technology would have an absorption profile that was both spectrally tunable and finite in bandwidth, thus offering flexibility for both current-matching and device design.

The concept of using the photonic band structure in a slab-type PC to control the reflection and transmission of external propagating fields is illustrated in Figure 3.16. In Figure 3.16, we present a system consisting of a 2D PC "slab" structure in which a periodic lattice of air holes is drilled in a semiconductor. The "out-of-plane" incident, reflected, and transmitted fields are highlighted and interact with the "in-plane" resonant field with properties determined by the PC structure. Here we use "in-plane" to describe physical structures or fields and states that are bound by or mostly concentrated in the slab itself, and "out-of-plane" to describe fields and waves that propagate indefinitely outside of the slab structure. The "in-plane" fields and states compose the band structure of the slab, and they can couple to the "out-of-plane" incident waves at the point of the Brillouin Zone, shown on the right side of the Figure. We sketch hypothetical reflection and transmission spectra at normal incidence alongside a hypothetical (generic) in-plane band diagram for a structure such as that shown in Figure 3.16 to illustrate the coupling between the in-plane photonic bands and the out-of-plane reflection and transmission profiles. The

transmission and reflection spectra should consist of a smoothly varying background that resembles a Fabry-Perot interference spectrum, [278] with sharp and asymmetric resonance features on top. As will be discussed in the next section, the coupling between incident waves and the photonic bands sharing a lateral wave-vector results in resonance features in the transmission and reflection spectra of the slab. This coupling gives rise to the potential for tuning the "out-of-plane" spectral selectivity by tailoring the band structure of the PC slab, to achieve desired absorption, reflection and transmission profiles.

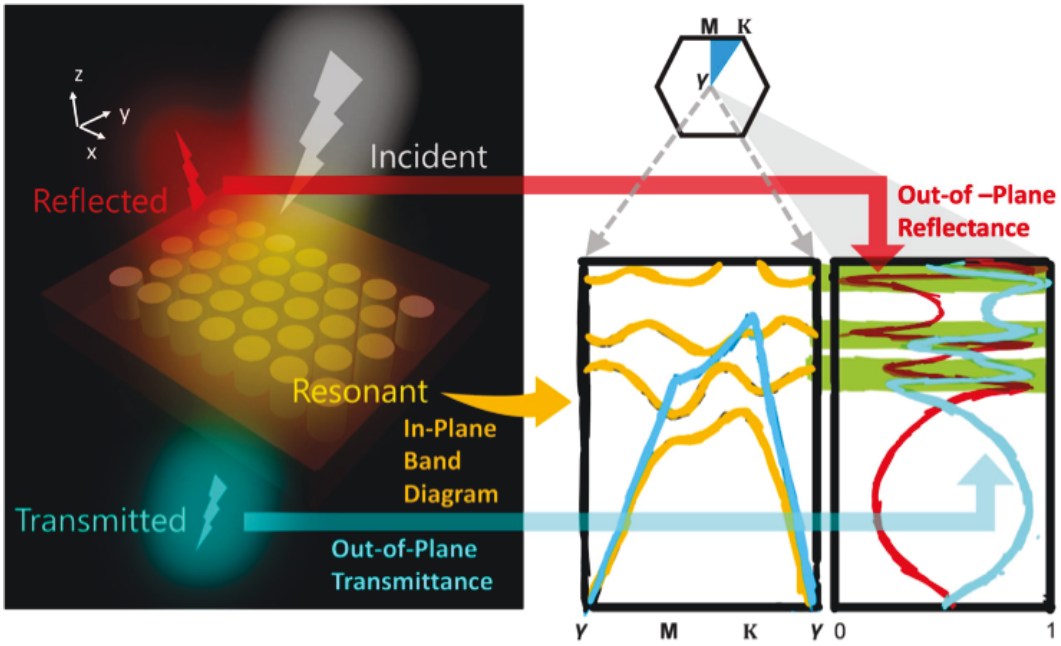

Figure 3.16: Schematic of a generic 2D slab photonic crystal illustrating the spectral tuning concept (left). The "in-plane" photonic band structure is used to generate spectrally-selective reflectivity, transmissivity and absorption for target optoelectronic applications. Broadband light (white in color) is incident on the slab, with specific frequency components strongly coupled to the resonance modes of the slab (yellow), resulting in spectrally-selective transmission (blue) and reflection (red). A hypothetical photonic band diagram for the generic slab structure (photonic bands are shown in yellow; the light line is shown in blue in the center panel) and "out-of-plane" transmittance (blue) and reflectance (red) spectra at normal incidence are sketched on the right side of the Fig. The green stripes show direct correlations (coupling) between the sharp resonance features in the transmittance and reflectance spectra and the photonic band states at the γ-point. A Brillouin Zone diagram for the hypothetical structure is shown above the photonic band diagram sketch.

In this work, we use finite-difference time-domain (FDTD) simulations and Fourier modal methods [279, 280, 281] to quantify the effect of material absorption on a slab PC with relevant photonic bands that fall above the electronic band gap of the semiconductor slab material. We then use the

insights gained from the simulations to design a PC structure in a solution-processed semiconductor, based on a PbS colloidal quantum dot (CQD) thin film, that strongly absorbs in the infrared but transmits visible light more strongly than in the non-structured semiconductor. This type of material could enable visible-blind infrared photodetectors without external filters, and it could also allow for flexibility in current-matching in a tandem solar cell.

3.4.2 Simulations

To study the effect of material absorption on photonic band structure, we based our simulations on the well-studied 2D GaAs slab PC structure, [262] which consists of a triangular lattice of air pillars in a semiconductor slab of finite thickness. In FDTD simulations, we are able to artificially adjust the strength of the absorption through control of the imaginary part of the dielectric constant (ϵ_I) as long as we keep the real part (ϵ_R) constant, which is equivalent to varying the real and imaginary parts of the refractive index (n, k). Dispersion is not explicitly considered in the test-case model since it results in difficulty in satisfying the Kramers-Kronig relations [282]. The completely non-absorbing control case uses a material that has ϵ_R set to 13, meant to approximate the average value of n for GaAs across the relevant frequency range, and ϵ_I set to zero. We then gradually increase the value of ϵ_I in the simulations, keeping ϵ_R constant, in order to systematically quantify the effect of dissipation on the photonic band structure.

We use FDTD simulations to calculate the frequencies of the modes that

can exist in the structure beyond the initial transient phase in our artificial materials to reconstruct their photonic band structures. The broadband field profile of the excitation source is chosen to ensure that all modes of interest are excited. Randomly distributed time monitors collect the time-resolved field data. Destructive interference causes rapid decay of non-resonant fields, while the excited modes of the structure resonate with varying decay rates for the bulk of the simulation time. The frequencies of these modes are extracted via fast Fourier transform (FFT).

Details of the FDTD simulation method for band structure simulations [283] are as follows: The simulation volume consists of an integer number of unit cells of the 2D periodic structure, and the volume is extended in the z-direction symmetrically above and below the slab by approximately 10 lattice constants. Bloch boundary conditions are used for the x and y (in-plane) directions and perfectly matched layers (PMLs) with symmetric or anti-symmetric boundary conditions are used in the simulations corresponding to the even (TE-like) or odd (TM-like) mode polarizations, respectively, for the z-direction. Identical broadband dipole sources with random polarizations are used to excite the modes and randomly distributed throughout the simulation volume. Conformal meshing is used near material interfaces, and Maxwell's integral Eqs are used to account for structural variations within a single mesh cell. We apodize the loaded time signals from each time monitor for each field component, with a Gaussian-shaped windowing function used to only consider the portion of the time signal following the source pulse injection and before the simulation is cut off. The resulting FFT of the apodized signal

is a spectrum with peaks at the resonant mode frequencies, corresponding to allowed photonic bands. The energy spectra of Fourier-transformed time signals for each field component of every time monitor are summed to ensure that we identify all of the resonant frequencies even if some of the randomly placed time monitors are located at the node of a mode. The simulations are repeated for each Bloch vector value, K, and frequency peaks for each K that meet the threshold tolerance are retained.

In our simulations, we chose a semiconductor slab thickness of 125 nm and tuned the lattice constant (a = 250 nm) and radius (r = 60 nm) of the air holes to produce a number of relevant photonic bands within the visible regime, or above the electronic band gap of GaAs. The model structure is shown in the inset of Figure 3.17c. The simulated band structure for the non-absorbing control case with both even and odd modes is shown in the top left panel of Figure 3.17a, followed by a series of photonic band structures with increasing k. The photonic band structure for a GaAs PC slab including full dispersion [284] in the refractive index model is shown in Figure 3.17b.

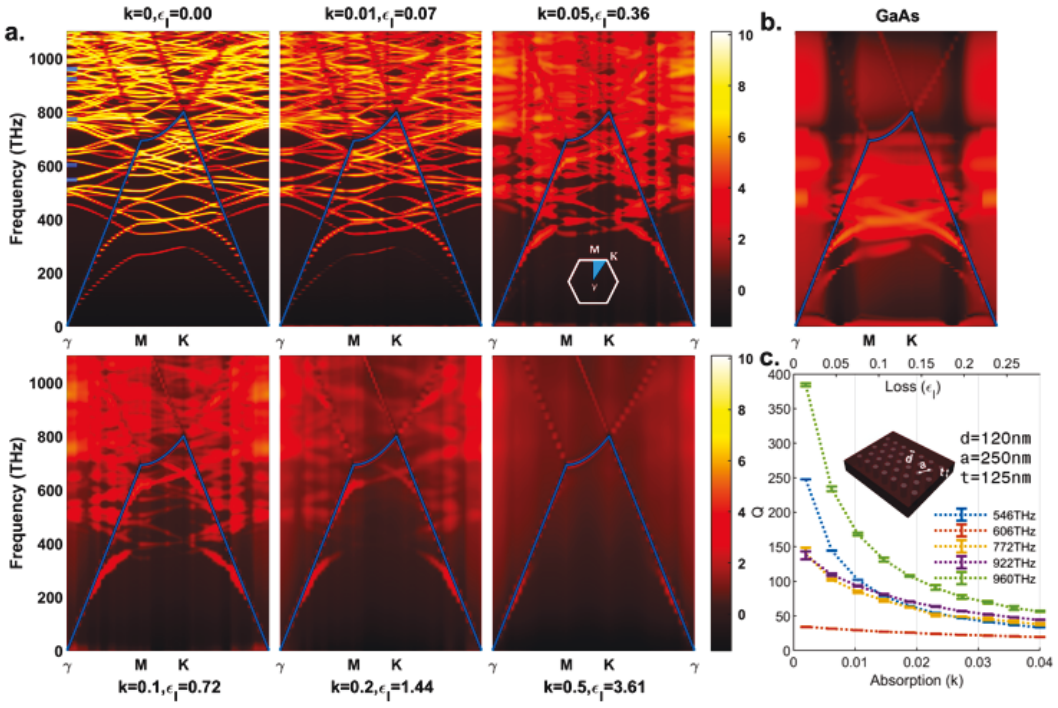

Figure 3.17: (a) FDTD-calculated photonic band diagrams for the structure shown in (c) with media loss (absorption) varying from ϵ_I=0 to ϵ_I=3.61 and constant ϵ_R= 13, with corresponding imaginary part of the refractive index also indicated. The light lines are plotted in blue. The color scale is in arbitrary logarithmic units corresponding to the field intensity. (b) FDTD-calculated photonic band diagram for the same structure for a GaAs slab medium (the dielectric constant includes dispersion in this case). (c) Quality factor for 5 selected modes, indicated by the blue markings at the point in the top left panel of (a), as a function of loss in the material. Inset: model of the simulated structure, a triangular lattice of air holes in a semiconductor slab with 120 nm diameter, 250 nm lattice constant, and 125 nm slab thickness.

As can be seen from Figure 3.17a, the frequencies of the photonic bands are almost unchanged as dissipation is added to the optical model, if ϵ_I remains small compared to ϵ_R, although the relative band strengths are reduced with increasing material absorption. As material loss increases, the widths of the bands are broadened, and the clarity of the higher order bands decreases faster than that of the lower order bands, which is expected from the shorter

absorption lengths at higher frequencies present in the model. The rough maintenance of the photonic band frequencies in the presence of weak material loss can be understood using perturbation theory applied to the PC master Eq. [262] Adding a small imaginary part to the dielectric function, ϵ, results in the addition of an imaginary part to the resonance frequency, $\omega_0 = \omega_0 - i\gamma$, which consequently adds to the linewidth of the Lorentzian resonance profile and reduces the resonance peak height.

To quantitatively study the properties of photonic bands in dissipative structures, we calculated quality factors, Q, for the individual bands in the structure shown in Figure 3.17: $Q_i = \omega_0/\Gamma_i$, where Γ_i is the energy decay rate, or the band resonance linewidth, of the ith photonic band at the γ point of the periodic structure. Modes at the point are above the light line, and because of the finite thickness of the PC slab, they are radiating modes at that point that can couple to external propagating fields. Here, we chose five modes capable of coupling to plane waves at normal incidence angles, i.e. they can be excited by incident plane waves and radiate energy to reflected and transmitted plane waves. For this reason, these bands dissipate energy from the slab and have finite Q even without the presence of material absorption. Figure 3.17c shows the quality factors for the five bands as a function of increasing ϵ_I or k in the material. All quality factors exhibit similar decays as a function of ϵ_I and can be well fitted by the function $Q_i = \frac{Q_0\Gamma_0}{\Gamma_0+\alpha_i\epsilon_I}$, where Q_0 is the quality factor of the lossless structure, and α_I is a constant that depends on the spatial distribution of the ith mode [26]. As loss in the material (ϵ_I) increases, the differences in Q between different modes decrease, corresponding to a "smearing" and

overlapping of the photonic bands until they eventually become indistinct at the limit of very high material absorption.

Understanding the interactions of external propagating fields with the in-plane photonic band structure of a slab-like PC, specifically the spectral reflection and transmission of a PC thin film, is a critical step in using them for absorbing optoelectronic applications. These interactions involve power transfer from external fields to radiating modes within the slab and vice versa. Such systems can be modeled as resonators interacting with external ports using coupled-resonator theories [285]. In PC thin films of interest for optoelectronic applications, the periodicities are always smaller than the wavelengths of interest; therefore, for plane wave sources, no diffraction orders exist. Consequently, all fields and modes that interact with an incident wave are contained in the reflected and transmitted waves with the same in-plane wave vector as the incident wave, and the in-resonance slab radiating modes. Waves impingent at normal incidence on a slab-PC therefore compose a system that can be fully and concisely modeled.

Figure 3.18 shows transmission and reflection spectra for absorbing and non-absorbing PC structures calculated via Fourier modal methods [279, 280, 281] at a fixed in-plane wave vector with polarization along one of the reciprocal lattice vectors. The smoothly-varying background curve resembles the spectrum from a simple Fabry-Perot cavity consisting of a uniform continuous media sandwiched between two mirrors, with additional sharp resonance features added on top. The resonances occur at the same frequencies as the in-plane PC radiating modes and are asymmetric with negative and positive

features due to the nature of Fano resonance behavior [285]; these features include dramatic increases in transmission on one side of the resonance, even in the case with material absorption. The transmitted and reflected fields directly couple to the incident field while simultaneously indirectly coupling to the radiating mode of the photonic crystal excited by the incident field. Such resonance phenomena are well explained by temporal-coupled wave theory [285, 286, 287]. We note that not all modes in the photonic band structure can be excited with incident plane waves, due to restrictions in symmetry and polarization [285].

In the absence of absorption, the Fano resonance features are narrow and sharp, due to the intrinsic long lifetimes of the lossless radiating modes. When absorption is added to the model, the lifetimes of the radiating modes are reduced, resulting in broader and weaker resonance features, which originate from the same effects as the reduction in Q factor seen for the modes in the band structures. The resonance frequencies for the same structure with a non-zero ϵ_I, set to 2% of ϵ_R, are almost unchanged, in accordance with the FDTD photonic band structure simulations. The FDTD-calculated photonic band structure for the ϵ_R=0 case is plotted next to the reflection and transmission spectra in Figure 3.18 to illustrate direct spectral correspondence between the out-of-plane Fano resonance features and the in-plane photonic crystal bands. The overall reflection and transmission are both slightly reduced in the case with absorption compared to the case without absorption, as would be expected for a uniform lossy slab.

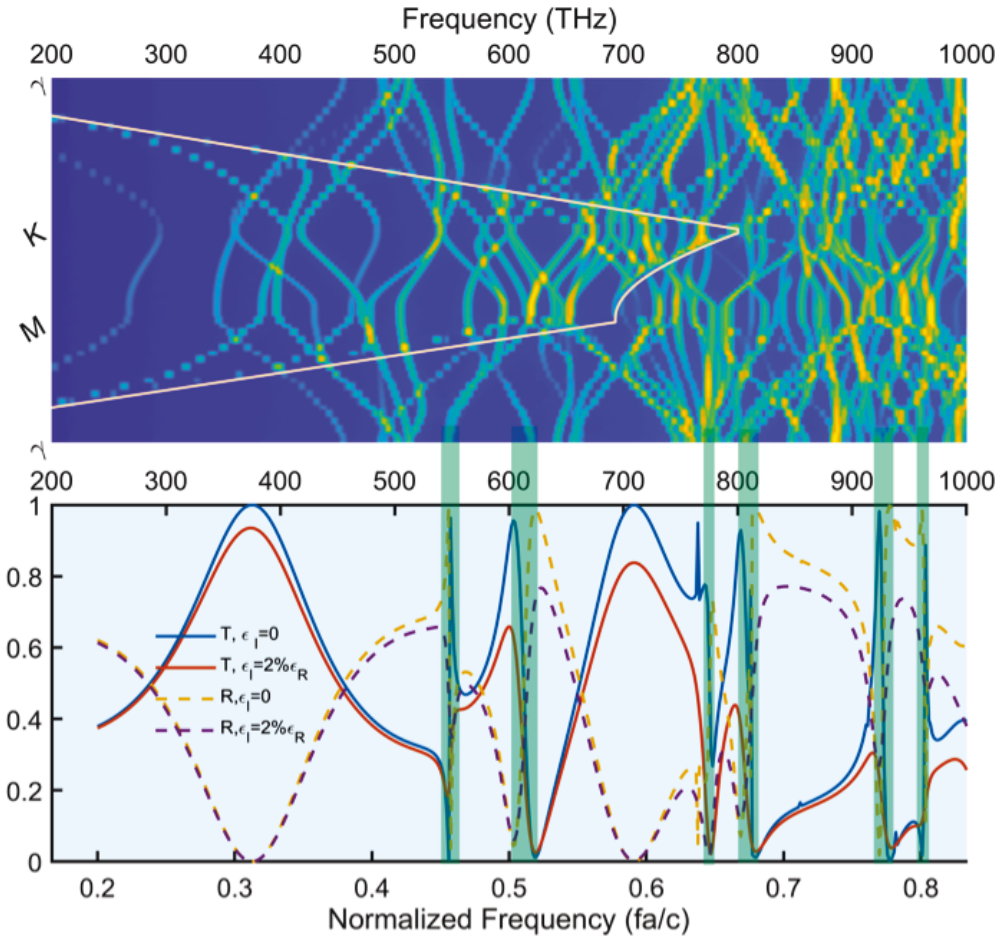

Figure 3.18: FMM-calculated transmission (solid lines) and reflection (dashed lines) spectra (bottom) for a triangular lattice slab photonic crystal with r = 0.24a, t = 0.5a and ϵ=13 (blue and yellow spectra) and ϵ=13+0.3i (red and purple spectra). The incident field is perpendicular to the slab structure. The corresponding FDTD-calculated band structure for the ϵ=13 case is shown in the top panel (light line plotted in white). The resonance regions are highlighted and associated with the modes at the γ point in the band structure.

Although the resonance features are less apparent in the transmission and reflection spectra of the absorptive structure, the interactions of the PC medium with the radiating resonance modes are not necessarily weakened.

Applications such as photovoltaics and photocatalysis that depend on absorption of the photoactive material could benefit from this phenomenon of increased absorption of the resonance modes. The amplitude of the *i*th steady-state resonance mode in the presence of material absorption can be approximated from temporal-coupled wave theory as shown in Equation 3.10 [286, 288]:

$$a_i = \frac{gs}{i(\omega - \omega_0) + \Gamma_{rad,i} + \Gamma_{abs,i}} \tag{3.10}$$

where g and s are the coupling strength and the amplitude of the incident field, respectively; ω_0 is the resonance frequency; and Γ_{rad} and Γ_{abs} are the decay rates, i.e., the reciprocals of the radiation and absorption lifetimes. The power absorbed in the *i*th mode is therefore approximated as:

$$P_{abs} \propto \Gamma_{abs}|a_i|^2 = \frac{\Gamma_{abs}|g|^2|s|^2}{(\omega - \omega_0)^2 + (\Gamma_{rad,i} + \Gamma_{abs,i})^2} \tag{3.11}$$

which can be maximized at the resonance frequency ω_0, if the absorption strength is comparable to the radiative strength. In the presence of material absorption, the widths of the resonances are also broadened so that a larger range of frequencies is capable of inducing stronger absorption in the media. Additionally, the integrated absorbed power associated with a specific resonance (photonic band) always increases with increasing material absorption strength.

Based on this analysis, using 2D PC slabs in absorptive materials should enable spectral modulation, including absorption and transmission tuning, with

careful control of the PC parameters. Broadband transmission and reflection selectivity is controlled primarily by the average optical properties of the slab, i.e. the effective refractive index. The smoothly varying background in the reflection spectra can be very accurately fitted assuming an optically uniform slab with slight dispersion in the dielectric constant that varies around the average dielectric constant of the PC slab. Broadband transmission and reflection tuning is therefore effectively only dependent on the volume ratio of the periodic voids (low-index inclusions), the slab thickness, and the properties of the high-index material. The spectral locations of the sharp resonant features corresponding to the photonic bands within the material, on the other hand, are highly dependent on the PC structural properties, such as the periods and shapes of the voids, not on the slab thickness and high-to-low index material volume ratio. Additionally, due to the optical scalability of PC structures in the absence of strong dispersion, specific spectral features can be easily shifted to preferred frequency ranges simply by scaling the structure accordingly. The addition of material absorption allows abrupt spectral features to be smoothed and broadened without significant shifts in frequency or decreases in the absorbed incident power, an additional tool that can be used to tailor transmission and reflection profiles.

3.4.3 Experimental demonstration of spectral tuning using PCs in strongly absorbing materials

Our simulation results indicate that the photonic band structure can be at least partially preserved in a PC fabricated in a strongly absorbing medium and

that this in-plane band structure has a strong effect on the out-of-plane transmission and reflection spectra. We sought to experimentally demonstrate this spectral tuning mechanism by fabricating a proof-of-principle PC structure in a strongly absorbing material with response in the infrared portion of the spectrum.

We chose to use a PbS CQD thin film as the absorbing media because of the demonstrated infrared absorption, facile solution processability, and applicability in many optoelectronic applications, including photodetectors, [289] LEDs [290] and solar cells [214, 192]. We used nanosphere self-assembly [291, 292] to construct a monolayer triangular lattice structure out of polystyrene beads, which served as the low-index material, and infiltrated them with PbS CQDs as the high-index absorbing material to form a photonic crystal-CQD (PC-CQD) structure. We optimized the PC-CQD film for transmittance in the visible regime using FDTD simulations. Our simulations aimed to mimic the realistic system by incorporating slight non-uniformity in the large-scale film thicknesses. We calculated the transmission by averaging the simulation results for 11 different film thicknesses for the PC-CQD case (250$\pm$50 nm) and 3 different film thicknesses for the CQD control case (200$\pm$10 nm), based on our experimental thickness measurements. As shown in Figures 3.19a-b, the PC-CQD film consisting of 250 nm beads in a monolayer triangular lattice array infiltrated with PbS CQDs displays a slight enhancement in visible transparency and a slight decrease in near-infrared (NIR) transparency compared to the control CQD film in both the simulation and experimental spectra. The electrical field profiles at the transmittance peak and valley of the 250 nm

PC-CQD film are shown in Figures 3.19 c and d, respectively. At the transmittance peak, the field is mainly confined within the low-index dielectric material, whereas at the transmittance valley, the field interacts more with the high-index absorbing media and thus more energy is absorbed at that wavelength.

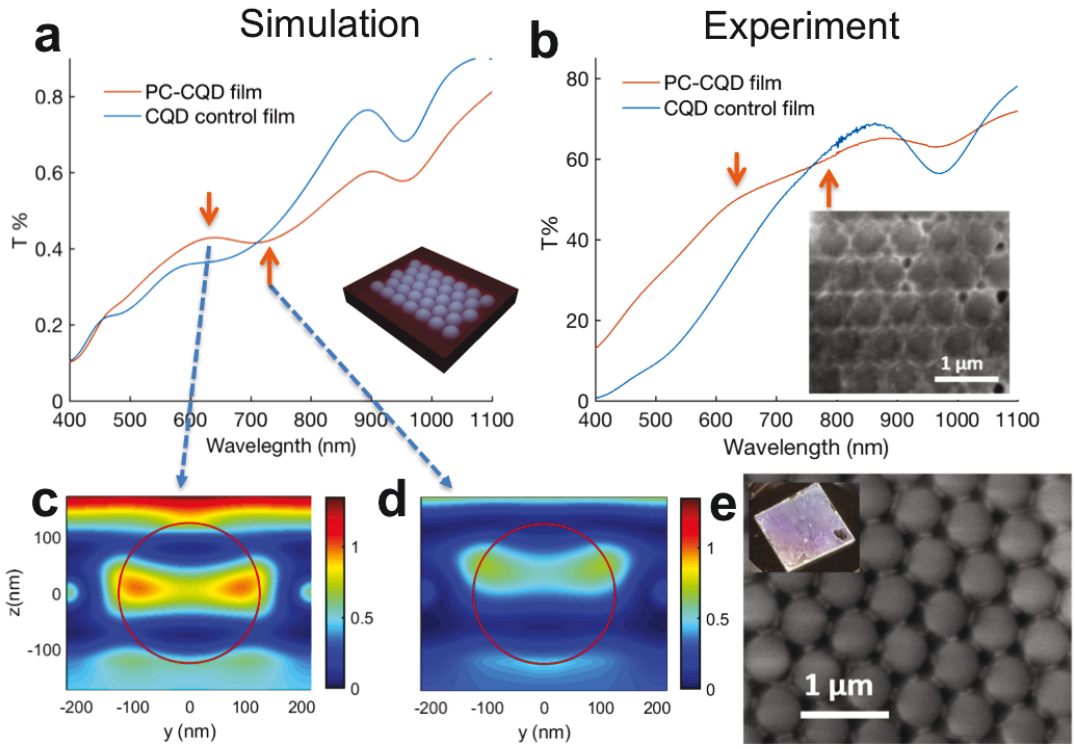

Figure 3.19: (a) FDTD-calculated transmittance for a control CQD film and a PC-CQD film. The inset is the PC-CQD structure: a triangular lattice monolayer of polystyrene beads infiltrated with PbS CQDs. The control CQD film is 200 nm thick on average, and the PC-CQD film consists of 250 nm diameter beads in a triangular array with a lattice constant of 250 nm; the space around the beads is filled with CQDs to form a 250 nm thick film on average. The spectra are averaged over several thicknesses to simulate roughness. The PC-CQD film shows a slight enhancement in visible transparency compared to the control CQD film. (b) UV-Vis-NIR spectrophotometric transmittance spectra of the PC-CQD film and the control CQD film, showing qualitative agreement with the FDTD calculations. Absolute difference in transmittance can be attributed to large-area non-uniformities in the films. Inset: Top-view SEM image of the PC-CQD structure consisting of mildly-etched self-assembled polystyrene beads infiltrated with PbS CQDs. (c) FDTD-calculated cross-section of the spatial electric field profile at the transmittance peak (d) valley. (e) Top-view SEM image of the etched bead array before CQD infiltration. The inset is a photo of the 1 inch x 1 inch bead array on a glass substrate before CQD infiltration. Large-scale order can be inferred from the strong iridescence of the structure.

To fabricate the PC-CQD film, we started by treating glass substrates with an O_2 plasma to make them hydrophilic and spin-cast 50 μL of an aqueous

solution of polystyrene beads at a concentration of 10% w/v purchased from Magsphere at a speed of 500 rpm for 10 seconds, followed by a 2-minute 700 rpm drying step. The beads self-assemble to form a close-packed triangular array with a lattice constant equal to the bead diameter. We then applied an O_2 plasma etching step at 120 W for a few minutes to open up space between the beads, adjusting the time to control the ratio of the bead radius-to-lattice constant. A scanning electron microscope (SEM) image of the bead array after etching is shown Figure 3.19e, and the inset contains a photograph of the 1 inch x 1 inch sample, which shows strong iridescence from the beads, indicating large-scale order. We synthesized oleic-acid capped PbS CQDs following previously published methods [293] and deposited the control CQD films from octane at a concentration of 50 mg/mL via a layer-by-layer spin-casting and 3-mercaptopropionic acid (MPA) ligand exchange process [293] to build up a film of the desired thickness. We used a lower concentration CQD solution (10 mg/mL) while keeping the concentration of the MPA-in-methanol solution at 1% by volume, to promote infiltration of the CQDs into the bead array. An SEM image of the PC-CQD film is shown in the inset of Figure 3.19b, showing preservation of the bead array and infiltration of the CQDs. Optical transmittance spectra of the PC-CQD and control films are shown in Figure 3.19b and were measured by placing samples at the entrance of an integrating sphere in a UV-Vis-NIR spectrophotometer. The experimental data is in rough qualitative agreement with the FDTD simulation results: the PC-CQD film shows a slight enhancement in visible transparency with a peak visible in both the experimental and simulation spectra at approximately 630 nm. The peaks and valleys of the experimental spectra are broadened and reduced in

intensity compared to the simulated spectra, most likely due to non-uniformity across the films and significant surface roughness that results in reduction of interference effects. Although preliminary, these results demonstrate that photonic structuring in strongly absorbing materials can result in significant modulation of the optical spectra which could be a useful tuning knob for optoelectronic applications. Future work will involve complete photonic band structure calculations to identify optimal structures that can be fabricated using CQD materials with targeted spectral properties for specific device applications.

3.4.4 Summary and Outlook

We developed and analyzed a new strategy for tuning the spectral selectivity of optoelectronic thin films: using photonic band engineering in strongly absorbing materials in which in-plane photonic bands are used to control the spectral properties of the out-of-plane reflection and transmission spectra. We analyzed a model system composed of a semiconductor-based slab photonic crystal in which the photonic bands of interest are located in the absorbing region of the material. By artificially varying k in FDTD and FMM simulations, we were able to quantify the impact of absorption on the photonic band structure. Specifically, adding absorption had little impact on the frequency of the photonic bands, although the widths of the bands were broadened and the quality factors of the in-plane modes decreased and saturated with increasing material absorption. Our FMM analysis showed that coupling between the

photonic bands at the γ point and normal-incidence wave induces sharp resonance features over the smoothly varying background in the reflection and transmission spectra, which can lead to strong frequency-dependent variations in the reflectivity and transmissivity associated with Fano resonances, even in the presence of material absorption. These results indicate that PC structures in strongly absorbing media can be used to produce spectrally selective optoelectronic thin films for targeted applications by careful adjustment of the lattice parameters.

Experimentally, we demonstrated the use of photonic structuring to tune the transmission spectrum of a strongly absorbing material by fabricating a proof-of-principle structure consisting of a self-assembled polystyrene bead monolayer infiltrated with PbS CQDs. The PC-CQD structure showed both near-infrared absorption enhancement and visible transparency enhancement over a control homogeneous CQD film of the same thickness, qualitatively matching predictions.

Future work will focus on extending these results by calculating full photonic band structures for solution-processed systems and including realistic dispersion in the optical models. We will use the insights gained from this study to design spectrally-selective photoactive optoelectronic films for targeted applications such as narrow-band infrared photodetectors and infrared solar cell materials for multijunction photovoltaics. The platform described here should form the basis for a new way to think about using photonic band structure engineering to control the spectral selectivity of strongly absorbing materials.

References

[1] Ting Xie, Md Rezaul Hasan, Botong Qiu, Ebuka S Arinze, Nhan V Nguyen, Abhishek Motayed, Susanna M Thon, and Ratan Debnath. "High-performing visible-blind photodetectors based on SnO2/CuO nanoheterojunctions". In: *Applied physics letters* 107.24 (2015), p. 241108.

[2] Kenji Nomura, Hiromichi Ohta, Kazushige Ueda, Toshio Kamiya, Masahiro Hirano, and Hideo Hosono. "Thin-film transistor fabricated in single-crystalline transparent oxide semiconductor". In: *Science* 300.5623 (2003), pp. 1269–1272.

[3] Kenji Nomura, Hiromichi Ohta, Akihiro Takagi, Toshio Kamiya, Masahiro Hirano, and Hideo Hosono. "Room-temperature fabrication of transparent flexible thin-film transistors using amorphous oxide semiconductors". In: *Nature* 432.7016 (2004), p. 488.

[4] Tadatsugu Minami. "Transparent conducting oxide semiconductors for transparent electrodes". In: *Semiconductor science and technology* 20.4 (2005), S35.

[5] Ratan Debnath, Ting Xie, Baomei Wen, Wei Li, Jong Y Ha, Nichole F Sullivan, Nhan V Nguyen, and Abhishek Motayed. "A solution-processed high-efficiency p-NiO/n-ZnO heterojunction photodetector". In: *Rsc Advances* 5.19 (2015), pp. 14646–14652.

[6] Ting Xie, Guannan Liu, Baomei Wen, Jong Y Ha, Nhan V Nguyen, Abhishek Motayed, and Ratan Debnath. "Tunable ultraviolet photoresponse in solution-processed p–n junction photodiodes based on transition-metal oxides". In: *ACS applied materials & interfaces* 7.18 (2015), pp. 9660–9667.

[7] YY Xi, YF Hsu, AB Djurišić, AMC Ng, WK Chan, HL Tam, and KW Cheah. "Ni O/ Zn O light emitting diodes by solution-based growth". In: *Applied Physics Letters* 92.11 (2008), p. 113505.

[8] Ya-Qing Bie, Zhi-Min Liao, Hong-Zhou Zhang, Guang-Ru Li, Yu Ye, Yang-Bo Zhou, Jun Xu, Zhi-Xin Qin, Lun Dai, and Da-Peng Yu. "Self-Powered, ultrafast, visible-blind UV detection and optical logical operation based on ZnO/GaN Nanoscale p-n junctions". In: *Advanced Materials* 23.5 (2011), pp. 649–653.

[9] Wei Zhang, Jin Xu, Wei Ye, Yang Li, Zhiqiang Qi, Jiangnan Dai, Zhihao Wu, Changqing Chen, Jun Yin, Jing Li, et al. "High-performance AlGaN metal–semiconductor–metal solar-blind ultraviolet photodetectors by localized surface plasmon enhancement". In: *Applied Physics Letters* 106.2 (2015), p. 021112.

[10] Linfeng Hu, Jian Yan, Meiyong Liao, Limin Wu, and Xiaosheng Fang. "Ultrahigh external quantum efficiency from thin SnO2 nanowire ultraviolet photodetectors". In: *Small* 7.8 (2011), pp. 1012–1017.

[11] Yujin Chen, Chunling Zhu, Maosheng Cao, and Taihong Wang. "Photoresponse of SnO2 nanobelts grown in situ on interdigital electrodes". In: *Nanotechnology* 18.28 (2007), p. 285502.

[12] Sanjay Mathur, Sven Barth, Hao Shen, Jae-Chul Pyun, and Ulf Werner. "Size-dependent photoconductance in SnO2 nanowires". In: *Small* 1.7 (2005), pp. 713–717.

[13] Hao Chen, Linfeng Hu, Xiaosheng Fang, and Limin Wu. "General Fabrication of Monolayer SnO2 Nanonets for High-Performance Ultraviolet Photodetectors". In: *Advanced Functional Materials* 22.6 (2012), pp. 1229–1235.

[14] Takayoshi Oshima, Takeya Okuno, and Shizuo Fujita. "UV-B sensor based on a SnO2 thin film". In: *Japanese Journal of Applied Physics* 48.12R (2009), p. 120207.

[15] Kewei Liu, Makoto Sakurai, Masakazu Aono, and Dezhen Shen. "Ultrahigh-Gain Single SnO2 Microrod Photoconductor on Flexible Substrate with Fast Recovery Speed". In: *Advanced Functional Materials* 25.21 (2015), pp. 3157–3163.

[16] Wei Tian, Chao Zhang, Tianyou Zhai, Song-Lin Li, Xi Wang, Meiyong Liao, Kazuhito Tsukagoshi, Dmitri Golberg, and Yoshio Bando. "Flexible SnO 2 hollow nanosphere film based high-performance ultraviolet photodetector". In: *Chemical Communications* 49.36 (2013), pp. 3739–3741.

[17] Cheng-Hua Lin, Reui-San Chen, Tzung-Te Chen, Hsin-Yi Chen, Yang-Fang Chen, Kuei-Hsien Chen, and Li-Chyong Chen. "High photocurrent gain in SnO 2 nanowires". In: *Applied Physics Letters* 93.11 (2008), p. 112115.

[18] Irina Giebelhaus, Elena Varechkina, Thomas Fischer, Marina Rumyantseva, Vladimir Ivanov, Alexander Gaskov, Joan Ramon Morante, Jordi Arbiol, Wieland Tyrra, and Sanjay Mathur. "One-dimensional CuO–SnO 2 p–n heterojunctions for enhanced detection of H 2 S". In: *Journal of Materials Chemistry A* 1.37 (2013), pp. 11261–11268.

[19] Xinyu Xue, Lili Xing, Yujin Chen, Songlin Shi, Yanguo Wang, and Taihong Wang. "Synthesis and H2S sensing properties of CuO- SnO2 core/shell pn-junction nanorods". In: *The Journal of Physical Chemistry C* 112.32 (2008), pp. 12157–12160.

[20] Lilai Liu, Maozhong An, Peixia Yang, and Jinqiu Zhang. "Superior cycle performance and high reversible capacity of SnO 2/graphene composite as an anode material for lithium-ion batteries". In: *Scientific reports* 5 (2015), p. 9055.

[21] RP Vasquez. "CuO by XPS". In: *Surface Science Spectra* 5.4 (1998), pp. 262–266.

[22] Dahlang Tahir and Sven Tougaard. "Electronic and optical properties of Cu, CuO and Cu2O studied by electron spectroscopy". In: *Journal of physics: Condensed matter* 24.17 (2012), p. 175002.

[23] RP Vasquez. "Cu2O by XPS". In: *Surface Science Spectra* 5.4 (1998), pp. 257–261.

[24] ED Palik. "Handbook of Optical Constants of Solids II Academic". In: *New York* 19912 (1991).

[25] IH Malitson and MJ Dodge. "Refractive-index and birefringence of synthetic sapphire". In: *Journal Of The Optical Society Of America*. Vol. 62. 11. AMER INST PHYSICS CIRCULATION FULFILLMENT DIV, 500 SUNNYSIDE BLVD, WOODBURY, NY 11797-2999. 1972, pp. 1405–1405.

[26] FP Koffyberg and FA Benko. "A photoelectrochemical determination of the position of the conduction and valence band edges of p-type CuO". In: *Journal of Applied Physics* 53.2 (1982), pp. 1173–1177.

[27] J Robertson, K Xiong, and SJ Clark. "Band gaps and defect levels in functional oxides". In: *Thin Solid Films* 496.1 (2006), pp. 1–7.

[28] Ebuka S Arinze, Botong Qiu, Gabrielle Nyirjesy, and Susanna M Thon. "Plasmonic nanoparticle enhancement of solution-processed solar cells: practical limits and opportunities". In: *ACS Photonics* 3.2 (2016), pp. 158–173.

[29] D Aaron R Barkhouse, Andras G Pattantyus-Abraham, Larissa Levina, and Edward H Sargent. "Thiols passivate recombination centers in colloidal quantum dots leading to enhanced photovoltaic device efficiency". In: *ACS nano* 2.11 (2008), pp. 2356–2362.

[30] Sung Heum Park, Anshuman Roy, Serge Beaupré, Shinuk Cho, Nelson Coates, Ji Sun Moon, Daniel Moses, Mario Leclerc, Kwanghee Lee, and Alan J Heeger. "Bulk heterojunction solar cells with internal quantum efficiency approaching 100%". In: *Nature photonics* 3.5 (2009), p. 297.

[31] Yongye Liang, Danqin Feng, Yue Wu, Szu-Ting Tsai, Gang Li, Claire Ray, and Luping Yu. "Highly efficient solar cell polymers developed via fine-tuning of structural and electronic properties". In: *Journal of the American Chemical Society* 131.22 (2009), pp. 7792–7799.

[32] Michael M Lee, Joël Teuscher, Tsutomu Miyasaka, Takurou N Murakami, and Henry J Snaith. "Efficient hybrid solar cells based on meso-superstructured organometal halide perovskites". In: *Science* (2012), p. 1228604.

[33] Paul Heremans, David Cheyns, and Barry P Rand. "Strategies for increasing the efficiency of heterojunction organic solar cells: material selection and device architecture". In: *Accounts of chemical research* 42.11 (2009), pp. 1740–1747.

[34] Jin Young Kim, Sun Hee Kim, H-H Lee, Kwanghee Lee, Wanli Ma, Xiong Gong, and Alan J Heeger. "New architecture for high-efficiency polymer photovoltaic cells using solution-based titanium oxide as an optical spacer". In: *Advanced materials* 18.5 (2006), pp. 572–576.

[35] Illan J Kramer and Edward H Sargent. "The architecture of colloidal quantum dot solar cells: materials to devices". In: *Chemical reviews* 114.1 (2013), pp. 863–882.

[36] Jeong-Hyeok Im, Chang-Ryul Lee, Jin-Wook Lee, Sang-Won Park, and Nam-Gyu Park. "6.5% efficient perovskite quantum-dot-sensitized solar cell". In: *Nanoscale* 3.10 (2011), pp. 4088–4093.

[37] Jin Hyuck Heo, Sang Hyuk Im, Jun Hong Noh, Tarak N Mandal, Choong-Sun Lim, Jeong Ah Chang, Yong Hui Lee, Hi-jung Kim, Arpita Sarkar, Md K Nazeeruddin, et al. "Efficient inorganic–organic hybrid heterojunction solar cells containing perovskite compound and polymeric hole conductors". In: *Nature photonics* 7.6 (2013), p. 486.

[38] Ali Dabirian and Nima Taghavinia. "Theoretical study of light trapping in nanostructured thin film solar cells using wavelength-scale silver particles". In: *ACS applied materials & interfaces* 7.27 (2015), pp. 14926–14932.

[39] Michael Niggemann, Moritz Riede, Andreas Gombert, and Karl Leo. "Light trapping in organic solar cells". In: *physica status solidi (a)* 205.12 (2008), pp. 2862–2874.

[40] Seung-Bum Rim, Shanbin Zhao, Shawn R Scully, Michael D McGehee, and Peter Peumans. "An effective light trapping configuration for thin-film solar cells". In: *Applied Physics Letters* 91.24 (2007), p. 243501.

[41] Albert Polman and Harry A Atwater. "Photonic design principles for ultrahigh-efficiency photovoltaics". In: *Nature materials* 11.3 (2012), p. 174.

[42] Chun-Hsien Chou and Fang-Chung Chen. "Plasmonic nanostructures for light trapping in organic photovoltaic devices". In: *Nanoscale* 6.15 (2014), pp. 8444–8458.

[43] Wei Zhang, Michael Saliba, Samuel D Stranks, Yao Sun, Xian Shi, Ulrich Wiesner, and Henry J Snaith. "Enhancement of perovskite-based solar cells employing core–shell metal nanoparticles". In: *Nano letters* 13.9 (2013), pp. 4505–4510.

[44] Harry A Atwater. "The promise of plasmonics". In: *Scientific American* 296.4 (2007), pp. 56–62.

[45] Dmitri K Gramotnev and Sergey I Bozhevolnyi. "Plasmonics beyond the diffraction limit". In: *Nature photonics* 4.2 (2010), p. 83.

[46] Jon A Schuller, Edward S Barnard, Wenshan Cai, Young Chul Jun, Justin S White, and Mark L Brongersma. "Plasmonics for extreme light concentration and manipulation". In: *Nature materials* 9.3 (2010), p. 193.

[47] Stefan A Maier and Harry A Atwater. "Plasmonics: Localization and guiding of electromagnetic energy in metal/dielectric structures". In: *Journal of applied physics* 98.1 (2005), p. 10.

[48] Ekmel Ozbay. "Plasmonics: merging photonics and electronics at nanoscale dimensions". In: *science* 311.5758 (2006), pp. 189–193.

[49] Stefan Alexander Maier. *Plasmonics: fundamentals and applications*. Springer Science & Business Media, 2007.

[50] Ching W Tang. "Two-layer organic photovoltaic cell". In: *Applied Physics Letters* 48.2 (1986), pp. 183–185.

[51] Wade A Luhman and Russell J Holmes. "Investigation of energy transfer in organic photovoltaic cells and impact on exciton diffusion length measurements". In: *Advanced Functional Materials* 21.4 (2011), pp. 764–771.

[52] Oleksandr V Mikhnenko, Hamed Azimi, Markus Scharber, Mauro Morana, Paul WM Blom, and Maria Antonietta Loi. "Exciton diffusion length in narrow bandgap polymers". In: *Energy & Environmental Science* 5.5 (2012), pp. 6960–6965.

[53] Thomas Stübinger and Wolfgang Brütting. "Exciton diffusion and optical interference in organic donor–acceptor photovoltaic cells". In: *Journal of Applied Physics* 90.7 (2001), pp. 3632–3641.

[54] Richard R Lunt, Noel C Giebink, Anna A Belak, Jay B Benziger, and Stephen R Forrest. "Exciton diffusion lengths of organic semiconductor thin films measured by spectrally resolved photoluminescence quenching". In: *Journal of Applied Physics* 105.5 (2009), p. 053711.

[55] Paul E Shaw, Arvydas Ruseckas, and Ifor DW Samuel. "Exciton diffusion measurements in poly (3-hexylthiophene)". In: *Advanced Materials* 20.18 (2008), pp. 3516–3520.

[56] Masahiro Hiramoto, Hiroshi Fujiwara, and Masaaki Yokoyama. "p-i-n like behavior in three-layered organic solar cells having a co-deposited interlayer of pigments". In: *Journal of applied physics* 72.8 (1992), pp. 3781–3787.

[57] JJM Halls, CA Walsh, Neil C Greenham, EA Marseglia, Richard H Friend, SC Moratti, and AB Holmes. "Efficient photodiodes from interpenetrating polymer networks". In: *Nature* 376.6540 (1995), p. 498.

[58] Jeffery Peet, C Soci, RC Coffin, TQ Nguyen, A Mikhailovsky, Daniel Moses, and Guillermo C Bazan. "Method for increasing the photoconductive response in conjugated polymer/fullerene composites". In: *Applied physics letters* 89.25 (2006), p. 252105.

[59] Jeffery Peet, Jin Young Kim, Nelson E Coates, Wang Li Ma, Daniel Moses, Alan J Heeger, and Guillermo C Bazan. "Efficiency enhancement in low-bandgap polymer solar cells by processing with alkane dithiols". In: *Nature materials* 6.7 (2007), p. 497.

[60] Wei Chen, Maxim P Nikiforov, and Seth B Darling. "Morphology characterization in organic and hybrid solar cells". In: *Energy & Environmental Science* 5.8 (2012), pp. 8045–8074.

[61] Andras G Pattantyus-Abraham, Illan J Kramer, Aaron R Barkhouse, Xihua Wang, Gerasimos Konstantatos, Ratan Debnath, Larissa Levina, Ines Raabe, Mohammad K Nazeeruddin, Michael Gratzel, et al. "Depleted-heterojunction colloidal quantum dot solar cells". In: *ACS nano* 4.6 (2010), pp. 3374–3380.

[62] Jiang Tang, Huan Liu, David Zhitomirsky, Sjoerd Hoogland, Xihua Wang, Melissa Furukawa, Larissa Levina, and Edward H Sargent. "Quantum junction solar cells". In: *Nano letters* 12.9 (2012), pp. 4889–4894.

[63] Chia-Hao M Chuang, Patrick R Brown, Vladimir Bulović, and Moungi G Bawendi. "Improved performance and stability in quantum dot solar cells through band alignment engineering". In: *Nature materials* 13.8 (2014), p. 796.

[64] David Zhitomirsky, Oleksandr Voznyy, Larissa Levina, Sjoerd Hoogland, Kyle W Kemp, Alexander H Ip, Susanna M Thon, and Edward H Sargent. "Engineering colloidal quantum dot solids within and beyond the mobility-invariant regime". In: *Nature communications* 5 (2014), p. 3803.

[65] Hui-Seon Kim, Chang-Ryul Lee, Jeong-Hyeok Im, Ki-Beom Lee, Thomas Moehl, Arianna Marchioro, Soo-Jin Moon, Robin Humphry-Baker, Jun-Ho Yum, Jacques E Moser, et al. "Lead iodide perovskite sensitized all-solid-state submicron thin film mesoscopic solar cell with efficiency exceeding 9%". In: *Scientific reports* 2 (2012), p. 591.

[66] Dongqin Bi, Soo-Jin Moon, Leif Häggman, Gerrit Boschloo, Lei Yang, Erik MJ Johansson, Mohammad K Nazeeruddin, Michael Grätzel, and Anders Hagfeldt. "Using a two-step deposition technique to prepare perovskite (CH3 NH3PbI3) for thin film solar cells based on ZrO 2 and TiO 2 mesostructures". In: *Rsc Advances* 3.41 (2013), pp. 18762–18766.

[67] Jun Hong Noh, Sang Hyuk Im, Jin Hyuck Heo, Tarak N Mandal, and Sang Il Seok. "Chemical management for colorful, efficient, and stable inorganic–organic hybrid nanostructured solar cells". In: *Nano letters* 13.4 (2013), pp. 1764–1769.

[68] Lioz Etgar, Peng Gao, Zhaosheng Xue, Qin Peng, Aravind Kumar Chandiran, Bin Liu, Md K Nazeeruddin, and Michael GraÌĹtzel. "Mesoscopic CH3NH3PbI3/TiO2 heterojunction solar cells". In: *Journal of the American Chemical Society* 134.42 (2012), pp. 17396–17399.

[69] Matthew J Carnie, Cecile Charbonneau, Matthew L Davies, Joel Troughton, Trystan M Watson, Konrad Wojciechowski, Henry Snaith, and David A Worsley. "A one-step low temperature processing route for organolead halide perovskite solar cells". In: *Chemical communications* 49.72 (2013), pp. 7893–7895.

[70] James M Ball, Michael M Lee, Andrew Hey, and Henry J Snaith. "Low-temperature processed meso-superstructured to thin-film perovskite solar cells". In: *Energy & Environmental Science* 6.6 (2013), pp. 1739–1743.

[71] Dong Shi, Valerio Adinolfi, Riccardo Comin, Mingjian Yuan, Erkki Alarousu, Andrei Buin, Yin Chen, Sjoerd Hoogland, Alexander Rothenberger, Khabiboulakh Katsiev, et al. "Low trap-state density and long carrier diffusion in organolead trihalide perovskite single crystals". In: *Science* 347.6221 (2015), pp. 519–522.

[72] Wanyi Nie, Hsinhan Tsai, Reza Asadpour, Jean-Christophe Blancon, Amanda J Neukirch, Gautam Gupta, Jared J Crochet, Manish Chhowalla, Sergei Tretiak, Muhammad A Alam, et al. "High-efficiency solution-processed perovskite solar cells with millimeter-scale grains". In: *Science* 347.6221 (2015), pp. 522–525.

[73] Eli Yablonovitch. "Statistical ray optics". In: *JOSA* 72.7 (1982), pp. 899–907.

[74] Adolf Goetzberger. "Optical confinement in thin Si-solar cells by diffuse back reflectors". In: *15th Photovoltaic Specialists Conference*. 1981, pp. 867–870.

[75] Patrick Campbell and Martin A Green. "The limiting efficiency of silicon solar cells under concentrated sunlight". In: *IEEE Transactions on Electron Devices* 33.2 (1986), pp. 234–239.

[76] Carl HaÌĹgglund, S Peter Apell, and Bengt Kasemo. “Maximized optical absorption in ultrathin films and its application to plasmon-based two-dimensional photovoltaics”. In: *Nano letters* 10.8 (2010), pp. 3135–3141.

[77] Zongfu Yu, Aaswath Raman, and Shanhui Fan. “Fundamental limit of nanophotonic light trapping in solar cells”. In: *Proceedings of the National Academy of Sciences* 107.41 (2010), pp. 17491–17496.

[78] Dennis M Callahan, Jeremy N Munday, and Harry A Atwater. “Solar cell light trapping beyond the ray optic limit”. In: *Nano letters* 12.1 (2012), pp. 214–218.

[79] Christian S Schuster, Angelo Bozzola, Lucio C Andreani, and Thomas F Krauss. “How to assess light trapping structures versus a Lambertian Scatterer for solar cells?” In: *Optics Express* 22.102 (2014), A542–A551.

[80] Surbhi Lal, Stephan Link, and Naomi J Halas. “Nano-optics from sensing to waveguiding”. In: *Nature photonics* 1.11 (2007), p. 641.

[81] AV Kabashin, P Evans, S Pastkovsky, W Hendren, GA Wurtz, R Atkinson, R Pollard, VA Podolskiy, and AV Zayats. “Plasmonic nanorod metamaterials for biosensing”. In: *Nature materials* 8.11 (2009), p. 867.

[82] Na Liu, Thomas Weiss, Martin Mesch, Lutz Langguth, Ulrike Eigenthaler, Michael Hirscher, Carsten Sonnichsen, and Harald Giessen. “Planar metamaterial analogue of electromagnetically induced transparency for plasmonic sensing”. In: *Nano letters* 10.4 (2009), pp. 1103–1107.

[83] Min-Ki Kwon, Ja-Yeon Kim, Baek-Hyun Kim, Il-Kyu Park, Chu-Young Cho, Clare Chisu Byeon, and Seong-Ju Park. “Surface-plasmon-enhanced light-emitting diodes”. In: *Advanced Materials* 20.7 (2008), pp. 1253–1257.

[84] Koichi Okamoto, Isamu Niki, Alexander Shvartser, Yukio Narukawa, Takashi Mukai, and Axel Scherer. “Surface-plasmon-enhanced light emitters based on InGaN quantum wells”. In: *Nature materials* 3.9 (2004), p. 601.

[85] Jelena Vučković, Marko Lončar, and Axel Scherer. “Surface plasmon enhanced light-emitting diode”. In: *IEEE Journal of Quantum Electronics* 36.10 (2000), pp. 1131–1144.

[86] Rupert F Oulton, Volker J Sorger, Thomas Zentgraf, Ren-Min Ma, Christopher Gladden, Lun Dai, Guy Bartal, and Xiang Zhang. "Plasmon lasers at deep subwavelength scale". In: *Nature* 461.7264 (2009), p. 629.

[87] Ren-Min Ma, Rupert F Oulton, Volker J Sorger, Guy Bartal, and Xiang Zhang. "Room-temperature sub-diffraction-limited plasmon laser by total internal reflection". In: *Nature materials* 10.2 (2011), p. 110.

[88] Malte C Gather. "A rocky road to plasmonic lasers". In: *Nature Photonics* 6.11 (2012), p. 708.

[89] Gerasimos Konstantatos and Edward H Sargent. "Nanostructured materials for photon detection". In: *Nature nanotechnology* 5.6 (2010), p. 391.

[90] Rashid Zia, Jon A Schuller, Anu Chandran, and Mark L Brongersma. "Plasmonics: the next chip-scale technology". In: *Materials today* 9.7-8 (2006), pp. 20–27.

[91] Harry A Atwater and Albert Polman. "Plasmonics for improved photovoltaic devices". In: *Nature materials* 9.3 (2010), p. 205.

[92] S Pillai, and MA Green. "Plasmonics for photovoltaic applications". In: *Solar Energy Materials and Solar Cells* 94.9 (2010), pp. 1481–1486.

[93] R Santbergen, TL Temple, R Liang, AHM Smets, RACMM Van Swaaij, and M Zeman. "Application of plasmonic silver island films in thin-film silicon solar cells". In: *Journal of Optics* 14.2 (2012), p. 024010.

[94] Vivian E Ferry, Jeremy N Munday, and Harry A Atwater. "Design considerations for plasmonic photovoltaics". In: *Advanced materials* 22.43 (2010), pp. 4794–4808.

[95] Keisuke Nakayama, Katsuaki Tanabe, and Harry A Atwater. "Plasmonic nanoparticle enhanced light absorption in GaAs solar cells". In: *Applied Physics Letters* 93.12 (2008), p. 121904.

[96] Martin A Green and Supriya Pillai. "Harnessing plasmonics for solar cells". In: *Nature Photonics* 6.3 (2012), p. 130.

[97] Vivian E Ferry, Luke A Sweatlock, Domenico Pacifici, and Harry A Atwater. "Plasmonic nanostructure design for efficient light coupling into solar cells". In: *Nano letters* 8.12 (2008), pp. 4391–4397.

[98] Vivian E Ferry, Marc A Verschuuren, Hongbo BT Li, Ruud EI Schropp, Harry A Atwater, and Albert Polman. "Improved red-response in thin film a-Si: H solar cells with soft-imprinted plasmonic back reflectors". In: *Applied Physics Letters* 95.18 (2009), p. 183503.

[99] V Giannini, Y Zhang, M Forcales, and J Gómez Rivas. "Long-range surface polaritons in ultra-thin films of silicon". In: *Optics Express* 16.24 (2008), pp. 19674–19685.

[100] Xi Chen, Baohua Jia, Jhantu K Saha, Boyuan Cai, Nicholas Stokes, Qi Qiao, Yongqian Wang, Zhengrong Shi, and Min Gu. "Broadband enhancement in thin-film amorphous silicon solar cells enabled by nucleated silver nanoparticles". In: *Nano letters* 12.5 (2012), pp. 2187–2192.

[101] Yang Wang, Tianyi Sun, Trilochan Paudel, Yi Zhang, Zhifeng Ren, and Krzysztof Kempa. "Metamaterial-plasmonic absorber structure for high efficiency amorphous silicon solar cells". In: *Nano letters* 12.1 (2011), pp. 440–445.

[102] Hairen Tan, Rudi Santbergen, Arno HM Smets, and Miro Zeman. "Plasmonic light trapping in thin-film silicon solar cells with improved self-assembled silver nanoparticles". In: *Nano letters* 12.8 (2012), pp. 4070–4076.

[103] Dong Hwan Wang, Do Youb Kim, Kyeong Woo Choi, Jung Hwa Seo, Sang Hyuk Im, Jong Hyeok Park, O Ok Park, and Alan J Heeger. "Enhancement of donor–acceptor polymer bulk heterojunction solar cell power conversion efficiencies by addition of Au nanoparticles". In: *Angewandte Chemie International Edition* 50.24 (2011), pp. 5519–5523.

[104] Dong Hwan Wang, Keum Hwan Park, Jung Hwa Seo, Jason Seifter, Ji Hye Jeon, Jung Kyu Kim, Jong Hyeok Park, O Ok Park, and Alan J Heeger. "Enhanced power conversion efficiency in PCDTBT/PC70BM bulk heterojunction photovoltaic devices with embedded silver nanoparticle clusters". In: *Advanced Energy Materials* 1.5 (2011), pp. 766–770.

[105] Charlie CD Wang, Wallace CH Choy, Chunhui Duan, Dixon DS Fung, EI Wei, Feng-Xian Xie, Fei Huang, and Yong Cao. "Optical and electrical effects of gold nanoparticles in the active layer of polymer solar cells". In: *Journal of Materials Chemistry* 22.3 (2012), pp. 1206–1211.

[106] Chu-Chen Chueh, Chang-Zhi Li, and Alex K-Y Jen. "Recent progress and perspective in solution-processed Interfacial materials for efficient and stable polymer and organometal perovskite solar cells". In: *Energy & Environmental Science* 8.4 (2015), pp. 1160–1189.

[107] Qiaoqiang Gan, Filbert J Bartoli, and Zakya H Kafafi. "Plasmonic-enhanced organic photovoltaics: Breaking the 10% efficiency barrier". In: *Advanced materials* 25.17 (2013), pp. 2385–2396.

[108] Jingbi You, Xuanhua Li, Feng-xian Xie, Wei EI Sha, Johnson HW Kwong, Gang Li, Wallace CH Choy, and Yang Yang. "Surface Plasmon and Scattering-Enhanced Low-Bandgap Polymer Solar Cell by a Metal Grating Back Electrode". In: *Advanced Energy Materials* 2.10 (2012), pp. 1203–1207.

[109] Xuanhua Li, Wallace CH Choy, Lijun Huo, Fengxian Xie, Wei EI Sha, Baofu Ding, Xia Guo, Yongfang Li, Jianhui Hou, Jingbi You, et al. "Dual plasmonic nanostructures for high performance inverted organic solar cells". In: *Advanced Materials* 24.22 (2012), pp. 3046–3052.

[110] Manuel J Mendes, Seweryn Morawiec, Francesca Simone, Francesco Priolo, and Isodiana Crupi. "Colloidal plasmonic back reflectors for light trapping in solar cells". In: *Nanoscale* 6.9 (2014), pp. 4796–4805.

[111] Gholamhosain Haidari, Morteza Hajimahmoodzadeh, Hamid Reza Fallah, and Mohsen Ghasemi Varnamkhasti. "Effective medium analysis of thermally evaporated Ag nanoparticle films for plasmonic enhancement in organic solar cell". In: *Superlattices and Microstructures* 85 (2015), pp. 294–304.

[112] Gholamhosain Haidari, Morteza Hajimahmoodzadeh, Hamid Reza Fallah, Andreas Peukert, Alina Chanaewa, and Elizabeth von Hauff. "Thermally evaporated Ag nanoparticle films for plasmonic enhancement in organic solar cells: effects of particle geometry". In: *physica status solidi (RRL)–Rapid Research Letters* 9.3 (2015), pp. 161–165.

[113] Bjoern Niesen, Barry P Rand, Pol Van Dorpe, David Cheyns, Lianming Tong, Alexandre Dmitriev, and Paul Heremans. "Plasmonic efficiency enhancement of high performance organic solar cells with a nanostructured rear electrode". In: *Advanced Energy Materials* 3.2 (2013), pp. 145–150.

[114] Kinam Jung, Hyung-Jun Song, Gunhee Lee, Youngjun Ko, KwangJun Ahn, Hoseop Choi, Jun Young Kim, Kyungyeon Ha, Jiyun Song, Jong-Kwon Lee, et al. "Plasmonic organic solar cells employing nanobump assembly via aerosol-derived nanoparticles". In: *ACS nano* 8.3 (2014), pp. 2590–2601.

[115] Fiona J Beck, Alexandros Stavrinadis, Silke L Diedenhofen, Tania Lasanta, and Gerasimos Konstantatos. "Surface plasmon polariton couplers for light trapping in thin-film absorbers and their application to colloidal quantum dot optoelectronics". In: *ACS Photonics* 1.11 (2014), pp. 1197–1205.

[116] Michael Salvador, Bradley A MacLeod, Angela Hess, Abhishek P Kulkarni, Keiko Munechika, Jennifer IL Chen, and David S Ginger. "Electron accumulation on metal nanoparticles in plasmon-enhanced organic solar cells". In: *ACS nano* 6.11 (2012), pp. 10024–10032.

[117] Daniel Paz-Soldan, Anna Lee, Susanna M Thon, Michael M Adachi, Haopeng Dong, Pouya Maraghechi, Mingjian Yuan, AndreÌĄ J Labelle, Sjoerd Hoogland, Kun Liu, et al. "Jointly tuned plasmonic–excitonic photovoltaics using nanoshells". In: *Nano letters* 13.4 (2013), pp. 1502–1508.

[118] Michael Saliba, Wei Zhang, Victor M Burlakov, Samuel D Stranks, Yao Sun, James M Ball, Michael B Johnston, Alain Goriely, Ulrich Wiesner, and Henry J Snaith. "Plasmonic-Induced Photon Recycling in Metal Halide Perovskite Solar Cells". In: *Advanced Functional Materials* 25.31 (2015), pp. 5038–5046.

[119] Abhishek P Kulkarni, Kevin M Noone, Keiko Munechika, Samuel R Guyer, and David S Ginger. "Plasmon-enhanced charge carrier generation in organic photovoltaic films using silver nanoprisms". In: *Nano letters* 10.4 (2010), pp. 1501–1505.

[120] TJ Echtermeyer, L Britnell, PK Jasnos, A Lombardo, RV Gorbachev, AN Grigorenko, AK Geim, AC Ferrari, and KS Novoselov. "Strong plasmonic enhancement of photovoltage in graphene". In: *Nature communications* 2 (2011), p. 458.

[121] Fang-Chung Chen, Jyh-Lih Wu, Chia-Ling Lee, Yi Hong, Chun-Hong Kuo, and Michael H Huang. "Plasmonic-enhanced polymer photovoltaic devices incorporating solution-processable metal nanoparticles". In: *Applied Physics Letters* 95.1 (2009), p. 182.

[122] Woo-Jun Yoon, Kyung-Young Jung, Jiwen Liu, Thirumalai Duraisamy, Rao Revur, Fernando L Teixeira, Suvankar Sengupta, and Paul R Berger. "Plasmon-enhanced optical absorption and photocurrent in organic bulk heterojunction photovoltaic devices using self-assembled layer of silver nanoparticles". In: *Solar Energy Materials and Solar Cells* 94.2 (2010), pp. 128–132.

[123] Nathan C Lindquist, Wade A Luhman, Sang-Hyun Oh, and Russell J Holmes. "Plasmonic nanocavity arrays for enhanced efficiency in organic photovoltaic cells". In: *Applied Physics Letters* 93.12 (2008), p. 350.

[124] Yu A Akimov, K Ostrikov, and EP Li. "Surface plasmon enhancement of optical absorption in thin-film silicon solar cells". In: *Plasmonics* 4.2 (2009), pp. 107–113.

[125] Carl HaÌĺgglund, Gabriel Zeltzer, Ricardo Ruiz, Isabell Thomann, Han-Bo-Ram Lee, Mark L Brongersma, and Stacey F Bent. "Self-assembly based plasmonic arrays tuned by atomic layer deposition for extreme visible light absorption". In: *Nano letters* 13.7 (2013), pp. 3352–3357.

[126] Sang Eon Han and Gang Chen. "Toward the Lambertian limit of light trapping in thin nanostructured silicon solar cells". In: *Nano letters* 10.11 (2010), pp. 4692–4696.

[127] C Ciracì, RT Hill, JJ Mock, Y Urzhumov, AI Fernández-Domínguez, SA Maier, JB Pendry, A Chilkoti, and DR Smith. "Probing the ultimate limits of plasmonic enhancement". In: *Science* 337.6098 (2012), pp. 1072–1074.

[128] Durmus U Karatay, Michael Salvador, Kai Yao, Alex K-Y Jen, and David S Ginger. "Performance limits of plasmon-enhanced organic photovoltaics". In: *Applied Physics Letters* 105.3 (2014), 109_1.

[129] Mattias Marklund, Gert Brodin, Lennart Stenflo, and Chuan S Liu. "New quantum limits in plasmonic devices". In: *EPL (Europhysics Letters)* 84.1 (2008), p. 17006.

[130] Jyh-Lih Wu, Fang-Chung Chen, Yu-Sheng Hsiao, Fan-Ching Chien, Peilin Chen, Chun-Hong Kuo, Michael H Huang, and Chain-Shu Hsu. "Surface plasmonic effects of metallic nanoparticles on the performance of polymer bulk heterojunction solar cells". In: *ACS nano* 5.2 (2011), pp. 959–967.

[131] Mei Xue, Lu Li, Bertrand J Tremolet de Villers, Huajun Shen, Jinfeng Zhu, Zhibin Yu, Adam Z Stieg, Qibing Pei, Benjamin J Schwartz, and Kang L Wang. "Charge-carrier dynamics in hybrid plasmonic organic solar cells with Ag nanoparticles". In: *Applied Physics Letters* 98.25 (2011), p. 119.

[132] Soo Won Heo, Eui Jin Lee, Kwan Wook Song, Jang Yong Lee, and Doo Kyung Moon. "Enhanced carrier mobility and photon-harvesting property by introducing Au nano-particles in bulk heterojunction photovoltaic cells". In: *Organic Electronics* 14.8 (2013), pp. 1931–1938.

[133] Xuanhua Li, Wallace Chik Ho Choy, Haifei Lu, Wei EI Sha, and Aaron Ho Pui Ho. "Efficiency Enhancement of Organic Solar Cells by Using Shape-Dependent Broadband Plasmonic Absorption in Metallic Nanoparticles". In: *Advanced Functional Materials* 23.21 (2013), pp. 2728–2735.

[134] Wanjung Kim, Bong Geun Cha, Jung Kyu Kim, Woonggi Kang, Eunchul Kim, Tae Kyu Ahn, Dong Hwan Wang, Qing Guo Du, Jeong Ho Cho, Jaeyun Kim, et al. "Tailoring dispersion and aggregation of Au nanoparticles in the BHJ layer of polymer solar cells: Plasmon effects versus electrical effects". In: *ChemSusChem* 7.12 (2014), pp. 3452–3458.

[135] Zelin Lu, Xujie Pan, Yingzhuang Ma, Yu Li, Lingling Zheng, Danfei Zhang, Qi Xu, Zhijian Chen, Shufeng Wang, Bo Qu, et al. "Plasmonic-enhanced perovskite solar cells using alloy popcorn nanoparticles". In: *RSC Advances* 5.15 (2015), pp. 11175–11179.

[136] Chao Shen, Hua Tong, Weichuan Gao, Shuanglong Yuan, Guorong Chen, and Yunxia Yang. "Effects of anode structures and fabrication methods on cell efficiencies of CdS/CdSe quantum dot co-sensitized solar cells". In: *Journal of Alloys and Compounds* 644 (2015), pp. 205–210.

[137] Natalia Kholmicheva, Pavel Moroz, Upendra Rijal, Ebin Bastola, Prakash Uprety, Geethika Liyanage, Anton Razgoniaev, Alexis D Ostrowski, and Mikhail Zamkov. "Plasmonic nanocrystal solar cells utilizing strongly confined radiation". In: *ACS nano* 8.12 (2014), pp. 12549–12559.

[138] Fiona J Beck, Tania Lasanta, and Gerasimos Konstantatos. "Plasmonic Schottky nanojunctions for tailoring the photogeneration profile in thin film solar cells". In: *Advanced Optical Materials* 2.5 (2014), pp. 493–500.

[139] Jiang Tang, Kyle W Kemp, Sjoerd Hoogland, Kwang S Jeong, Huan Liu, Larissa Levina, Melissa Furukawa, Xihua Wang, Ratan Debnath, Dongkyu Cha, et al. "Colloidal-quantum-dot photovoltaics using atomic-ligand passivation". In: *Nature materials* 10.10 (2011), p. 765.

[140] Xiaoliang Zhang, Jindan Zhang, Jianhua Liu, and Erik MJ Johansson. "Solution processed flexible and bending durable heterojunction colloidal quantum dot solar cell". In: *Nanoscale* 7.27 (2015), pp. 11520–11524.

[141] Xudong Yao, Yajing Chang, Guopeng Li, Longfei Mi, Shangjing Liu, Hui Wang, Yalan Yu, and Yang Jiang. "Inverted quantum-dot solar cells with depleted heterojunction structure employing CdS as the electron acceptor". In: *Solar Energy Materials and Solar Cells* 137 (2015), pp. 287–292.

[142] Gi-Hwan Kim, Bright Walker, Hak-Beom Kim, Jin Young Kim, Edward H Sargent, Jongnam Park, and Jin Young Kim. "Inverted colloidal quantum dot solar cells". In: *Advanced Materials* 26.20 (2014), pp. 3321–3327.

[143] Xinzheng Lan, Silvia Masala, and Edward H Sargent. "Charge-extraction strategies for colloidal quantum dot photovoltaics". In: *Nature materials* 13.3 (2014), p. 233.

[144] Pouya Maraghechi, André J Labelle, Ahmad R Kirmani, Xinzheng Lan, Michael M Adachi, Susanna M Thon, Sjoerd Hoogland, Anna Lee, Zhijun Ning, Armin Fischer, et al. "The donor–supply electrode enhances performance in colloidal quantum dot solar cells". In: *ACS nano* 7.7 (2013), pp. 6111–6116.

[145] Zhijun Ning, Oleksandr Voznyy, Jun Pan, Sjoerd Hoogland, Valerio Adinolfi, Jixian Xu, Min Li, Ahmad R Kirmani, Jon-Paul Sun, James Minor, et al. "Air-stable n-type colloidal quantum dot solids". In: *Nature materials* 13.8 (2014), p. 822.

[146] James M Gee. "The effect of parasitic absorption losses on light trapping in thin silicon solar cells". In: *Photovoltaic Specialists Conference, 1988., Conference Record of the Twentieth IEEE*. IEEE. 1988, pp. 549–554.

[147] UW Paetzold, F Hallermann, BE Pieters, U Rau, R Carius, and G Von Plessen. "Localized plasmonic losses at metal back contacts of thin-film silicon solar cells". In: *Photonics for Solar Energy Systems III*. Vol. 7725. International Society for Optics and Photonics. 2010, p. 772517.

[148] Jacob B Khurgin and Alexandra Boltasseva. "Reflecting upon the losses in plasmonics and metamaterials". In: *MRS bulletin* 37.8 (2012), pp. 768–779.

[149] U Palanchoke, V Jovanov, H Kurz, R Dewan, P Magnus, Helmut Stiebig, and D Knipp. "Influence of back contact roughness on light trapping and plasmonic losses of randomly textured amorphous silicon thin film solar cells". In: *Applied Physics Letters* 102.8 (2013), p. 083501.

[150] Peng Du, Pengtao Jing, Di Li, Yinghui Cao, Zhenyu Liu, and Zaicheng Sun. "Plasmonic Ag@ oxide nanoprisms for enhanced performance of organic solar cells". In: *Small* 11.20 (2015), pp. 2454–2462.

[151] Bo Wu, Nripan Mathews, and Tze Chien Sum. "Ag nanoparticle-blended plasmonic organic solar cells: performance enhancement or detraction?" In: *Physics, Simulation, and Photonic Engineering of Photovoltaic Devices III*. Vol. 8981. International Society for Optics and Photonics. 2014, p. 898111.

[152] M Magdalena Mandoc, Welmoed Veurman, L Jan Anton Koster, Bert de Boer, and Paul WM Blom. "Origin of the reduced fill factor and photocurrent in MDMO-PPV: PCNEPV all-polymer solar cells". In: *Advanced Functional Materials* 17.13 (2007), pp. 2167–2173.

[153] Jonathan A Scholl, Ai Leen Koh, and Jennifer A Dionne. "Quantum plasmon resonances of individual metallic nanoparticles". In: *Nature* 483.7390 (2012), p. 421.

[154] SJ Oldenburg, RD Averitt, SL Westcott, and NJ Halas. "Nanoengineering of optical resonances". In: *Chemical Physics Letters* 288.2-4 (1998), pp. 243–247.

[155] JJ Mock, M Barbic, DR Smith, DA Schultz, and S Schultz. "Shape effects in plasmon resonance of individual colloidal silver nanoparticles". In: *The Journal of Chemical Physics* 116.15 (2002), pp. 6755–6759.

[156] Jack J Mock, David R Smith, and Sheldon Schultz. "Local refractive index dependence of plasmon resonance spectra from individual nanoparticles". In: *Nano letters* 3.4 (2003), pp. 485–491.

[157] Eliza Hutter and Janos H Fendler. "Exploitation of localized surface plasmon resonance". In: *Advanced materials* 16.19 (2004), pp. 1685–1706.

[158] DAG Bruggeman. "Dielectric constant and conductivity of mixtures of isotropic materials". In: *Ann. Phys.(Leipzig)* 24 (1935), pp. 636–679.

[159] JC Maxwell Garnett. “VII. Colours in metal glasses, in metallic films, and in metallic solutions. −II”. In: *Phil. Trans. R. Soc. Lond. A* 205.387-401 (1906), pp. 237–288.

[160] Hendrik Christoffel Hulst and Hendrik C van de Hulst. *Light scattering by small particles*. Courier Corporation, 1981.

[161] Qiang Fu and Wenbo Sun. “Mie theory for light scattering by a spherical particle in an absorbing medium”. In: *Applied Optics* 40.9 (2001), pp. 1354–1361.

[162] M Futamata, Y Maruyama, and M Ishikawa. “Local electric field and scattering cross section of Ag nanoparticles under surface plasmon resonance by finite difference time domain method”. In: *The Journal of Physical Chemistry B* 107.31 (2003), pp. 7607–7617.

[163] Weihai Ni, Xiaoshan Kou, Zhi Yang, and Jianfang Wang. “Tailoring longitudinal surface plasmon wavelengths, scattering and absorption cross sections of gold nanorods”. In: *Acs Nano* 2.4 (2008), pp. 677–686.

[164] Bruce T Draine and Piotr J Flatau. “Discrete-dipole approximation for scattering calculations”. In: *JOSA A* 11.4 (1994), pp. 1491–1499.

[165] J-M Jin and Valdis V Liepa. “Application of hybrid finite element method to electromagnetic scattering from coated cylinders”. In: *IEEE transactions on antennas and propagation* 36.1 (1988), pp. 50–54.

[166] DF Swinehart. “The beer-lambert law”. In: *Journal of chemical education* 39.7 (1962), p. 333.

[167] Allen Taflove and Susan C Hagness. *Computational electrodynamics: the finite-difference time-domain method*. Artech house, 2005.

[168] Christopher JM Emmott, Jason A Röhr, Mariano Campoy-Quiles, Thomas Kirchartz, Antonio Urbina, Nicholas J Ekins-Daukes, and Jenny Nelson. “Organic photovoltaic greenhouses: a unique application for semi-transparent PV?” In: *Energy & environmental science* 8.4 (2015), pp. 1317–1328.

[169] Philipp LoÌĹper, Michael Stuckelberger, Bjoern Niesen, Jérémie Werner, Miha Filipic, Soo-Jin Moon, Jun-Ho Yum, Marko TopicÌŇ, Stefaan De Wolf, and Christophe Ballif. “Complex refractive index spectra of CH3NH3PbI3 perovskite thin films determined by spectroscopic ellipsometry and spectrophotometry”. In: *The journal of physical chemistry letters* 6.1 (2014), pp. 66–71.

[170] Sankara Rao Gollu, MS Murthy, Ramakant Sharma, G Srinivas, Swaroop Ganguly, and Dipti Gupta. "Enhanced efficiency of inverted bulk heterojunction solar cells with embedded silica nanoparticles". In: *Photovoltaic Specialist Conference (PVSC), 2014 IEEE 40th*. IEEE. 2014, pp. 1745–1749.

[171] NT Fofang, TS Luk, M Okandan, GN Nielson, and I Brener. "Substrate-modified scattering properties of silicon nanostructures for solar energy applications". In: *Optics Express* 21.4 (2013), pp. 4774–4782.

[172] S Tanev, VV Tuchin, and P Paddon. "Light scattering effects of gold nanoparticles in cells: FDTD modeling". In: *Laser Physics Letters* 3.12 (2006), p. 594.

[173] Shuang Jiang, Zhe Hu, Zhizhong Chen, Xingxing Fu, Xianzhe Jiang, Qianqian Jiao, Tongjun Yu, and Guoyi Zhang. "Resonant absorption and scattering suppression of localized surface plasmons in Ag particles on green LED". In: *Optics Express* 21.10 (2013), pp. 12100–12110.

[174] Huanjun Chen, Xiaoshan Kou, Zhi Yang, Weihai Ni, and Jianfang Wang. "Shape-and size-dependent refractive index sensitivity of gold nanoparticles". In: *Langmuir* 24.10 (2008), pp. 5233–5237.

[175] Kyeong-Seok Lee and Mostafa A El-Sayed. "Dependence of the enhanced optical scattering efficiency relative to that of absorption for gold metal nanorods on aspect ratio, size, end-cap shape, and medium refractive index". In: *The Journal of Physical Chemistry B* 109.43 (2005), pp. 20331–20338.

[176] Ming Li, Scott K Cushing, Jianming Zhang, Jessica Lankford, Zoraida P Aguilar, Dongling Ma, and Nianqiang Wu. "Shape-dependent surface-enhanced Raman scattering in gold–Raman-probe–silica sandwiched nanoparticles for biocompatible applications". In: *Nanotechnology* 23.11 (2012), p. 115501.

[177] Xianliang Wang, Xin Liu, Deqiang Yin, Yujie Ke, and Mark T Swihart. "Size-, shape-, and composition-controlled synthesis and localized surface plasmon resonance of copper tin selenide nanocrystals". In: *Chemistry of Materials* 27.9 (2015), pp. 3378–3388.

[178] Jian Zhu, Liqing Huang, Junwu Zhao, Yongchang Wang, Yanrui Zhao, Limei Hao, and Yimin Lu. "Shape dependent resonance light scattering properties of gold nanorods". In: *Materials Science and Engineering: B* 121.3 (2005), pp. 199–203.

[179] Prashant K Jain, Kyeong Seok Lee, Ivan H El-Sayed, and Mostafa A El-Sayed. "Calculated absorption and scattering properties of gold nanoparticles of different size, shape, and composition: applications in biological imaging and biomedicine". In: *The journal of physical chemistry B* 110.14 (2006), pp. 7238–7248.

[180] Andrea Tao, Prasert Sinsermsuksakul, and Peidong Yang. "Polyhedral silver nanocrystals with distinct scattering signatures". In: *Angewandte Chemie International Edition* 45.28 (2006), pp. 4597–4601.

[181] Jian Zhu. "Shape dependent full width at half maximum of the absorption band in gold nanorods". In: *Physics Letters A* 339.6 (2005), pp. 466–471.

[182] David D Evanoff Jr and George Chumanov. "Synthesis and optical properties of silver nanoparticles and arrays". In: *ChemPhysChem* 6.7 (2005), pp. 1221–1231.

[183] Sol Carretero-Palacios, Mauricio E Calvo, and Hernán Míguez. "Absorption enhancement in organic–inorganic halide perovskite films with embedded plasmonic gold nanoparticles". In: *The Journal of Physical Chemistry C* 119.32 (2015), pp. 18635–18640.

[184] F Pelayo García de Arquer, Fiona J Beck, and Gerasimos Konstantatos. "Absorption enhancement in solution processed metal-semiconductor nanocomposites". In: *Optics express* 19.21 (2011), pp. 21038–21049.

[185] Leif AA Pettersson, Lucimara S Roman, and Olle Inganäs. "Modeling photocurrent action spectra of photovoltaic devices based on organic thin films". In: *Journal of Applied Physics* 86.1 (1999), pp. 487–496.

[186] George F Burkhard, Eric T Hoke, and Michael D McGehee. "Accounting for interference, scattering, and electrode absorption to make accurate internal quantum efficiency measurements in organic and other thin solar cells". In: *Advanced Materials* 22.30 (2010), pp. 3293–3297.

[187] R Kern, R Sastrawan, J Ferber, R Stangl, and J Luther. "Modeling and interpretation of electrical impedance spectra of dye solar cells operated under open-circuit conditions". In: *Electrochimica Acta* 47.26 (2002), pp. 4213–4225.

[188] Paul A Basore. "Numerical modeling of textured silicon solar cells using PC-1D". In: *IEEE Transactions on electron devices* 37.2 (1990), pp. 337–343.

[189] Jörg Ferber, Rolf Stangl, and Joachim Luther. "An electrical model of the dye-sensitized solar cell". In: *Solar Energy Materials and Solar Cells* 53.1-2 (1998), pp. 29–54.

[190] Roderick CI MacKenzie, Thomas Kirchartz, George FA Dibb, and Jenny Nelson. "Modeling nongeminate recombination in P3HT: PCBM solar cells". In: *The Journal of Physical Chemistry C* 115.19 (2011), pp. 9806–9813.

[191] Weiwei Li, Koen H Hendriks, WS Christian Roelofs, Youngju Kim, Martijn M Wienk, and René AJ Janssen. "Efficient small bandgap polymer solar cells with high fill factors for 300 nm thick films". In: *Advanced materials* 25.23 (2013), pp. 3182–3186.

[192] Ebuka S Arinze, Botong Qiu, Nathan Palmquist, Yan Cheng, Yida Lin, Gabrielle Nyirjesy, Gary Qian, and Susanna M Thon. "Color-tuned and transparent colloidal quantum dot solar cells via optimized multilayer interference". In: *Optics Express* 25.4 (2017), A101–A112.

[193] Anne Grete Hestnes. "Building integration of solar energy systems". In: *Solar Energy* 67.4-6 (1999), pp. 181–187.

[194] Andreas Henemann. "BIPV: Built-in solar energy". In: *Renewable Energy Focus* 9.6 (2008), pp. 14–19.

[195] Zhong Lin Wang, Guang Zhu, Ya Yang, Sihong Wang, and Caofeng Pan. "Progress in nanogenerators for portable electronics". In: *Materials today* 15.12 (2012), pp. 532–543.

[196] Henrik Davidsson, Bengt Perers, and Björn Karlsson. "Performance of a multifunctional PV/T hybrid solar window". In: *Solar Energy* 84.3 (2010), pp. 365–372.

[197] T Miyazaki, A Akisawa, and T Kashiwagi. "Energy savings of office buildings by the use of semi-transparent solar cells for windows". In: *Renewable energy* 30.3 (2005), pp. 281–304.

[198] Hideo Otaka, Michie Kira, Kentaro Yano, Shunichiro Ito, Hirofumi Mitekura, Toshio Kawata, and Fumio Matsui. "Multi-colored dye-sensitized solar cells". In: *Journal of Photochemistry and Photobiology A: Chemistry* 164.1-3 (2004), pp. 67–73.

[199] Hui Joon Park, Ting Xu, Jae Yong Lee, Abram Ledbetter, and L Jay Guo. "Photonic color filters integrated with organic solar cells for energy harvesting". In: *Acs Nano* 5.9 (2011), pp. 7055–7060.

[200] Chu-Chen Chueh, Shang-Chieh Chien, Hin-Lap Yip, José Francisco Salinas, Chang-Zhi Li, Kung-Shih Chen, Fang-Chung Chen, Wen-Chang Chen, and Alex K-Y Jen. "Toward high-performance semi-transparent polymer solar cells: optimization of ultra-thin light absorbing layer and transparent cathode architecture". In: *Advanced Energy Materials* 3.4 (2013), pp. 417–423.

[201] Young-Hoon Kim, Himchan Cho, Jin Hyuck Heo, Tae-Sik Kim, NoSoung Myoung, Chang-Lyoul Lee, Sang Hyuk Im, and Tae-Woo Lee. "Multicolored organic/inorganic hybrid perovskite light-emitting diodes". In: *Advanced materials* 27.7 (2015), pp. 1248–1254.

[202] Kyu-Tae Lee, L Jay Guo, and Hui Joon Park. "Neutral-and multicolored semitransparent perovskite solar cells". In: *Molecules* 21.4 (2016), p. 475.

[203] Giles E Eperon, Victor M Burlakov, Alain Goriely, and Henry J Snaith. "Neutral color semitransparent microstructured perovskite solar cells". In: *ACS nano* 8.1 (2013), pp. 591–598.

[204] Cristina Roldan-Carmona, Olga Malinkiewicz, Rafael Betancur, Giulia Longo, Cristina Momblona, Franklin Jaramillo, Luis Camacho, and Henk J Bolink. "High efficiency single-junction semitransparent perovskite solar cells". In: *Energy & Environmental Science* 7.9 (2014), pp. 2968–2973.

[205] Jae Woong Jung, Chu-Chen Chueh, and Alex K-Y Jen. "High-Performance Semitransparent Perovskite Solar Cells with 10% Power Conversion Efficiency and 25% Average Visible Transmittance Based on Transparent CuSCN as the Hole-Transporting Material". In: *Advanced Energy Materials* 5.17 (2015), p. 1500486.

[206] Yulia Galagan, Michael G Debije, and Paul WM Blom. "Semitransparent organic solar cells with organic wavelength dependent reflectors". In: *Applied Physics Letters* 98.4 (2011), p. 16.

[207] Wei Zhang, Miguel Anaya, Gabriel Lozano, Mauricio E Calvo, Michael B Johnston, Hernán Míguez, and Henry J Snaith. "Highly efficient perovskite solar cells with tunable structural color". In: *Nano letters* 15.3 (2015), pp. 1698–1702.

[208] Kyu-Tae Lee, Masanori Fukuda, Suneel Joglekar, and L Jay Guo. "Colored, see-through perovskite solar cells employing an optical cavity". In: *Journal of Materials Chemistry C* 3.21 (2015), pp. 5377–5382.

[209] CeÌĄsar Omar RamiÌĄrez Quiroz, Carina Bronnbauer, Ievgen Levchuk, Yi Hou, Christoph J Brabec, and Karen Forberich. "Coloring semitransparent perovskite solar cells via dielectric mirrors". In: *ACS nano* 10.5 (2016), pp. 5104–5112.

[210] Johannes Krantz, Tobias Stubhan, Moses Richter, Stefanie Spallek, Ivan Litzov, Gebhard J Matt, Erdmann Spiecker, and Christoph J Brabec. "Spray-coated silver nanowires as top electrode layer in semitransparent P3HT: PCBM-based organic solar cell devices". In: *Advanced Functional Materials* 23.13 (2013), pp. 1711–1717.

[211] Yu-Ying Lee, Kun-Hua Tu, Chen-Chieh Yu, Shao-Sian Li, Jeong-Yuan Hwang, Chih-Cheng Lin, Kuei-Hsien Chen, Li-Chyong Chen, Hsuen-Li Chen, and Chun-Wei Chen. "Top laminated graphene electrode in a semitransparent polymer solar cell by simultaneous thermal annealing/releasing method". In: *ACS nano* 5.8 (2011), pp. 6564–6570.

[212] Robert Koeppe, Doris Hoeglinger, Pavel A Troshin, Rimma N Lyubovskaya, Vladimir F Razumov, and Niyazi Serdar Sariciftci. "Organic solar cells with semitransparent metal back contacts for power window applications". In: *ChemSusChem: Chemistry & Sustainability Energy & Materials* 2.4 (2009), pp. 309–313.

[213] Edward H Sargent. "Colloidal quantum dot solar cells". In: *Nature photonics* 6.3 (2012), p. 133.

[214] Graham H Carey, Ahmed L Abdelhady, Zhijun Ning, Susanna M Thon, Osman M Bakr, and Edward H Sargent. "Colloidal quantum dot solar cells". In: *Chemical reviews* 115.23 (2015), pp. 12732–12763.

[215] Margaret A Hines and Gregory D Scholes. "Colloidal PbS nanocrystals with size-tunable near-infrared emission: observation of post-synthesis self-narrowing of the particle size distribution". In: *Advanced Materials* 15.21 (2003), pp. 1844–1849.

[216] Y Wang, A Suna, W Mahler, and R Kasowski. "PbS in polymers. From molecules to bulk solids". In: *The Journal of chemical physics* 87.12 (1987), pp. 7315–7322.

[217] Jay N Zemel, James D Jensen, and Richard B Schoolar. "Electrical and optical properties of epitaxial films of PbS, PbSe, PbTe, and SnTe". In: *Physical Review* 140.1A (1965), A330.

[218] Saim Emin, Surya P Singh, Liyuan Han, Norifusa Satoh, and Ashraful Islam. "Colloidal quantum dot solar cells". In: *Solar Energy* 85.6 (2011), pp. 1264–1282.

[219] Xiaoliang Zhang, Carl Hägglund, Malin B Johansson, Kári Sveinbjörnsson, and Erik MJ Johansson. "Fine Tuned Nanolayered Metal/Metal Oxide Electrode for Semitransparent Colloidal Quantum Dot Solar Cells". In: *Advanced Functional Materials* 26.12 (2016), pp. 1921–1929.

[220] Xiaoliang Zhang, Carl Hägglund, and Erik MJ Johansson. "Highly efficient, transparent and stable semitransparent colloidal quantum dot solar cells: a combined numerical modeling and experimental approach". In: *Energy & Environmental Science* 10.1 (2017), pp. 216–224.

[221] Olivier Ouellette, Nadir Hossain, Brandon R Sutherland, Amirreza Kiani, F Pelayo GarciÌĄa de Arquer, Hairen Tan, Mohamed Chaker, Sjoerd Hoogland, and Edward H Sargent. "Optical Resonance Engineering for Infrared Colloidal Quantum Dot Photovoltaics". In: *ACS Energy Letters* 1.4 (2016), pp. 852–857.

[222] Xiaoliang Zhang, Giles E Eperon, Jianhua Liu, and Erik MJ Johansson. "Semitransparent quantum dot solar cell". In: *Nano Energy* 22 (2016), pp. 70–78.

[223] Shahab Akhavan, Burak Guzelturk, Vijay Kumar Sharma, and Hilmi Volkan Demir. "Large-area semi-transparent light-sensitive nanocrystal skins". In: *Optics Express* 20.23 (2012), pp. 25255–25266.

[224] Ebuka S Arinze, Gabrielle Nyirjesy, Yan Cheng, Nathan Palmquist, and Susanna M Thon. "Colloidal quantum dot materials for infrared optoelectronics". In: *Infrared Remote Sensing and Instrumentation XXIII*. Vol. 9608. International Society for Optics and Photonics. 2015, p. 960813.

[225] James Kennedy. "Particle swarm optimization". In: *Encyclopedia of machine learning*. Springer, 2011, pp. 760–766.

[226] Kalyanmoy Deb. "Multi-Objective Optimization Using Evolutionary Algorithms. John Wiley& Sons". In: *Inc., New York, NY* (2001).

[227] Thomas Smith and John Guild. "The CIE colorimetric standards and their use". In: *Transactions of the optical society* 33.3 (1931), p. 73.

[228] Andrew S Brown and Martin A Green. "Detailed balance limit for the series constrained two terminal tandem solar cell". In: *Physica E: Low-dimensional Systems and Nanostructures* 14.1-2 (2002), pp. 96–100.

[229] Xihua Wang, Ghada I Koleilat, Jiang Tang, Huan Liu, Illan J Kramer, Ratan Debnath, Lukasz Brzozowski, D Aaron R Barkhouse, Larissa Levina, Sjoerd Hoogland, et al. "Tandem colloidal quantum dot solar cells employing a graded recombination layer". In: *Nature Photonics* 5.8 (2011), p. 480.

[230] Joshua J Choi, Whitney N Wenger, Rachel S Hoffman, Yee-Fun Lim, Justin Luria, Jacek Jasieniak, John A Marohn, and Tobias Hanrath. "Solution-Processed Nanocrystal Quantum Dot Tandem Solar Cells". In: *Advanced Materials* 23.28 (2011), pp. 3144–3148.

[231] Pralay K Santra and Prashant V Kamat. "Tandem-layered quantum dot solar cells: tuning the photovoltaic response with luminescent ternary cadmium chalcogenides". In: *Journal of the American Chemical Society* 135.2 (2013), pp. 877–885.

[232] MJ Speirs, BGHM Groeneveld, L Protesescu, C Piliego, Maksym V Kovalenko, and MA Loi. "Hybrid inorganic–organic tandem solar cells for broad absorption of the solar spectrum". In: *Physical Chemistry Chemical Physics* 16.17 (2014), pp. 7672–7676.

[233] Taesoo Kim, Yangqin Gao, Hanlin Hu, Buyi Yan, Zhijun Ning, Lethy Krishnan Jagadamma, Kui Zhao, Ahmad R Kirmani, Jessica Eid, Michael M Adachi, et al. "Hybrid tandem solar cells with depleted-heterojunction quantum dot and polymer bulk heterojunction subcells". In: *Nano Energy* 17 (2015), pp. 196–205.

[234] Edward H Sargent. "Infrared photovoltaics made by solution processing". In: *Nature Photonics* 3.6 (2009), p. 325.

[235] André J Labelle, Susanna M Thon, Jin Young Kim, Xinzheng Lan, David Zhitomirsky, Kyle W Kemp, and Edward H Sargent. "Conformal fabrication of colloidal quantum dot solids for optically enhanced photovoltaics". In: *ACS nano* 9.5 (2015), pp. 5447–5453.

[236] Xinzheng Lan, Oleksandr Voznyy, Amirreza Kiani, F Pelayo García de Arquer, Abdullah Saud Abbas, Gi-Hwan Kim, Mengxia Liu, Zhenyu Yang, Grant Walters, Jixian Xu, et al. "Passivation using molecular halides increases quantum dot solar cell performance". In: *Advanced Materials* 28.2 (2016), pp. 299–304.

[237] Mengxia Liu, Oleksandr Voznyy, Randy Sabatini, F Pelayo García de Arquer, Rahim Munir, Ahmed Hesham Balawi, Xinzheng Lan, Fengjia Fan, Grant Walters, Ahmad R Kirmani, et al. "Hybrid organic–inorganic inks flatten the energy landscape in colloidal quantum dot solids". In: *Nature materials* 16.2 (2017), p. 258.

[238] Botong Qiu, Yida Lin, Ebuka S Arinze, Arlene Chiu, Lulin Li, and Susanna M Thon. "Photonic band engineering in absorbing media for spectrally selective optoelectronic films". In: *Optics Express* 26.21 (2018), pp. 26933–26945.

[239] SB Dworkin and TJ Nye. "Image processing for machine vision measurement of hot formed parts". In: *Journal of materials processing technology* 174.1-3 (2006), pp. 1–6.

[240] Drago Bračun, Gašper Škulj, and Miran Kadiš. "Spectral selective and difference imaging laser triangulation measurement system for on line measurement of large hot workpieces in precision open die forging". In: *The International Journal of Advanced Manufacturing Technology* 90.1-4 (2017), pp. 917–926.

[241] Joseph J Talghader, Anand S Gawarikar, and Ryan P Shea. "Spectral selectivity in infrared thermal detection". In: *Light: Science & Applications* 1.8 (2012), e24.

[242] James A Ratches, Richard H Vollmerhausen, and Ronald G Driggers. "Target acquisition performance modeling of infrared imaging systems: past, present, and future". In: *IEEE Sensors journal* 1.1 (2001), pp. 31–40.

[243] Hitosh Hara, Naoki Kishi, Makoto Noro, Hideto Iwaoka, and Kentaro Suzuki. *Fabry-Perot filter, wavelength-selective infrared detector and infrared gas analyzer using the filter and detector*. 2003.

[244] Peter Werle, Franz Slemr, Karl Maurer, Robert Kormann, Robert Mücke, and Bernd Jänker. "Near-and mid-infrared laser-optical sensors for gas analysis". In: *Optics and lasers in engineering* 37.2-3 (2002), pp. 101–114.

[245] Christopher S Goldenstein, R Mitchell Spearrin, Jay B Jeffries, and Ronald K Hanson. "Infrared laser-absorption sensing for combustion gases". In: *Progress in Energy and Combustion Science* 60 (2017), pp. 132–176.

[246] Alexis De Vos. "Detailed balance limit of the efficiency of tandem solar cells". In: *Journal of Physics D: Applied Physics* 13.5 (1980), p. 839.

[247] Feng Cao, Kenneth McEnaney, Gang Chen, and Zhifeng Ren. "A review of cermet-based spectrally selective solar absorbers". In: *Energy & Environmental Science* 7.5 (2014), pp. 1615–1627.

[248] DM Trotter and AJ Sievers. "Spectral selectivity of high-temperature solar absorbers". In: *Applied optics* 19.5 (1980), pp. 711–728.

[249] Hoyeon Kim, Hui-Seon Kim, Jaewon Ha, Nam-Gyu Park, and Seunghyup Yoo. "Empowering semi-transparent solar cells with thermal-mirror functionality". In: *Advanced Energy Materials* 6.14 (2016), p. 1502466.

[250] E Radziemska. "The effect of temperature on the power drop in crystalline silicon solar cells". In: *Renewable energy* 28.1 (2003), pp. 1–12.

[251] Adham Makki, Siddig Omer, and Hisham Sabir. "Advancements in hybrid photovoltaic systems for enhanced solar cells performance". In: *Renewable and sustainable energy reviews* 41 (2015), pp. 658–684.

[252] BJ Huang, PE Yang, YP Lin, BY Lin, HJ Chen, RC Lai, and JS Cheng. "Solar cell junction temperature measurement of PV module". In: *Solar Energy* 85.2 (2011), pp. 388–392.

[253] Kevin A Bush, Axel F Palmstrom, J Yu Zhengshan, Mathieu Boccard, Rongrong Cheacharoen, Jonathan P Mailoa, David P McMeekin, Robert LZ Hoye, Colin D Bailie, Tomas Leijtens, et al. "23.6%-efficient monolithic perovskite/silicon tandem solar cells with improved stability". In: *Nature Energy* 2.4 (2017), p. 17009.

[254] Martin A. Green, Yoshihiro Hishikawa, Ewan D. Dunlop, Dean H. Levi, Jochen Hohl-Ebinger, and Anita W.Y. Ho-Baillie. "Solar cell efficiency tables (version 51)". In: *Progress in Photovoltaics: Research and Applications* 26.1 (), pp. 3–12.

[255] JC Knight, TA Birks, P St J Russell, and DM Atkin. "All-silica single-mode optical fiber with photonic crystal cladding". In: *Optics letters* 21.19 (1996), pp. 1547–1549.

[256] Attila Mekis, JC Chen, I Kurland, Shanhui Fan, Pierre R Villeneuve, and JD Joannopoulos. "High transmission through sharp bends in photonic crystal waveguides". In: *Physical Review Letters* 77.18 (1996), p. 3787.

[257] Philip St J Russell. "Photonic-crystal fibers". In: *Journal of lightwave technology* 24.12 (2006), pp. 4729–4749.

[258] Eiichi Kuramochi, Kengo Nozaki, Akihiko Shinya, Koji Takeda, Tomonari Sato, Shinji Matsuo, Hideaki Taniyama, Hisashi Sumikura, and Masaya Notomi. "Large-scale integration of wavelength-addressable all-optical memories on a photonic crystal chip". In: *Nature Photonics* 8.6 (2014), p. 474.

[259] MR Sprague, PS Michelberger, TFM Champion, DG England, J Nunn, X-M Jin, WS Kolthammer, A Abdolvand, P St J Russell, and IA Walmsley. "Broadband single-photon-level memory in a hollow-core photonic crystal fibre". In: *Nature Photonics* 8.4 (2014), p. 287.

[260] Yurii A Vlasov, Martin O'boyle, Hendrik F Hamann, and Sharee J McNab. "Active control of slow light on a chip with photonic crystal waveguides". In: *Nature* 438.7064 (2005), p. 65.

[261] Thomas Volz, Andreas Reinhard, Martin Winger, Antonio Badolato, Kevin J Hennessy, Evelyn L Hu, and Ataç Imamoğlu. "Ultrafast all-optical switching by single photons". In: *Nature Photonics* 6.9 (2012), p. 605.

[262] John D Joannopoulos, Steven G Johnson, Joshua N Winn, and Robert D Meade. *Photonic crystals: molding the flow of light*. Princeton university press, 2011.

[263] S Strauf, K Hennessy, MT Rakher, Y-S Choi, A Badolato, LC Andreani, EL Hu, PM Petroff, and D Bouwmeester. "Self-tuned quantum dot gain in photonic crystal lasers". In: *Physical review letters* 96.12 (2006), p. 127404.

[264] Hong-Gyu Park, Se-Heon Kim, Soon-Hong Kwon, Young-Gu Ju, Jin-Kyu Yang, Jong-Hwa Baek, Sung-Bock Kim, and Yong-Hee Lee. "Electrically driven single-cell photonic crystal laser". In: *Science* 305.5689 (2004), pp. 1444–1447.

[265] Peter Bermel, Chiyan Luo, Lirong Zeng, Lionel C Kimerling, and John D Joannopoulos. "Improving thin-film crystalline silicon solar cell efficiencies with photonic crystals". In: *Optics express* 15.25 (2007), pp. 16986–17000.

[266] Antonio Badolato, Kevin Hennessy, Mete Atatüre, Jan Dreiser, Evelyn Hu, Pierre M Petroff, and Atac Imamoğlu. "Deterministic coupling of single quantum dots to single nanocavity modes". In: *Science* 308.5725 (2005), pp. 1158–1161.

[267] Andrew R Parker and Helen E Townley. "Biomimetics of photonic nanostructures". In: *Nature nanotechnology* 2.6 (2007), p. 347.

[268] Vinodkumar Saranathan, Chinedum O Osuji, Simon GJ Mochrie, Heeso Noh, Suresh Narayanan, Alec Sandy, Eric R Dufresne, and Richard O Prum. "Structure, function, and self-assembly of single network gyroid (I4132) photonic crystals in butterfly wing scales". In: *Proceedings of the National Academy of Sciences* 107.26 (2010), pp. 11676–11681.

[269] Jeremy W Galusha, Lauren R Richey, John S Gardner, Jennifer N Cha, and Michael H Bartl. "Discovery of a diamond-based photonic crystal structure in beetle scales". In: *Physical Review E* 77.5 (2008), p. 050904.

[270] John D Joannopoulos, Pierre R Villeneuve, and Shanhui Fan. "Photonic crystals: putting a new twist on light". In: *Nature* 386.6621 (1997), p. 143.

[271] Zhenlin Wang, Che Ting Chan, Weiyi Zhang, Naiben Ming, and Ping Sheng. "Three-dimensional self-assembly of metal nanoparticles: Possible photonic crystal with a complete gap below the plasma frequency". In: *Physical Review B* 64.11 (2001), p. 113108.

[272] Ken Xingze Wang, Zongfu Yu, Victor Liu, Aaswath Raman, Yi Cui, and Shanhui Fan. "Light trapping in photonic crystals". In: *Energy & Environmental Science* 7.8 (2014), pp. 2725–2738.

[273] Alongkarn Chutinan, Nazir P Kherani, and Stefan Zukotynski. "High-efficiency photonic crystal solar cell architecture". In: *Optics Express* 17.11 (2009), pp. 8871–8878.

[274] Alongkarn Chutinan and Sajeev John. "Light trapping and absorption optimization in certain thin-film photonic crystal architectures". In: *Physical Review A* 78.2 (2008), p. 023825.

[275] Robert B Withrow and Leonard Price. "Filters for the isolation of narrow regions in the visible and near-visible spectrum". In: *Plant physiology* 28.1 (1953), p. 105.

[276] Hao Wang and Liping Wang. "Perfect selective metamaterial solar absorbers". In: *Optics express* 21.106 (2013), A1078–A1093.

[277] Amaresh Mishra and Peter Bäuerle. "Small molecule organic semiconductors on the move: promises for future solar energy technology". In: *Angewandte Chemie International Edition* 51.9 (2012), pp. 2020–2067.

[278] KF Renk and L Genzel. "Interference filters and Fabry-Perot interferometers for the far infrared". In: *Applied Optics* 1.5 (1962), pp. 643–648.

[279] Lifeng Li. "New formulation of the Fourier modal method for crossed surface-relief gratings". In: *JOSA A* 14.10 (1997), pp. 2758–2767.

[280] Lifeng Li. "Formulation and comparison of two recursive matrix algorithms for modeling layered diffraction gratings". In: *JOSA A* 13.5 (1996), pp. 1024–1035.

[281] Lifeng Li. "Use of Fourier series in the analysis of discontinuous periodic structures". In: *JOSA A* 13.9 (1996), pp. 1870–1876.

[282] Valerio Lucarini, Jarkko J Saarinen, Kai-Erik Peiponen, and Erik M Vartiainen. *Kramers-Kronig relations in optical materials research*. Vol. 110. Springer Science & Business Media, 2005.

[283] Igor A Sukhoivanov and Igor V Guryev. *Photonic crystals: physics and practical modeling*. Vol. 152. Springer, 2009.

[284] Edward D Palik. "-Gallium Arsenide (GaAs)". In: *Handbook of optical constants of solids*. Elsevier, 1997, pp. 429–443.

[285] Hermann A Haus. "Waves and Fields in Optoelectronics Prentice-Hall". In: *Inc. Englewood Cliffs, New Jersey* (1984).

[286] Shanhui Fan, Wonjoo Suh, and John D Joannopoulos. "Temporal coupled-mode theory for the Fano resonance in optical resonators". In: *JOSA A* 20.3 (2003), pp. 569–572.

[287] Wonjoo Suh, Zheng Wang, and Shanhui Fan. "Temporal coupled-mode theory and the presence of non-orthogonal modes in lossless multimode cavities". In: *IEEE Journal of Quantum Electronics* 40.10 (2004), pp. 1511–1518.

[288] Shanhui Fan and JD Joannopoulos. "Analysis of guided resonances in photonic crystal slabs". In: *Physical Review B* 65.23 (2002), p. 235112.

[289] Gerasimos Konstantatos, Ian Howard, Armin Fischer, Sjoerd Hoogland, Jason Clifford, Ethan Klem, Larissa Levina, and Edward H Sargent. "Ultrasensitive solution-cast quantum dot photodetectors". In: *Nature* 442.7099 (2006), p. 180.

[290] Xiwen Gong, Zhenyu Yang, Grant Walters, Riccardo Comin, Zhijun Ning, Eric Beauregard, Valerio Adinolfi, Oleksandr Voznyy, and Edward H Sargent. "Highly efficient quantum dot near-infrared light-emitting diodes". In: *Nature Photonics* 10.4 (2016), p. 253.

[291] Michael M Adachi, André J Labelle, Susanna M Thon, Xinzheng Lan, Sjoerd Hoogland, and Edward H Sargent. “Broadband solar absorption enhancement via periodic nanostructuring of electrodes”. In: *Scientific reports* 3 (2013), p. 2928.

[292] Chin Li Cheung, RJ Nikolić, CE Reinhardt, and TF Wang. “Fabrication of nanopillars by nanosphere lithography”. In: *Nanotechnology* 17.5 (2006), p. 1339.

[293] Alexander H Ip, Susanna M Thon, Sjoerd Hoogland, Oleksandr Voznyy, David Zhitomirsky, Ratan Debnath, Larissa Levina, Lisa R Rollny, Graham H Carey, Armin Fischer, et al. “Hybrid passivated colloidal quantum dot solids”. In: *Nature nanotechnology* 7.9 (2012), p. 577.

Chapter 4

Nanomaterials manufacturing for optoelectronic devices with novel functions

4.1 Solution-processed near-infrared transparent LEDs

4.1.1 Background and Motivation

Although incandescent bulbs and fluorescent lamps are still in use today, light emitting diode (LED)-based white light sources are much more energy-efficient, and therefore represent a revolution in ambient lighting [1]. What is more, thanks to the development of organic LEDs (OLEDs), display technology has experienced a huge leap in the past decade, and the high-end display market is now dominated by LEDs [2, 3]. Beyond lighting and display, LEDs also serve as the essential light sources in all kinds systems and instruments, such as optical communication systems [4, 5], wearable devices [6, 7]and medical instruments [8, 9]. Innovations in these areas have also led to many challenges for the development of novel LEDs.

There is an urgent need for transparent flexible LED devices that emit in the invisible near-infrared (NIR) regime for many applications such as eye-tracking, biomedical imaging, motion-capture and security monitoring. Commercially available LED devices made out of traditional crystalline semiconductors or organic conductors, have difficulties in fulfilling such requirements. OLEDs are made of nanomaterials and can be transparent and lightweight, as well as flexible, and have had huge success in visible light applications, but NIR OLEDs are scarce due to limited materials choices for that emission range. Although traditional NIR LEDs can be made from specific crystalline semiconductor compositions, such devices suffer from opacity, rigidity and high costs due to their energy-intensive materials processing requirements.

Ever since their invention [10], quantum-dot-based LEDs (QLEDs) have drawn significant interest due to their narrow emission spectral-bandwidth and ease of tuning the emission wavelength via control of the QD size [11, 12]. Thanks to multilateral efforts based on advances in the fundamental understanding of the device physics as well as advanced engineering of materials and device architectures, the performance of QLEDs in terms of brightness, quantum efficiency and stability has improved rapidly [13, 14, 15, 16, 17, 18]. Despite this progress, most of the work on QLEDs has focused on the visible range for display technology, or the NIR beyond 1000 nm that poses challenges on the detection side of an integrated system. Although PbS CQD-based QLEDs emitting in the infrared have been made before, we developed devices that are novel in that they can be integrated into a flexible transparent membrane and optimized for both transparency and an NIR

emission wavelength that is short enough to be detectable by inexpensive silicon-based photodetectors.

4.1.2 Transparent QLED Applications and Device Architectures

Current eye-tracking goggles for virtual reality (VR) applications or human behavior studies are relatively bulky and have an appearance that deviates significantly from normal glasses, which consequently affects the natural behavior of human eyes and the subject's comfort level. Therefore, reducing the goggle weight so that its appearance can become more similar to normal glasses is a current industry need. Our transparent LED membrane is designed to allow visible light to be transmitted through the goggles for display purposes while emitting invisible infrared (> 800 nm in wavelength) light to illuminate the eye. The envisioned eye tracking solution uses the optical augmentation effect at specific light wavelengths to provide high speed tracking of the eye with minimal light intensity.

Another example application for our transparent LED membrane is as part of a motion-capture system for the entertainment industry. Currently, motion-capture for animation requires actors to wear bulky motion-capture suits that are wired up to record their movements, and this is done in highly customized rooms. There is tremendous interest in new technology that will enable the acting to take place in realistic surroundings with the actors wearing normal clothing. The transparent light emitting membrane we propose can be easily integrated into the actor's clothing and provide illumination of specific locations on the person's body. The LEDs can be pulsed at different

frequencies to provide location-specific labelling. A high-speed imaging sensor can then track the body movements with high fidelity. Furthermore, if the illumination is synchronized with the image capture, this proposed solution could also provide 3D (depth) information, which is the ultimate objective for this industry.

Other target applications of our technology include: medical probes coated with our flexible transparent light-emitting membrane to be used as a local imaging light sources. Infrared (invisible) security monitoring systems could be coated with our flexible transparent light-emitting membrane on existing camera surfaces to make the systems easily camouflaged and less vulnerable. Photobiomodulation therapy systems in which infrared illumination generated by our flexible transparent LEDs could be used to treat a variety of retinal conditions including age-related macular degeneration, retinopathy of prematurity, diabetic retinopathy, Leber's hereditary optic neuropathy, amblyopia, methanol-induced retinal damage, and possibly other conditions [19].

The typical device structure of a QLED is similar to those of traditional OLEDs, which is a multi-layer thin film structure consisting of a bottom transparent electrode, electron injection/hole blocking layer, emission layer, hole injection/electron blocking layer and top electrode. In order to produce flexible devices, we construct our QLEDs on flexible substrates such as polyethylene terephthalate (PET) films and use solution-processed nanomaterials for all of the layers. We replace the traditional bottom electrode made of crystalline transparent conductive oxides (TCOs) and top metal electrodes

with Ag nanowire (NW)-based electrodes for enabling transparency of the device. The electron injection/hole blocking layer is made of ZnO or Mg-doped ZnO nanocrystals [20] while the emission layer is made of PbS CQDs with carefully controlled sizes and ligand exchanges enabling them to be made into solid films. There are a few organic polymer materials that can be used for the hole injection/electron blocking layers including 4-bis(carbazole-9-yl)biphenyl (CBP) [18] and poly(9-vinlycarbazole) (PVK) [21] or poly(9,9'-dioctylfluorene) (F8) [17] or the hole injection layer can be emitted from the device. The device structure is shown in Figure 4.1.

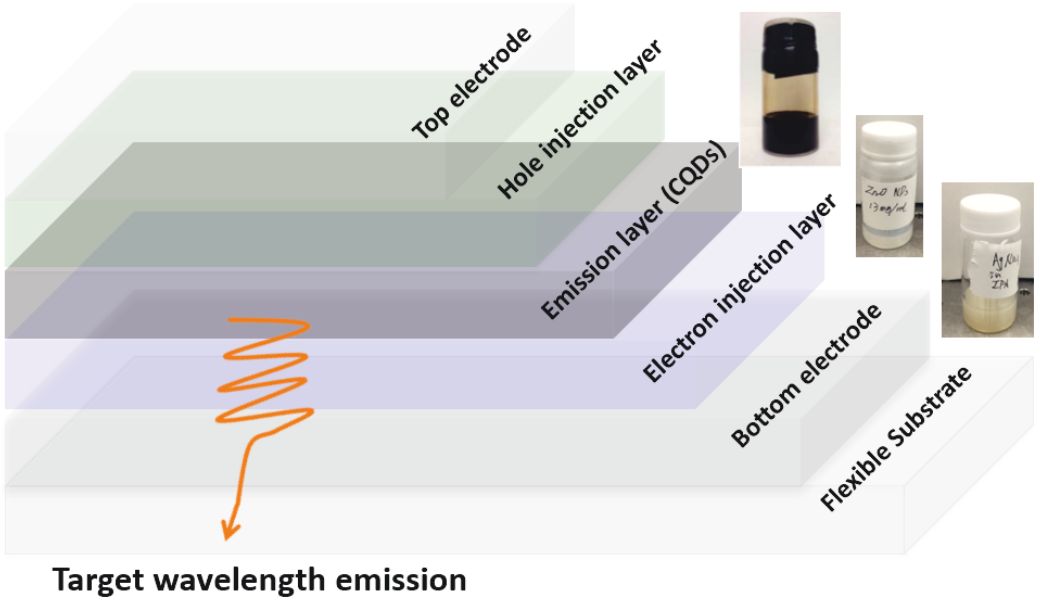

Figure 4.1: Device structure of solution-processed near-infrared QLEDs : from bottom to top: flexible substrate, bottom transparent electrode, electron injection/hole blocking layer, emission layer, hole injection/electron blocking layer and top electrode. The insets are photographs of solutions of Ag nanowires, ZnO nanoparticles, and PbS CQD inks used for the transparent electrode layers, electron injection/hole blocking layer, and emission layer, respectively. The arrow indicates the emission from radiative recombination processes within the active layer.

Ag nanowire-based electrodes have a good transparency-conductivity trade-off, allowing substantially all of the visible light emitted from the PbS CQD layer to be transmitted through the transparent substrate. Efficient radiative recombination does not require a thick PbS CQD film, and therefore the device can be made highly transparent with a tens-of-nanometers thick emission layer . We also apply the optical engineering method we developed for multi-layer thin film photovoltaic structures [22] to optimize transparency without sacrificing QLED performance.

4.1.3 Experimental Results

The Ag nanowire-based composite electrode is made by spin-casting a solution of Ag NWs on thoroughly cleaned substrates followed by spin-casting of indium tin oxide (ITO) nanoparticles. Both the Ag nanowires and ITO nanoparticles are in isopropanol and purchased from Sigma-Aldrich. The Ag NWs are approximately 40 microns in length and have diameters of approximately 70 nm, and the ITO nanoparticles are specified as < 100 nm in diameter using dynamic light scattering (DLS). It is important that these two spin-casting steps are performed in rapid succession to ensure good infiltration of the ITO nanoparticles into the Ag NW network to mitigate surface roughness and improve the conductivity. The transmittance spectrum of a Ag nanowire composite electrode on a glass substrate is shown in Figure 4.2, and the insets are photographs of the electrodes on glass and PET substrates.

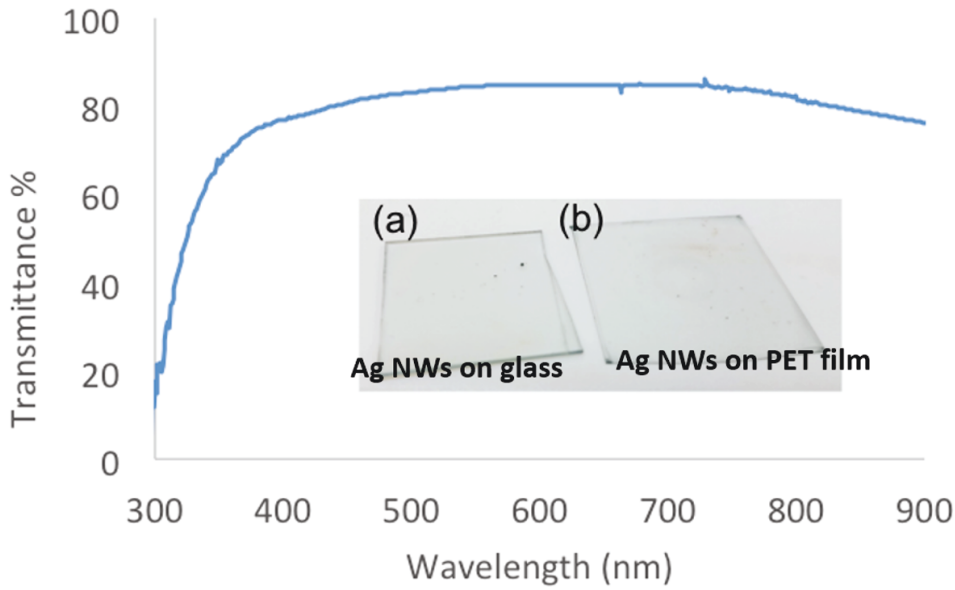

Figure 4.2: Transmittance of an Ag NW-based composite electrode : the Ag NW composite electrode is deposited on a glass substrate and has a sheet resistance of 34 Ω/□. Inset: (a) Photograph of an Ag NW-based composite electrode on glass. (b) Photograph of an Ag NW based composite electrode on PET

The ZnO nanocrystals are synthesized according to published methods [23] and spin-cast onto substrates coated with the transparent electrode. Our target application and the responsivity of silicon-based photodetectors require the emission wavelength to fall within the 800-1000 nm range. PbS CQD solutions meeting this requirement are synthesized by modifying previously published methods [24]. Due to the large Stokes shift that is present in these materials [25], very small PbS CQDs with first exciton peak wavelengths smaller than 800 nm in absorption are required, which are produced by using a low injection temperature for the sulfide precursor and applying an ice bath immediately after injection to quench the reaction [26]. 1,6-Hexanedithiol in methanol was introduced during spin-casting of the PbS CQDs in a solid-state ligand exchange followed by two methanol washing steps. The emission

layer thickness is about 20-40 nm and can be empirically tuned by controlling the concentration of the PbS CQD solution and spin-casting parameters (speed and acceleration). The organic polymer materials used for the hole injection/electron blocking layer are also be deposited by spin-casting. The top metal electrode is deposited using electron beam evaporation using a shadow mask to define the active device area. The transparent Ag nanowire-based composite top electrode is deposited in similar fashion as the bottom transparent electrode.

Electroluminescence (EL) spectra of the QLEDs are measured using our Ocean Optics spectrometer as shown in Figure 4.3a and the responsivity of a Thorlabs PDB210A Si photodetector is shown in Figure 4.3b. The close alignment of the peaks of the EL spectrum and Si photodetector responsivity show that the emission of our QLEDs can be easily detected by Si photodetectors, which is promising for easy integration of our QLEDs into their target applications. The inset of Figure 4.3a is a photograph of a device fabricated in our lab. The QLED array, consisting of several 0.5 cm^2 circles is created using a shadow mask during electron-beam evaporation of the metal top electrodes . The area in between the metal top electrodes shows high transparency. The transparency of the structure can be further optimized by reducing the active layer thickness and combining our previously developed optical engineering method into the QLED design and optimization [22].

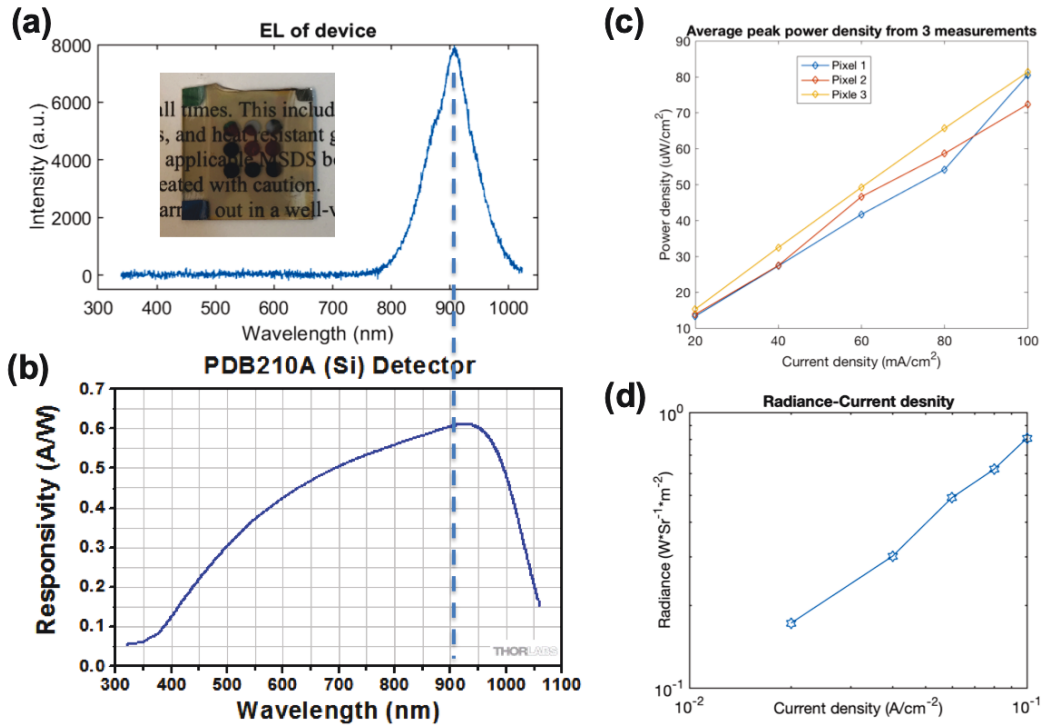

Figure 4.3: QLED characterization : (a) The EL spectrum of the QLED peaks around 900 nm, close to the peak (b) responsivity of a Thorlabs Si photodetector. Inset of (a) is a photograph of a typical QLED array with 9 pixels (pixel area is defined by the metal top electrode) on one substrate. (c) Power density versus current density for 3 different QLED pixels on the same substrate. (d) Radiance versus current density for a selected QLED pixel.

A Thorlabs power meter with a 9.5mm diameter circular aperture placed 5mm away from the QLED pixel is used to measure the emitted power from the QLED, and the dependence of the power density on the current density is plotted in Figure 4.3c. The linear relationship between the power density and current density indicates that the QLED does not show significant efficiency droop within this range of the current density. The radiance from the QLED is also calculated considering the geometry of the power measurement set-up and plotted versus current density in Figure 4.3d, whose performance is

comparable to the state-of-the-art performance of near-infrared PbS QLEDs emitting at other wavelengths [27]. Although through power tracing and switching on/off we find that our QLED is stable and switchable, when turned on for more than a few minutes, depending on the current density, the power output will drop slowly and finally diminish to zero, indicating irreversible damage due to excessive heating.

4.1.4 Summary and Outlook

In summary, we demonstrated a PbS CQD-based QLED with an emission wavelength near 900 nm that can be easily detected by silicon photodetector technology. We also developed a Ag NW-based composite electrode that can be used as the transparent contact material for QLEDs and other transparent devices. All of the QLED layers can be made from nanomaterials using solution-processed fabrication methods. The only layer that absorbs in the visible region is the ultra-thin QD emission layer; therefore, our device has great potential for use as a flexible transparent light-emitting diode membrane array. A number of target applications for this technology including VR goggles, motion-capture suits and medical probes were also discussed.

Future efforts towards practical applications of our QLEDs will have two components: device engineering and system integration. On the device side, future work will involve quantifying device performance in more detail and optimizing the device structure and materials properties to improve the efficiency of the QLEDs. On the system integration side, heat management of the devices, out-coupling optics, frequency and synchronization control, and

signal detection of the system are all of great importance. We will continue to collaborate with experts in those areas to develop a full system prototype.

4.2 Completely Spray-Cast Flexible Transparent CQD Solar Cells

4.2.1 Introduction

Even though the costs of silicon-based solar cells have continued to decline, their installations are limited to robust modern rooftops or require large land areas due to the rigid and heavy nature of their modules [28]. If flexible transparent solar cells could be made, they could expand the applications of solar cells to areas such as wearable devices, automobile skins, windows and exterior surfaces of existing urban infrastructures [29, 30]. Colloidal quantum dots (CQDs) are promising for building flexible transparent solar cells due to their lightweight nature, size-dependent band gap tunability and processing flexibility [31]. Power conversion efficiencies (PCEs) of CQD solar cells have been climbing rapidly [32, 33, 34]; however, the best-performing devices are still dependent on high-temperature-processed transparent conductive oxides (TCOs) and use lab-based batch-level processing methods such as spin-casting and dip-coating, which limit the flexibility and scalable fabrication of CQD solar cells.

Spray casting is a well-known industrial-scale manufacturing method and is of great interest for scalable solar cell manufacturing. Spray-casting can save on material costs due to its high and possibly 100% utilization rate of the starting ink material compared with traditional spin-casting processes that

waste a large fraction of the starting ink. In addition, spray-casting processes do not require high-temperature and high-vacuum conditions, which saves on processing costs. Lastly, spray-casting can be both scalable and portable and can be applied onto almost any surface, making it a viable way to expand the applications of CQD solar cells.

Even though spray-cast CQD solar cells with comparable performance to their batch-processed counterparts have been demonstrated [35], only the absorbing CQD layer was spray-cast in these studies, while the electrodes and other device layers still relied on batch-processed fabrication or high vacuum deposition methods, which not only add to the complexity that limits the scale-up potential of the device manufacturing but also limit the surfaces that the devices can be coated on to traditional wafer-based substrates. To eliminate the intensive processing requirements for the TCOs and metal electrodes, we developed a room-temperature spray-cast Ag nanowire transparent electrode, which also allows for good mechanical flexibility. With solution-based ZnO nanocrystals comprising the electron transport layers and solution-phase ligand-exchanged CQDs inks comprising the active layers, our ultimate goal is to demonstrate a CQD solar cell in which all device layers are spray-cast with minimal complexity and demonstrate flexible transparent devices on different kinds of flexible transparent substrates.

4.2.2 Results and Discussion

Most high-performing CQD solar cells employ ZnO nanocrystals [34] rather than crystalline ZnO or TiO_2 [22] as the electron transport layer, which is

convenient for building flexible CQD solar cells. With PbS CQD-based thin films acting as both the absorbing layer and hole transport layer, the only problematic device layers for building flexible transparent CQD solar cells are the brittle TCO bottom electrode and opaque metal top electrode, which must be replaced with flexible transparent electrodes. Our solution for this problem is a room-temperature spray-cast Ag NW electrode. The complete device structure is shown in Figure 4.4.

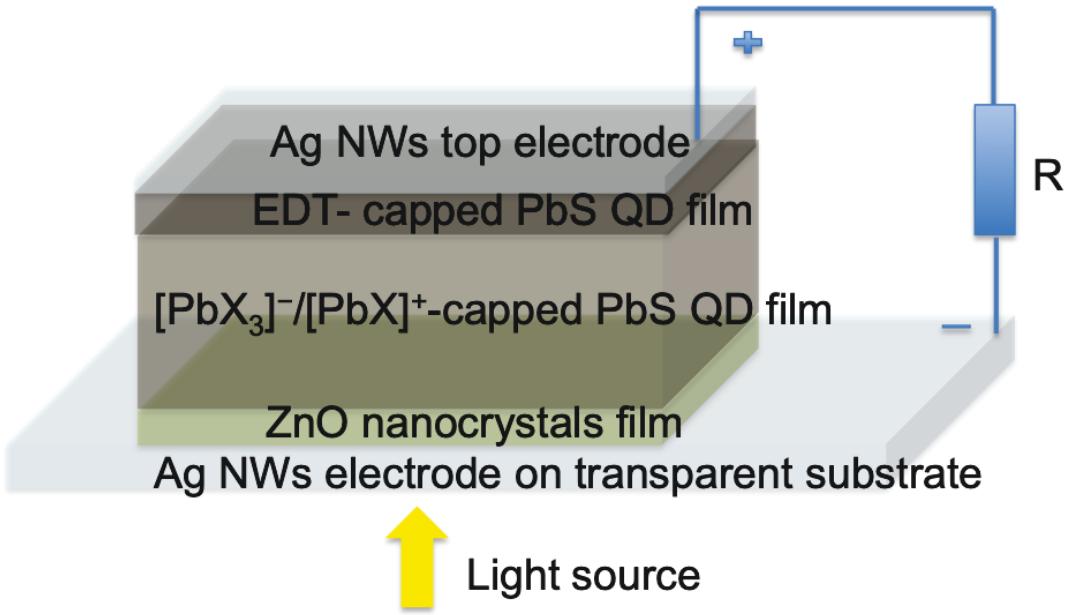

Figure 4.4: Device structure of a spray-cast flexible transparent CQD solar cell : from bottom to top: Ag NW-based bottom transparent electrode on a substrate; ZnO nanocrystal-based electron transport layer; $[PbX_3]^-/[PbX]^+$ -capped PbS QD absorbing layer; 1,2-Ethanedithiol (EDT)-capped PbS QD hole transport layer; Ag NW-based top transparent electrode. The arrow indicates the direction of the light source, and the load powered by this CQD solar cell is represented by a resistor with resistance R.

The Ag NW-based electrode is spray-cast onto a well-cleaned substrate using a Ag-N-in-isopropanol ink purchased from Sigma-Aldrich. The ZnO

nanocrystals are synthesized in our lab by modifying a previously published methods [23] and finally dispersed in methanol for spray-casting. PbS CQDs capped with oleic acid ligands in octane are synthesized by modifying previously published methods [24]. A solution-phase ligand exchange is performed using PbI_2, $PbBr_2$ and ammonium acetate in dimethylformamide (DMF) to get $[PbX_3]^-/[PbX]^+$ -capped PbS CQDs, and the CQDs are dispersed in a mixture of butylamine and DMF for spray-casting the $[PbX_3]^-/[PbX]^+$ -capped PbS QD absorbing layer. A thin layer of oleic-acid capped PbS CQDs is sprayed on top of the absorbing layer, followed by spraying of 1,2-Ethanedithiol (EDT) in acetonitrile to perform a solid-state ligand exchange. This is followed by a pure acetonitrile spray step to wash the film and remove the oleic acid ligands, forming the EDT-capped PbS QD hole transport layer.

We designed and built a semi-automated spray-casting instrument that uses computer-controlled on/off pneumatic valves to control the spray nozzles as shown in Figure 4.5. Deposition conditions for different materials, including the concentration of the solution, the deposition and drying times, the substrate-to-nozzle distance, and the air pressure are optimized individually for each device layer to get both good nano- and micro-scale film morphologies.

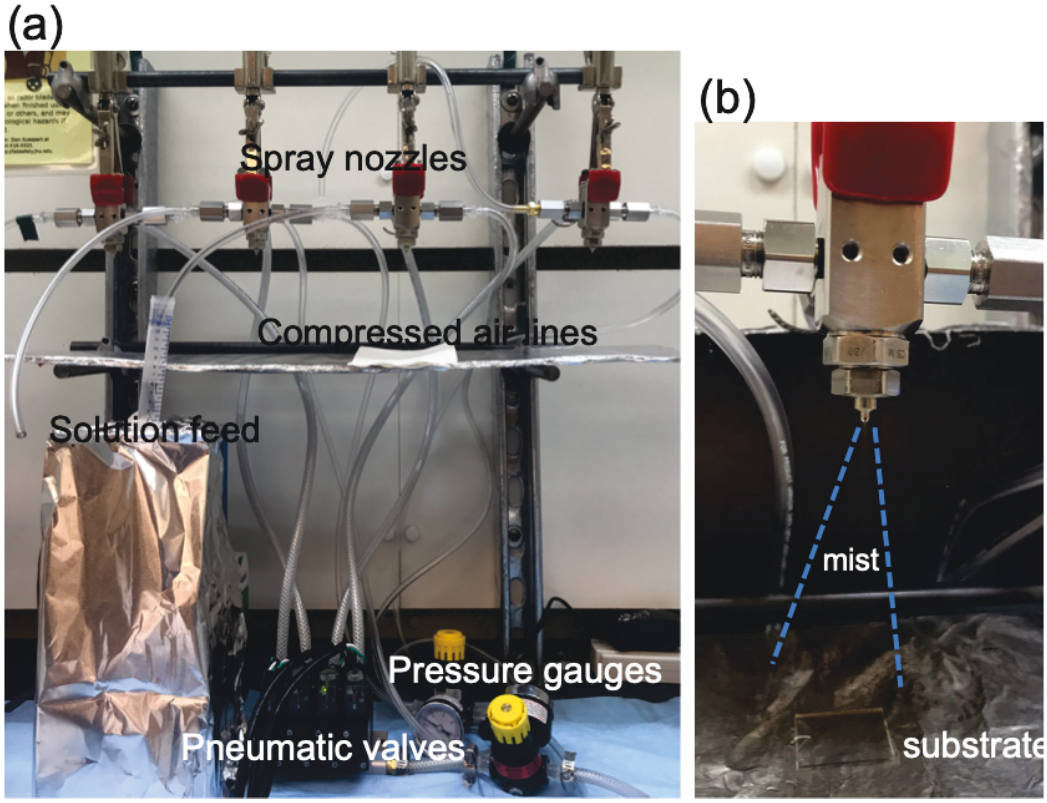

Figure 4.5: Photograph of our experimental set-up for spray-casting : (a) Our home-built semi-automated computer-controlled spray-casting system. (b) Close-up action shot of Ag NWs being sprayed onto a glass substrate.

For the spray-cast Ag NW electrode, the conductivity is generally determined by the degree of interconnection between individual Ag NWs that form the Ag NW network. Even though there is a transparency/conductivity trade-off inherent in the Ag NW network, generally, longer Ag NW constituents lead to better conductivity and thinner Ag NW constituents improve transparency []. We use a commercial Ag NW solution (Sigma-Aldrich, 5 mg/ml, 70 nm ($\pm$10 nm) diameter, 40 μm ($\pm$5 μm) length in isopropanol) as our source. Our optimized spray-casting procedure that produces Ag NW electrodes with

acceptable transparency and conductivity uses an Ag NW solution concentration of 0.5 mg/ml and a total spray duration of 6.5 minutes (consisting of six 1-minute-spray/1-minute-dry cycles). We place our 1-inch-square glass substrates 8 cm away from the spray nozzle.

The sheet resistance of the transparent electrode is measured using our home-built four-point-probe system, and transmittance is measured using a Cary5000 UV-Vis-NIR spectrophotometer. A comparison between commercial indium tin oxide (ITO), fluorine doped tin oxide (FTO) and our best-performing spray-cast Ag NW electrode on glass substrates are shown in Figure 4.6, and the inset shows a scanning electron microscope (SEM) image of the Ag NW network.

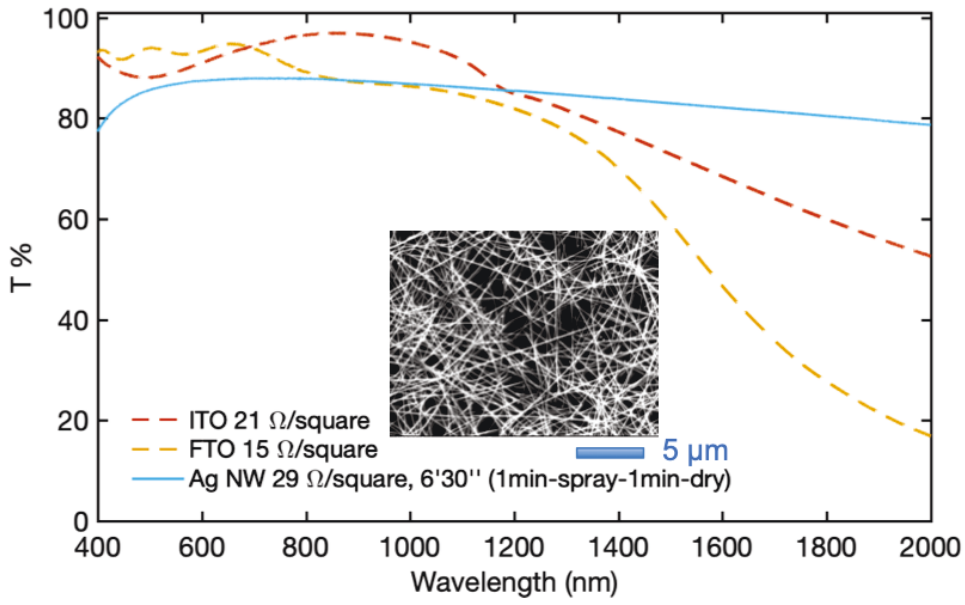

Figure 4.6: Performance comparison of different transparent electrodes : transmission curves for the best-performing spray-cast Ag NW electrode and transparent conductive oxide control samples, with sheet-resistances listed in the legend. The inset is a SEM image of the Ag NW film on glass.

With $\approx$ 85% average transmittance across the visible range, our best performing spray-cast Ag NW electrode has a sheet resistance of 29 $\Omega/\square$, which is comparable to the commercial TCO electrodes. One noticeable feature of our spray-cast Ag NW electrode is its significantly higher near-infrared transmittance compared to the commercial TCO electrodes. This property is crucial for PbS CQD solar cells because one major advantage of PbS CQD solar cells is their infrared solar energy harvesting ability [36, 32].

We have also demonstrated successful integration of spray-cast ZnO electron transport layers in PbS CQD solar cells. We identified 2 mg/ml as the optimum concentration for the ZnO nanocrystals in methanol for our current spray-casting process. We applied a continuous spray for 10 minutes to deposit ZnO nanocrystals onto ITO-coated glass, which resulted in a thin film with a mean thickness of approximately 100 nm, similar to our conventional spin-cast ZnO layer thickness. With the rest of the device layers made using conventional fabrication techniques, we produced a PbS CQD solar cell with a spin-cast ZnO electron transport layer that had a PCE of 5.4%. The current density - voltage (J-V) curve and performance summary of this device are shown in Figure 4.7.

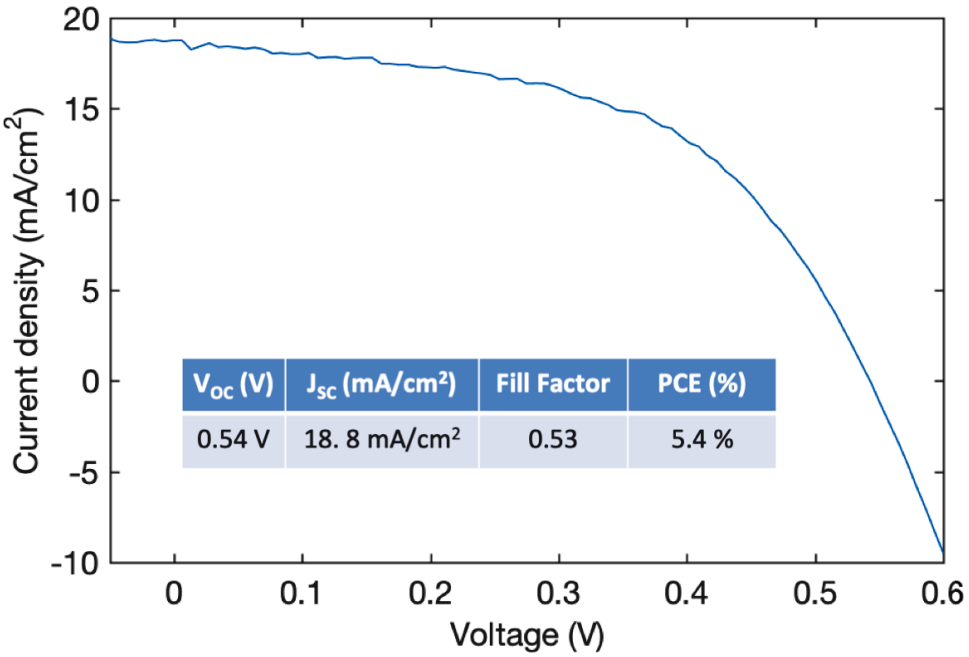

Figure 4.7: J-V curve of PbS soalr cell with spray-cast ZnO : current density-voltage curve under simulated solar illumination for a PbS CQD solar cell with a spray-cast ZnO electron transport layer on an ITO-coated glass substrate.

Although our spray-cast Ag NW electrode has a transparency/conductivity trade-off that is comparable to that of commercial TCO electrodes, the large surface roughness currently hinders the performance of this electrode in devices. Future work towards our goal of building a fully spray-cast PbS CQD solar cell will focus on strategies to reduce the surface roughness of the spray-cast Ag NW electrode and optimize deposition conditions for the rest of the cell layers.

4.2.3 Summary and outlook

In summary, we have successfully built a semi-automated spray-casting system capable of depositing different optoelectronically-relevant inks. We

demonstrated a spray-cast Ag NW electrode on glass substrates showing comparable performance to commercial TCO electrodes with superior near-infrared transparency, which is an advantage for PbS CQD solar cells that absorbs infrared photons. In addition, we demonstrated a PbS CQD solar cell with a spray-cast ZnO electron transport layer and a PCE of 5.4%.

Next we will pursue strategies such as inserting an encapsulating conducting layer of poly(3,4-ethylenedioxythiophene) polystyrene sulfonate (PEDOT:PSS) or heating the substrates during ZnO spray-casting to enable better coverage of the ZnO onto and into the Ag NW network to ameliorate the surface roughness issues associated with the Ag NW electrode. We will also optimize the deposition and ligand exchange processes for the rest of the layers of the PbS CQD solar cell to demonstrate a fully spray-cast PbS CQD solar cell as a demonstration of a scalable and portable next-generation solar cell manufacturing process.

References

[1] Siddha Pimputkar, James S Speck, Steven P DenBaars, and Shuji Nakamura. “Prospects for LED lighting”. In: *Nature photonics* 3.4 (2009), p. 180.

[2] Takuya Komoda, Hisahiro Sasabe, and Junji Kido. “Current Status of OLED Material and Process Technologies for Display and Lighting”. In: *2018 25th International Workshop on Active-Matrix Flatpanel Displays and Devices (AM-FPD)*. IEEE. 2018, pp. 1–4.

[3] Tingzhu Wu, Chin-Wei Sher, Yue Lin, Chun-Fu Lee, Shijie Liang, Yijun Lu, Sung-Wen Huang Chen, Weijie Guo, Hao-Chung Kuo, and Zhong Chen. “Mini-LED and micro-LED: Promising candidates for the next generation display technology”. In: *Applied Sciences* 8.9 (2018), p. 1557.

[4] Toshihiko Komine and Masao Nakagawa. “Fundamental analysis for visible-light communication system using LED lights”. In: *IEEE transactions on Consumer Electronics* 50.1 (2004), pp. 100–107.

[5] G Cossu, AM Khalid, P Choudhury, R Corsini, and E Ciaramella. “3.4 Gbit/s visible optical wireless transmission based on RGB LED”. In: *Optics express* 20.26 (2012), B501–B506.

[6] Chul Woo Cho, Ji Woo Lee, Kwang Yong Shin, Eui Chul Lee, Kang Ryoung Park, Heekyung Lee, and Jihun Cha. “Gaze Detection by Wearable Eye-Tracking and NIR LED-Based Head-Tracking Device Based on SVR”. In: *ETRI Journal* 34.4 (2012), pp. 542–552.

[7] Andrea Censi, Jonas Strubel, Christian Brandli, Tobi Delbruck, and Davide Scaramuzza. “Low-latency localization by Active LED Markers tracking using a Dynamic Vision Sensor”. In: *2013 IEEE/RSJ International Conference on Intelligent Robots and Systems*. IEEE. 2013, pp. 891–898.

[8] Jyoti Yadav, Asha Rani, Vijander Singh, and Bhaskar Mohan Murari. "Near-infrared LED based non-invasive blood glucose sensor". In: *2014 International Conference on Signal Processing and Integrated Networks (SPIN)*. IEEE. 2014, pp. 591–594.

[9] V Sao, K Pourrezaei, A Akin, and H Ayaz. "Breast tumor imaging using NIR LED based handheld continuous-wave imager". In: *2003 IEEE 29th Annual Proceedings of Bioengineering Conference*. IEEE. 2003, pp. 55–56.

[10] VL Colvin, MC Schlamp, and A Paul Alivisatos. "Light-emitting diodes made from cadmium selenide nanocrystals and a semiconducting polymer". In: *Nature* 370.6488 (1994), p. 354.

[11] Margaret A Hines and Gregory D Scholes. "Colloidal PbS nanocrystals with size-tunable near-infrared emission: observation of post-synthesis self-narrowing of the particle size distribution". In: *Advanced Materials* 15.21 (2003), pp. 1844–1849.

[12] Polina O Anikeeva, Jonathan E Halpert, Moungi G Bawendi, and Vladimir Bulovic. "Quantum dot light-emitting devices with electroluminescence tunable over the entire visible spectrum". In: *Nano letters* 9.7 (2009), pp. 2532–2536.

[13] Jeonghun Kwak, Wan Ki Bae, Donggu Lee, Insun Park, Jaehoon Lim, Myeongjin Park, Hyunduck Cho, Heeje Woo, Do Y Yoon, Kookheon Char, et al. "Bright and efficient full-color colloidal quantum dot light-emitting diodes using an inverted device structure". In: *Nano letters* 12.5 (2012), pp. 2362–2366.

[14] Seth Coe, Wing-Keung Woo, Moungi Bawendi, and Vladimir Bulović. "Electroluminescence from single monolayers of nanocrystals in molecular organic devices". In: *Nature* 420.6917 (2002), p. 800.

[15] Benjamin S Mashford, Matthew Stevenson, Zoran Popovic, Charles Hamilton, Zhaoqun Zhou, Craig Breen, Jonathan Steckel, Vladimir Bulovic, Moungi Bawendi, Seth Coe-Sullivan, et al. "High-efficiency quantum-dot light-emitting devices with enhanced charge injection". In: *Nature photonics* 7.5 (2013), p. 407.

[16] JM Caruge, JE Halpert, V Wood, V Bulović, and MG Bawendi. "Colloidal quantum-dot light-emitting diodes with metal-oxide charge transport layers". In: *Nature photonics* 2.4 (2008), p. 247.

[17] Xiwen Gong, Zhenyu Yang, Grant Walters, Riccardo Comin, Zhijun Ning, Eric Beauregard, Valerio Adinolfi, Oleksandr Voznyy, and Edward H Sargent. "Highly efficient quantum dot near-infrared light-emitting diodes". In: *Nature Photonics* 10.4 (2016), p. 253.

[18] Geoffrey J Supran, Katherine W Song, Gyu Weon Hwang, Raoul E Correa, Jennifer Scherer, Eric A Dauler, Yasuhiro Shirasaki, Moungi G Bawendi, and Vladimir Bulović. "High-performance shortwave-infrared light-emitting devices using core–shell (PbS–CdS) colloidal quantum dots". In: *Advanced materials* 27.8 (2015), pp. 1437–1442.

[19] Janis T Eells, MM Henry, P Summerfelt, MTT Wong-Riley, EV Buchmann, M Kane, NT Whelan, and HT Whelan. "Therapeutic photobiomodulation for methanol-induced retinal toxicity". In: *Proceedings of the National Academy of Sciences* 100.6 (2003), pp. 3439–3444.

[20] Hua Wu, Yu Zhang, Xiaoyu Zhang, Min Lu, Chun Sun, Tieqiang Zhang, and William W Yu. "Enhanced Stability and Performance in Perovskite Nanocrystal Light-Emitting Devices Using a ZnMgO Interfacial Layer". In: *Advanced Optical Materials* 5.20 (2017), p. 1700377.

[21] Heng Zhang, Hanrun Li, Xiaowei Sun, and Shuming Chen. "Inverted quantum-dot light-emitting diodes fabricated by all-solution processing". In: *ACS applied materials & interfaces* 8.8 (2016), pp. 5493–5498.

[22] Ebuka S Arinze, Botong Qiu, Nathan Palmquist, Yan Cheng, Yida Lin, Gabrielle Nyirjesy, Gary Qian, and Susanna M Thon. "Color-tuned and transparent colloidal quantum dot solar cells via optimized multilayer interference". In: *Optics Express* 25.4 (2017), A101–A112.

[23] Waldo JE Beek, Martijn M Wienk, Martijn Kemerink, Xiaoniu Yang, and René AJ Janssen. "Hybrid zinc oxide conjugated polymer bulk heterojunction solar cells". In: *The Journal of Physical Chemistry B* 109.19 (2005), pp. 9505–9516.

[24] Alexander H Ip, Susanna M Thon, Sjoerd Hoogland, Oleksandr Voznyy, David Zhitomirsky, Ratan Debnath, Larissa Levina, Lisa R Rollny, Graham H Carey, Armin Fischer, et al. "Hybrid passivated colloidal quantum dot solids". In: *Nature nanotechnology* 7.9 (2012), p. 577.

[25] Oleksandr Voznyy, Larissa Levina, Fengjia Fan, Grant Walters, James Z Fan, Amirreza Kiani, Alexander H Ip, Susanna M Thon, Andrew H Proppe, Mengxia Liu, et al. "Origins of stokes shift in PbS nanocrystals". In: *Nano letters* 17.12 (2017), pp. 7191–7195.

[26] Jianbing Zhang, Ryan W Crisp, Jianbo Gao, Daniel M Kroupa, Matthew C Beard, and Joseph M Luther. "Synthetic conditions for high-accuracy size control of PbS quantum dots". In: *The journal of physical chemistry letters* 6.10 (2015), pp. 1830–1833.

[27] Liangfeng Sun, Joshua J Choi, David Stachnik, Adam C Bartnik, Byung-Ryool Hyun, George G Malliaras, Tobias Hanrath, and Frank W Wise. "Bright infrared quantum-dot light-emitting diodes through inter-dot spacing control". In: *Nature nanotechnology* 7.6 (2012), p. 369.

[28] Martin A Green. "Commercial progress and challenges for photovoltaics". In: *Nat. Energy* 1.1 (2016), p. 15015.

[29] Anne Grete Hestnes. "Building integration of solar energy systems". In: *Solar Energy* 67.4-6 (1999), pp. 181–187.

[30] Andreas Henemann. "BIPV: Built-in solar energy". In: *Renewable Energy Focus* 9.6 (2008), pp. 14–19.

[31] Edward H Sargent. "Colloidal quantum dot solar cells". In: *Nature photonics* 6.3 (2012), p. 133.

[32] Graham H Carey, Ahmed L Abdelhady, Zhijun Ning, Susanna M Thon, Osman M Bakr, and Edward H Sargent. "Colloidal quantum dot solar cells". In: *Chemical reviews* 115.23 (2015), pp. 12732–12763.

[33] Junghwan Kim, Olivier Ouellette, Oleksandr Voznyy, Mingyang Wei, Jongmin Choi, Min-Jae Choi, Jea Woong Jo, Se-Woong Baek, James Fan, Makhsud I Saidaminov, et al. "Butylamine-Catalyzed Synthesis of Nanocrystal Inks Enables Efficient Infrared CQD Solar Cells". In: *Advanced Materials* 30.45 (2018), p. 1803830.

[34] Mengxia Liu, Oleksandr Voznyy, Randy Sabatini, F Pelayo García de Arquer, Rahim Munir, Ahmed Hesham Balawi, Xinzheng Lan, Fengjia Fan, Grant Walters, Ahmad R Kirmani, et al. "Hybrid organic–inorganic inks flatten the energy landscape in colloidal quantum dot solids". In: *Nature materials* 16.2 (2017), p. 258.

[35] Illan J Kramer, James C Minor, Gabriel Moreno-Bautista, Lisa Rollny, Pongsakorn Kanjanaboos, Damir Kopilovic, Susanna M Thon, Graham H Carey, Kang Wei Chou, David Zhitomirsky, et al. "Efficient spray-coated colloidal quantum dot solar cells". In: *Advanced materials* 27.1 (2015), pp. 116–121.

[36] Edward H Sargent. "Infrared photovoltaics made by solution processing". In: *Nature Photonics* 3.6 (2009), p. 325.

Chapter 5

Conclusion and Outlook

This thesis focuses on implementing nanophotonic design principles and applying advanced materials processing techniques to assemble nanomaterials with optimized properties for next-generation optoelectronic devices. By combining optical simulations, modeling, nanofabrication, and advanced optical and electrical characterization, we designed and built new photodetectors, solar cells and light emitting diodes with improved performance and novel functionality. These devices show great potential for a wide range of applications including in communication, security monitoring, defense and building-integrated photovoltaics.

Our photodetector work included improving the responsivity and extending the detection range of SnO_2 thin film visible-blind UV photodetectors by introducing CuO/SnO_2 nanoheterojunctions to the pristine SnO_2 thin films. Our photovoltaic work included using optical modeling and simulations to predict how embedding plasmonic nanoparticles in the absorbing media of a solar cell will affect the absorption of the device and making recommendations for

specific optimized systems. Secondly, we demonstrated color-tuned and semi-transparent solar cells by combing multi-objective optimization algorithms with multi-layer interference modeling. We demonstrated spray-casting as a viable way to build all-solution-processed flexible transparent solar cells that incorporate a Ag NW electrode. We investigated engineering the photonic band structure of absorbing materials to tune the spectral selectivity of a semiconductor thin film, which could find applications in both photovoltaics and photon detection technology. Our light emission work included demonstrating PbS CQD-based QLEDs emitting in the region of the near-infrared band that can be easily detected by silicon photodetectors. Combing our PbS CQD-based QLEDs with solution-processed Ag NW electrodes, we built flexible transparent light-emitting membrane technology for applications in motion capture, virtual reality goggles, and photobiomodulation therapy.

Future efforts to further improve the performance of the nanomaterial-based optoelectronic devices discussed here should focus on understanding the fundamental device physics, optimizing the material properties, and developing new device architectures. Our work on advanced fabrication techniques that enable scalable production of flexible transparent devices to expand the application areas of CQD solar cells are ultimately tied to an effort to meet the world's growing energy demands and solve the associated environmental problems. To facilitate innovations that have a broad impact, engineers from different disciplines and industries need to collaborate closely to work on packaging and integration of these devices into complete systems that can be deployed around the world.

Appendix A

Experimental Details

A.1 PbS CQD Synthesis

PbS CQDs were synthesized by modifying a previously published method [1] and using our home-built synthesis setup. The materials used were lead oxide (PbO, Alfa Aesar, >99.99 %), bis(trimethylsilyl)sulphide ($(TMS_2)S$ or TMS, Sigma-Aldrich, synthesis grade), oleic acid (Alfa Aesar, 90 %), 1-octadecene (ODE, Sigma-Aldrich, 90 %) and were used as purchased. All synthesis was performed using standard Schlenk line techniques. In an N_2-filled glovebox, TMS (0.18 ml) was added to ODE (10 ml), which had been dried and degassed by heating to 80 °C under vacuum for 16 h. A Pb oleate stock solution was prepared by mixing oleic acid (1.5 ml), PbO (0.45 g), and ODE (3 ml) and heating to 95 °C under vacuum for 16 hours then placed under nitrogen. 4.5 ml of the Pb oleate stock solution and 15 ml of ODE were heated to 120 ° C with constant stirring and nitrogen flow. The TMS/ODE mixture was then injected into the flask. After injection, the flask was allowed to cool gradually to 36 °C. The PbS CQDs were then precipitated with distilled acetone (40

ml) and centrifuged. After discarding the supernatant, the precipitate was re-dispersed in toluene. The PbS CQDs were precipitated again with acetone (5 ml) and methanol (5 ml), centrifuged for 5 min, dried, and finally dispersed in toluene. The yield of PbS CQDs was $\sim$0.40 g. The toluene-dispersed PbS CQDs were then stored in sealed vials at ambient conditions until ready to be washed and solvent-exchanged. Conditions such as TMS injection temperature, oleic acid weight, TMS weight and ODE volume could be varied to achieve different CQD sizes. PbS CQDs in toluene were brought into an N2-glovebox and precipitated with methanol. The supernatant was discarded and the remaining CQD powder was placed under vacuum until dry. The final redispersion is in octane at a dilution of 50mg/mL. The oleic acid -capped PbS CQDs in ocatane stock inks were then stored in sealed vials in the N_2-glovebox until ready to be utilized.

References

[1] Alexander H Ip, Susanna M Thon, Sjoerd Hoogland, Oleksandr Voznyy, David Zhitomirsky, Ratan Debnath, Larissa Levina, Lisa R Rollny, Graham H Carey, Armin Fischer, et al. "Hybrid passivated colloidal quantum dot solids". In: *Nature nanotechnology* 7.9 (2012), p. 577.

Botong Qiu

3400 N. Charles St., Barton 223B, Baltimore, MD, 21218

E-mail: bqiu4@jhu.edu *ORCID*: 0000-0001-6926-0458

EDUCATION

2019 Ph.D. in Electrical and Computer Engineering, Johns Hopkins University

2017 MSE in Electrical and Computer Engineering, Johns Hopkins University

2014 B.S. in Physics, Nanjing University

SKILL SET

Optical modeling: Lumerical, COMSOL Multiphysics, Zemax, MATLAB

Lab expertise: System integration and calibration, Custom parts design, Machine shop, Nanomaterial synthesis, Cleanroom fabrication

Experimental characterization and testing

- **Optical:** UV-Vis-NIR spectrophotometry, Pump-probe ultrafast spectroscopy, Interferometry, Optical profilometry, Optical microscopy, Integrating sphere, Emission spectroscopy (PL/EL), Quantum efficiency (EQE/IQE) measurements
- **Electrical:** 2D multimodal optelectronic scanning spectroscopy, I-V and C-V scanning, Four-point probe measurements, Photocurrent/photovoltage transient measurements
- **Thin film:** Electron microscopy (SEM/TEM), Surface topography (Dektak, Confocal microscopy), UPS, XPS, FTIR

,

Programming: MATLAB, LabVIEW, C, Python

Software: AutoCAD , Solidworks, Autodesk Maya, Origin, Microsoft Office

Soft skills: Passion for broadening the impact of technology, Good interpersonal and communication skills, Ability to work effectively and efficiently in an interdisciplinary team environment

RESEARCH EXPERIENCE

2014–2019, Research Assistant, Johns Hopkins University

Dissertation: *Nanophotonic design and nanomaterial assembly for next-generation optoelectronics*

Advisor: Prof. Susanna M. Thon; Thesis committee: Prof. Amy C. Foster, Prof. Jacob B. Khurgin

- FDTD optical simulation of enhanced absorption by nanoheterojunction incorporation in high-performing thin-film photodetectors
- Optical simulations of light trapping via LSPR of plasmonic nanoparticles and modeling of the overall absorption enhancement using our effective-medium model
- Optimizing multi-layer interference by combining TMM based optical modeling with optimization algorithms in MATLAB for color and transparency tuning in thin-film devices
- Optical design in Zemax to optimize the performance of integrated solar concentrator lenses

- Optical engineering of photonic bands in absorbing media for spectral selectivity
- Fully spray cast flexible transparent CQD solar cells
- CQD-based NIR flexible transparent LED array

LEADERSHIP ACTIVITIES

Fall 2017 **Team leader, JHU Bootcamp for Technology Entrepreneurs**: led our team "SolarFlex" to conduct market analysis, build our business model for our patented flexible integrated solar concentrator technology and deliver the business pitch to the business mentors

2018-2019 **Grant applicant, co-inventor, "The 2018 Cohen Translational Engineering Fund"**: co-inventor of the ”Flexible Transparent Membrane Light Emitting Diode Array and Systems Containing the Same” technology. I wrote the grant proposal and delivered the presentation to the Cohen fund committee. We were awarded $40,000 in funding. Currently we are working on system integration and building the prototype. U.S. Patent Application No.:62/828,707

HONORS AND AWARDS

2018 The Cohen Translational Engineering Fund Recipient. $40,000, more than 10 applications from JHU

2018 APS GERA Energy Research Workshop Invitee and Travel Grant. $\sim$50

invitees globally

2017 ARPA-E Energy Innovation Summit Student Invitee. 100 invitees in U.S.

Basketball: NJU All-star, FMVP, JHU GRO summer Champion, JHU CSSA team captain

VOLUNTEER AND TEACHING ACTIVITIES

2015-2019 **Mentor**: STEM Achievement in Baltimore Elementary Schools (SABES)

Summer 2015 **Mentor**: Johns Hopkins Center for Talented Youth (CTY) summer internship program

2017 & 2018 **Mentor**: NSF Research Experience for Undergraduates (REU) summer program

Fall 2015-2017 **Teaching assistant**: EN.520.270 Introduction to Renewable Energy Engineering (undergrad)

Spring 2016 **Teaching assistant**: EN.520.627 Photovoltaics and Energy Devices (graduate)

PUBLICATIONS

1. **Qiu, B.**, Lin, Y., Arinze, E. S., Chiu, A., Li, L., & Thon, S. M. (2019, April). In *2019 53rd Annual Conference on Information Sciences and Systems (CISS)* (pp. 1-5). IEEE.

2. Li, H., Plunkett, E., Cai, Z., **Qiu, B.**, Wei, T., Chen, H., ... & Katz, H. E. (2019) *Advanced Electronic Materials*, 1800618.

3. **Qiu, B.**, Lin, Y., Arinze, E. S., Chiu, A., Li, L., & Thon, S. M. (2018). *Optics Express*, 26(21), 26933-26945.

4. Lin, Y., Ung, G., **Qiu, B.**, Qian, G., & Thon, S. M. (2018). *ACS Applied Energy Materials*, 1(6), 2592-2599. **Featured as the cover article of *ACS Applied Energy Materials*: cover art by Botong Qiu and Gary Qian**

5. **Qiu, B.**, Arinze, E. S., Palmquist, N., Cheng, Y., Lin, Y., Nyirjesy, G., ... & Thon, S. M. (2017, May). In *CLEO: Science and Innovations* (pp. SM4K-5). Optical Society of America.

6. Arinze, E. S., **Qiu, B.**, Palmquist, N., Cheng, Y., Lin, Y., Nyirjesy, G., ... & Thon, S. M. (2017, June). In *2017 IEEE 44th Photovoltaic Specialist Conference (PVSC)* (pp. 667-669). IEEE. 7. Arinze, E. S.*, **Qiu, B.***, Palmquist, N., Cheng, Y., Lin, Y., Nyirjesy, G., ... & Thon, S. M. (2017). *Optics Express*, 25(4), A101-A112. ***Equal contribution**

8. Arinze, E. S., **Qiu, B.**, Nyirjesy, G., & Thon, S. M. (2016). *ACS Photonics*, 3(2), 158-173. **Featured as *ACS EditorsâĂŹ Choice***

9. Xie, T., Hasan*, M. R.*, **Qiu, B.***, Arinze, E. S., Nguyen, N. V., Motayed, A., ... & Debnath, R. (2015). *Applied Physics Letters*, 107(24), 241108. ***Equal contribution**

INTERNATIONAL CONFERENCE TALKS

IEEE CISS 2019, Contributed Talk. Baltimore, MD. *Controlling spectral selectivity in optoelectronics via photonic band engineering in absorbing media*

APS March Meeting 2019, contributed talk. Boston, MA. *Spectrally selective optoelectronic films via photonic band engineering in absorbing media*

APS March Meeting 2018, Contributed Talk. Los Angeles, CA. *Optimized multi-layer interference for color-tuned and transparent colloidal quantum dot solar cells*

CLEO: Science and Innovations 2017, Contributed Talk. San Jose, CA. *Optimized multilayer interference for color-tuning in colloidal quantum dot solar cells*

APS March Meeting 2016, Contributed Talk. Baltimore, MD. *Enhanced performance in SnO_2 thin film UV photodetectors via self-assembled CuO/SnO_2 nanoheterojunctions*